Studies on Optical Variability Properties of Less Luminous Active Galactic Nuclei by the Deep Multi-Band Photometry with Subaru Hyper Suprime-Cam

博士論文

Studies on Optical Variability Properties of Less Luminous Active Galactic Nuclei by the Deep Multi-Band Photometry with Subaru Hyper Suprime-Cam

（すばる望遠鏡 Hyper Suprime-Cam の多色深観測による
低光度活動銀河核の可視光度変光の性質に関する研究）

東北大学大学院
理学研究科 天文学専攻

木村勇貴

令和元年

Abstract

In this thesis, we study the variability of Active Galactic Nuclei (AGNs) by using the deep optical multi-band photometry data obtained from the Hyper Suprime-Cam Subaru Strategic Program (HSC SSP) Survey in the COSMOS field. The images analyzed here were taken with 8, 10, 13, 15 epochs over three years in g, r, i, and z band, respectively. Our variability selection is based on the probabilities of observed flux-differences and the cross-correlation coefficients between multi-band light curves. We have identified 491 robust variable AGNs, down to $i = 25$ mag, and their redshifts reach up to 4.26. Ninety percent of the variability-selected AGNs are individually detected in the Chandra deep X-ray imaging but the others are not, which suggests that our optical variability analysis is as sensitive to detect low luminosity type-I AGN as one of the deepest X-ray data obtained so far. The X-ray stacking analysis reveals the significant emission from the individually X-ray undetected AGNs in our variability-selected sample. The stacked samples show harder hardness ratio in their stacked X-ray spectrum than typical type-I AGNs, suggesting that the X-ray undetected optically variable AGNs have large soft X-ray absorption. We investigate the variability properties of the X-ray detected variable AGNs by using structure function analysis and find that the luminosity dependence of the structure function shows a 'turn-around' at 10^{45} erg s^{-1}, while that of more luminous sample shows consistent trend with the previous studies. The trend that weaker variability for less luminosity AGNs is likely to be caused by the larger contribution of the host galaxy light. Using the model templates of galaxy spectra, we evaluate the amount of host galaxy contribution to the structure function and find that dominance of young stellar population is needed to explain the observed luminosity-dependence of the structure function. This suggests that low luminosity AGNs ($L_{\rm bol} = 10^{44-45}$ erg s^{-1}) at $0.8 \lesssim z \lesssim 2.2$ are predominantly hosted in star-forming galaxies.

Contents

1 Introduction 1

1.1 AGN Optical Variability . . . 1

1.2 Identification of AGNs . . . 3

1.2.1 X-ray Radiation . . . 3

1.2.2 Broad Emission Lines . . . 4

1.2.3 Narrow Line Ratios . . . 6

1.2.4 Mid Infrared Colors . . . 6

1.3 Issues of Searching for Less Luminous AGNs . . . 9

1.4 Purposes of This Thesis . . . 16

2 Identification of Variable AGNs 18

2.1 Data Set . . . 18

2.2 Data Reduction . . . 23

2.2.1 Main Targets . . . 23

2.2.2 PSF Measurement and Matching . . . 24

2.2.3 Aperture Photometry . . . 26

2.2.4 Probability of Flux Difference . . . 27

2.3 Selection Method . . . 30

2.3.1 Ensemble Probability . . . 30

2.3.2 Cross-Correlation Coefficients of the Multi-band Light Curves . . . 34

2.3.3 Visual Inspection . . . 36

2.3.4 Comparison with the Previous Variability Survey . . . 43

3 Properties of Variability-Selected AGNs 45

3.1 Basic Information . . . 45

3.2 Stacking Analysis for X-ray Undetected Variable AGNs . . . 50

3.2.1 Stacking Analysis . . . 50

3.2.2 Other X-ray Contributions . . . 54

3.2.3 Hardness Ratio . . . 56
3.3 Dust Covering Factor . . . 60
3.4 Mid Infrared Color Diagnostics . . . 63

4 Structure Function Analysis 67
4.1 Ensemble Structure Function . . . 68
4.2 Dependences on Physical Parameters . . . 73

5 Discussion 81
5.1 Host Galaxy Contamination . . . 81
5.1.1 Host Galaxy to AGN Flux Ratio . . . 81
5.1.2 Constraints on the AGN Host Galaxy Type . . . 86
5.1.3 Host Galaxy Flux Contribution Rate to Structure Function . . . 89
5.2 Interpretations of X-ray Absorbed Variable AGNs . . . 93

6 Summary 95

Appendix 98
A Direct SQL Script . . . 98
B PSF Map . . . 99
C Limiting Magnitude Map . . . 107
D Variability Selected AGN Catalog . . . 115

Acknowledgement 125

Reference 126

1 Introduction

1.1 AGN Optical Variability

One of the characteristic features of Active Galactic Nuclei (AGNs) is their flux variation. The AGN flux variability was first found by Smith & Hoffleit (1963) and Matthews & Sandage (1963) soon after the discovery of the first quasars 3C 273 in 1963 (Schmidt, 1963). Currently a large number of multi-band observations show that the AGN flux variations are appeared in all wavelength ranges on timescales from several hours to many years (e.g., Ulrich et al., 1997). Figure 1.1 shows an example of light curves of continuum at 5100Å and the Hβ broad line for NGC 5548 (Seyfert 1 galaxy). As shown in Figure 1.1, the strength of AGN flux variation typically reaches $\sim$ 10% of the averaged flux level. The aperiodic AGN flux variations are often described by means of the root mean square (RMS) of magnitude difference as a function of time-lag or equivalently frequency, which are widely known as the structure function (SF) and power spectral density (PSD), respectively. Recent optical variability studies, based on large data sets of quasar light curves from time-domain surveys, show that the structure function, i.e., the variability amplitude of AGN, is correlated with the rest-frame time-lag, rest-frame wavelength, and AGN luminosity; the variability amplitude is lager at the longer time-lag, at shorter wavelength, and with fainter luminosity (e.g., Vanden Berk et al., 2004). Since AGN optical radiation is likely to be dominated by the accretion disk, such characteristic optical variability properties can be related to the disk instabilities.

Several models are proposed to explain the optical variability properties. Dexter & Agol (2011) propose the inhomogeneous accretion disk model, which consider the large local disk temperature fluctuations based on the stochastic process (Kelly et al., 2009). This model can describe not only the observed variability amplitude, but also the disk size predicted from microlensing studies (e.g., Pooley et al., 2007) and the UV excess appeared in the quasar composite spectrum (Zheng et al., 1997). However Kokubo (2015) argues that this inhomogeneous disk model can not describe the tight inter-band flux-flux correlations of optical

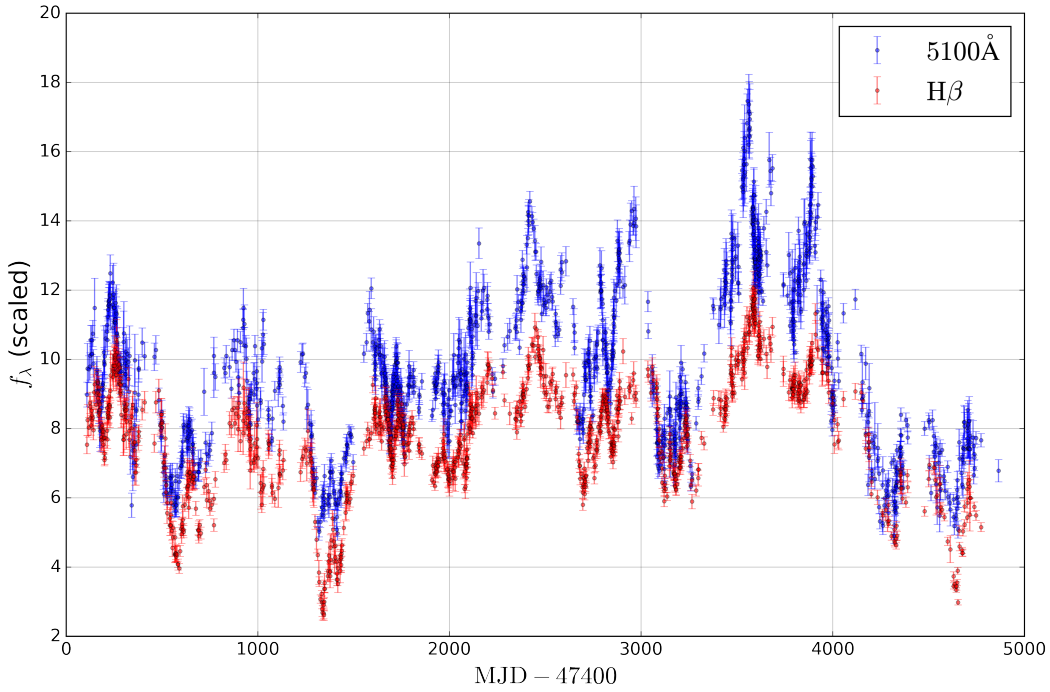

Fig 1.1: Light curves of the Seyfert 1 galaxy NGC 5548 (blue: 5100Å, red: Hβ). The data points are based on Peterson et al. (1991, 1992, 1994, 1999, 2002) and Korista et al. (1995).

variability.

Another plausible model is a X-ray reprocessing model (Krolik et al., 1991), which consider that a variation at the X-ray coronas located around the innermost region of the accretion disk illuminate the accretion disk. This model can explain the time-lag (the light travel time from the corona to the accretion disk) between X-ray light curves and UV-optical light curves (Noda et al., 2016) although the origin of variability of X-ray is not clear. Therefore the primary origin of AGN variability is still under debate.

1.2 Identification of AGNs

In addition to the variability signature, AGN has characteristic features in its spectrum, and several methods are commonly utilized in identifying AGNs, such as:

(i) Detection of X-ray,
(ii) Detection of broad emission lines,
(iii) Classification with narrow line ratios,
(iv) Mid infrared color diagnostics.

In this subsection, we briefly introduce each selection method.

1.2.1 X-ray Radiation

AGN can emit high energy photons in the vicinity of the central black hole. The typical X-ray spectrum of AGN contains a power-law continuum, reflection hump around 30 keV, iron Kα fluorescence line at 6.4 keV, and often an excess in the soft-band X-ray below 1 keV. The primary origin of the high energy photons from AGN is believe to be Comptonization of optical-UV photons from the accretion disk, which occurs in the hot corona located above the accretion disk. The Comptonization produces a power-law emission with photon index of $\Gamma \sim 1.8$-2.0. Other contributions in X-ray spectrum of AGN are the reprocessed X-ray emissions caused by the reflections at the molecular torus (e.g., Yaqoob, 2012), the BLR and NLR (Bianchi et al., 2008; Ponti et al., 2013), and the accretion disk (George & Fabian, 1991; Matt et al., 1991), which are seen as a reflection hump around 30-40 keV and fluorescence lines, such as an iron Kα emission line at 6.4 keV. Additionally a large fraction of AGN shows an excess component on the power-law continuum below 1 keV, which is called as soft excess. Several interpretations of this excess, such as the blurred reflection from an ionized disk (Crummy et al., 2006), smeared absorption by an ionized wind

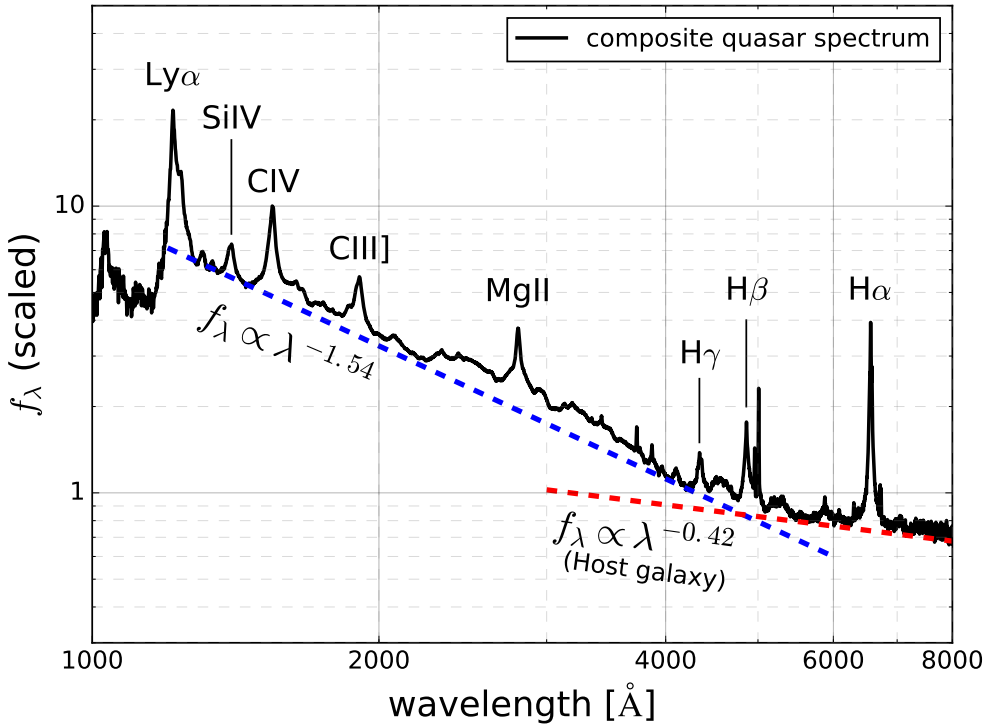

Fig 1.2: The median composite quasar spectrum presented by Vanden Berk et al. (2001), constructed from the spectra of 2204 SDSS quasars with redshift of $0.044 \leq z \leq 4.789$. Single power-law fitting functions with different slopes for the continuum bluer and redder than Hβ emission line are also plotted as the blue and red dashed lines, respectively. The prominent broad emission lines are labeled in figure.

from the inner disk (Gierliński & Done, 2004), are proposed, but the physical origin of this excess is still under debate.

1.2.2 Broad Emission Lines

Optically type-I AGN has not only narrow emission lines but also broad emission lines. The full width at half maximum (FWHM) of the broad emission line is typically more than $\gtrsim$ 1000-2000 km s^{-1}. Figure 1.2 shows the prominent broad emission lines in the optical wavelength range.

The line width of the broad emission line reflects the gas dynamics in the broad

line region (BLR). This means that the central black hole mass can be estimated from the line width of the broad emission line. From the virial theorem, the black hole mass can be written as:

$$M_{\rm BH} = f\left(\frac{R_{\rm BLR}\sigma^2}{G}\right) \tag{1.2.1}$$

where $R_{\rm BLR}$ is the size of the BLR, σ is the velocity dispersion of gas in the BLR, G is Newton's gravitational constant, and f is the dimensionless factor which depends on the geometry, kinematics, and inclination of the BLR. The typical value of this scaling factor is $\langle f \rangle \sim 5$ (Onken et al., 2004; Woo et al., 2010; Park et al., 2012). Reverberation mapping studies show that the size of BLR is correlated with the luminosity of AGN ($L_{\rm AGN}$) (e.g., Kaspi et al., 2000) with $R_{\rm BLR} \propto L^{\alpha}_{\rm AGN}$, and the slope α is close to the predicted value from photo-ionization model, ~ 0.5 (Bentz et al., 2006, 2009, 2013). The velocity dispersion is estimated from the line width of the broad emission line. Using these relations, the black hole mass can be simply estimated from the observable quantities, as:

$$\log\left(\frac{M_{\rm BH}}{M_\odot}\right) = a + b\log\left(\frac{\lambda L_\lambda}{10^{44}\ {\rm erg\ s^{-1}}}\right) + 2\log\left(\frac{\rm FWHM}{\rm km\ s^{-1}}\right), \tag{1.2.2}$$

where FWHM is the width of a broad emission line and λL_λ is an AGN monochromatic luminosity. The AGN monochromatic luminosities are often selected at 5100Å for Hβ (4861Å), 3000Å for MgII (2798Å), and 1350Å for CIV (1549Å) broad lines considering less contaminations from other emission lines, such as FeII, around the broad emission lines. The coefficients a and b are calibrated from the reverberation mapping technique and determined to be $a = 0.91$, $b = 0.50$ for Hβ (Vestergaard & Peterson, 2006), $a = 0.860$, $b = 0.50$ for MgII (Vestergaard & Osmer, 2009), and $a = 0.660$, $b = 0.53$ for CIV (Vestergaard & Peterson, 2006). This black hole mass estimation is widely used since it is easy to obtain the black hole mass once a spectroscopic observation is carried out.

1.2.3 Narrow Line Ratios

The extreme hard radiation from the accretion disk of AGN can ionizes the [OIII] and [NII] lines (ionization potentials are 14.5 eV and 35 eV, respectively). These collisionally excited emission lines ([OIII]λ5007, [NII]λ6584) are useful not only to classify between AGNs and star forming galaxies but also to understand the gas-phase chemical abundance, the ionization state of the gas, and the ionizing power source of the galaxy (for a review; see Kewley et al., 2019). Baldwin et al. (1981) classify galaxies dominated by AGN from those dominated by star formation by using the narrow line ratios of [OIII]/Hβ and [NII]/Hα (commonly referred to as the Baldwin, Phillips, Terlevich diagram; BPT diagram). Figure 1.3 shows the BPT diagram for the sample of the Sloan Digital Sky Survey (SDSS) Data Release 8 (DR8) (Brinchmann et al., 2004). Kewley et al. (2001) use the photoionization models to explain the line ratios of starburst galaxies and provide a theoretical upper limit for starburst galaxies (black solid line in Figure 1.3). On the other hand, Kauffmann et al. (2003) use 55757 galaxies from SDSS DR1 to revise the classification between AGNs and starburst galaxies (black dashed line in Figure 1.3). The objects located on the upper and lower lines in Figure 1.3 show composite ionization states of galaxies (green points in Figure 1.3). The intermediate line ratios can be produced by either a mixture of gas ionized by hot stars and AGN or a mixture of gas ionized by hot stars and radiative shocks. The objects over the upper limit of the theoretical prediction for starburst galaxies are classified as pure AGNs in the BPT diagram (red points in Figure 1.3).

1.2.4 Mid Infrared Colors

In the favored picture for the physical structure of AGN (the unified model, Antonucci, 1993), the accretion disk are surrounded by a optically thick dust and molecular torus (i.e., dusty torus). The hot and warm dust emission ($T \sim$

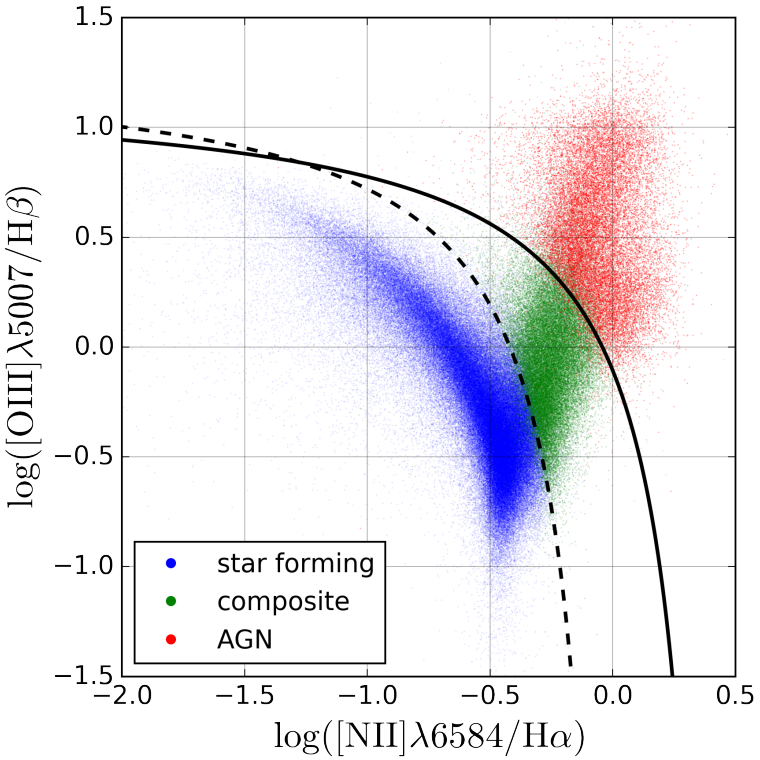

Fig 1.3: BPT diagram. The spectral data is taken from the SDSS-DR8, provided by the Max Planck Institute for Astrophysics and the Johns Hopkins University (MPA-JHU) group. The upper limit of star-forming region (solid line) is set to be equation (5) in Kewley et al. (2001). The revised devision line between AGN and star-forming region (dashed line) is provided as equation (1) in Kauffmann et al. (2003). The BPT classification shown in this figure is the same as Brinchmann et al. (2004).

1400 and 200 K, respectively) from the dusty torus overwhelms the host galaxy light, results in the power-law spectral energy distribution (SED) in mid-infrared (MIR) wavelength range for AGN. On the other hand, the polycyclic aromatic hydrocarbon (PAH) emissions (3.3, 6.2, 7.7, 8.6 μm) and warm dust radiation are dominated in MIR wavelength range for normal galaxies. Figure 1.4 shows model templates of type-I, type-II quasars, and starburst galaxy presented in Polletta et al. (2007) (each model template is labeled as $QSO1$, $QSO2$, and $M82$, respectively[*1]). The prominent PAH emission lines are appeared in the

[*1] http://www.iasf-milano.inaf.it/~polletta/templates/swire_templates.html

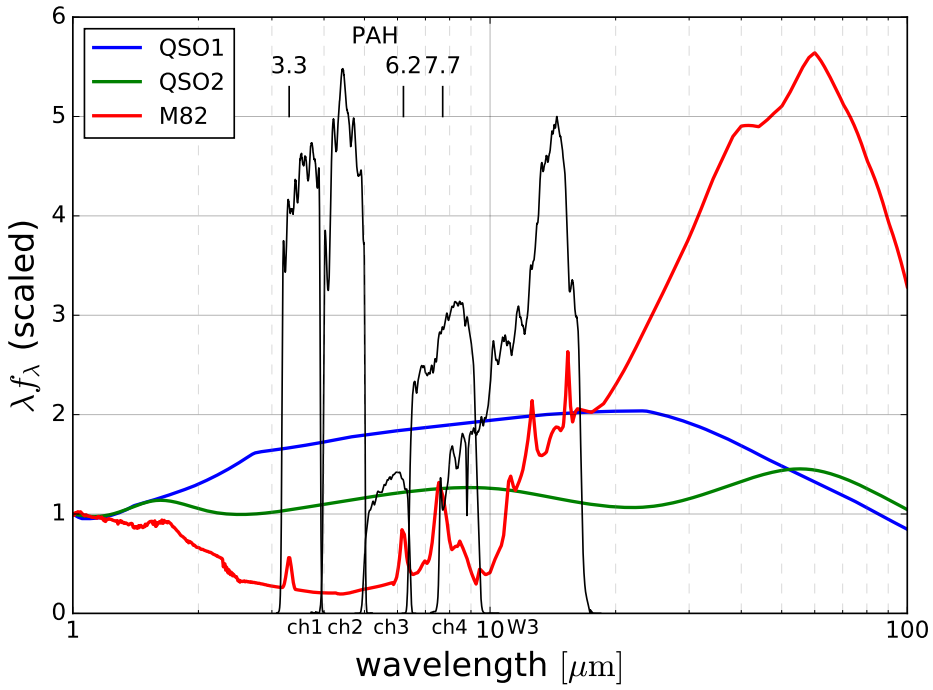

Fig 1.4: Model spectra for type-I quasar (blue), type-II quasar (green), and starburst galaxy (red), all of which are normalized at 1μm. IRAC band filter (3.6, 4.5, 5.8, 8.0 μm) and a unique WISE W3 band filter (12 μm) response curves are also shown in figure. The model SEDs are provided by Polletta et al. (2007).

starburst SED, on the other hand, quasars have a relatively flat spectrum in MIR wavelength range. From these characteristic features in MIR wavelength range, we can classify between AGNs and galaxies. Lacy et al. (2004, 2007), Stern et al. (2005) use the four broad-band channels (3.6, 4.5, 5.8, 8.0 μm) of the Infrared Array Camera (IRAC) mounted on the Spitzer Space Telescope to propose diagnostics to identify AGNs (including both type-I and type-II AGNs). Quasars are located in the redder color compared to the normal galaxies in their color-color plots. Jarrett et al. (2011) also propose the MIR color diagnostics to identify AGNs by using the Wide-field Infrared Survey Explorer (WISE) imaging data (3.4, 4.6, 12 μm).

1.3 Issues of Searching for Less Luminous AGNs

Recently less luminous AGNs are the focus of attention to understand the growth of not only central black holes but also their host galaxies. Low mass dwarf galaxies which are experienced few merger event may host pristine black holes, providing further clues to understand the origin of central black holes. Several theoretical models are proposed to explain the formation of seed black holes and their growth, such as gravitational runaway accretion at the center of a dense star cluster (e.g., Bahcall & Ostriker, 1975; Begelman & Rees, 1978; Quinlan & Shapiro, 1990; Lee, 1993), collapse of Population III stars (e.g., Bond et al., 1984; Madau & Rees, 2001), and direct collapse scenario (e.g., Haehnelt & Rees, 1993; Loeb & Rasio, 1994; Koushiappas et al., 2004), and each model shows the different trend in black hole mass function, occupation fraction, and black hole to bulge mass relation at lower mass side (for recent reviews; see Greene et al., 2019; Inayoshi et al., 2019). This means that observational constrains of those properties in low mass systems (black hole mass of less than 10^5 $M_\odot$) are essential.

However it is difficult to find low mass black holes hosted in less luminous systems among AGNs by methods of X-ray detection, broad lines, narrow line ratios, and MIR colors, due to the overwhelming host galaxy light.

We first show the detection limit of black hole mass in less luminosity AGNs by using one of the currently deepest X-ray data with more than 1 square degree area, the Chandra COSMOS Legacy Survey (Civano et al., 2016). The detection limits at 50% completeness level of X-ray flux in the Chandra COSMOS Legacy Survey are 4.9×10^{-16} erg s^{-1} cm^{-2} for soft-band (0.5-2 keV) and 3.1×10^{-15} erg s^{-1} cm^{-2} for hard-band (2-10 keV). This flux limit for each band can be converted to the AGN bolometric luminosity at a given redshift assuming a bolometric correction factor (~ 20, Lusso et al., 2012). Furthermore we change the bolometric luminosity to the Eddington luminosity $L_{\rm Edd}$ by introducing the Eddington ratio $\lambda_{\rm Edd}$, where $L_{\rm bol} = \lambda_{\rm Edd} L_{\rm Edd}$, and the Eddington luminosity can be converted to the black hole mass with 1.26×10^{38} erg s^{-1} ($M_{\rm BH}/M_\odot$).

Using these relations we can estimate the detection limit of black hole mass at a given redshift and Eddington ratio for each band. Figure 1.5 shows the detection limit of black hole mass for each band in the Chandra COSMOS Legacy Survey. We here set the Eddington ratio as 0.01, 0.10, and 1.00. Figure 1.5 suggests that the depth of the Chandra COSMOS Legacy Survey can detect AGNs with black hole mass larger than $10^{5.3}$ $M_{\odot}$ at $z \sim 1$ even if the Eddington ratio is the Eddington limit ($\lambda_{\rm Edd} = 1$).

Furthermore, such low mass black hole systems are difficult to be identified as type-I AGNs with the broad emission lines. In order to check how difficult to identify broad line AGNs in such low mass black hole systems, we estimate FWHM of broad lines as a function of black hole mass and Eddington ratio from equation (1.2.2). The AGN monochromatic luminosity λL_{λ} in equation (1.2.2) can be converted to the AGN bolometric luminosity $L_{\rm bol}$ with a bolometric correction factor BC_{λ} (9.26, 5.15, 3.81 for λ = 5100Å, 3000Å, and 1350Å, respectively; Shen et al., 2011). Additionally, the bolometric luminosity can be converted to the Eddington ratio and the Eddington luminosity, i.e., the black hole mass, as described before. Using these relations, the equation (1.2.2) can be modified to the following equation,

$$\log\left(\frac{\rm FWHM}{\rm km\ s^{-1}}\right) = \frac{1-b}{2}\log\left(\frac{M_{\rm BH}}{M_{\odot}}\right) - \frac{b}{2}\log\left(\frac{\lambda_{\rm Edd}}{BC_{\lambda}}\right) - \frac{a-5.9b}{2}. \quad (1.3.1)$$

This equation shows that the observed line width of the broad emission line is empirically determined from the conditions of the central black hole. Figure 1.6 shows the observed line width as a function of black hole mass with the Eddington ratio of 0.01, 0.1, and 1.0. If we consider again the case of the Chandra X-ray detection limit at $z = 1.0$, the FWHM of the broad emission line of Hβ is less than 1000 km s^{-1}, which is comparable to the width of narrow emission lines. This means that such low mass black hole systems hosted in less luminosity AGNs can be misclassified to as type-II AGNs in optical line diagnostics (optical type-I AGNs is often defined as broad line AGNs with the line widths of FWHM $\geq$ 2000 km s^{-1}; e.g., Merloni et al., 2014). In other words, another characteristic

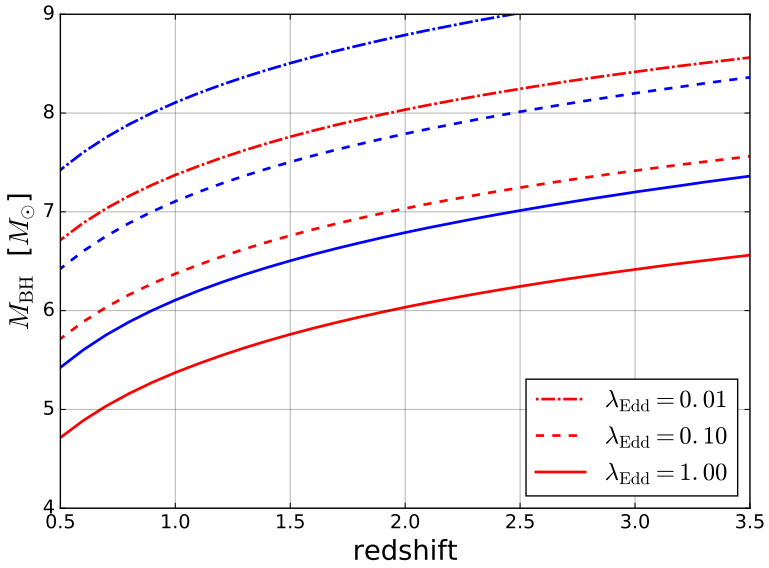

Fig 1.5: The detection limits of black hole mass as a function of redshift in the Chandra COSMOS Legacy Survey. The red (blue) lines are the 50% completeness level in the soft (hard) band. Each line type differs depending on the Eddington ratio.

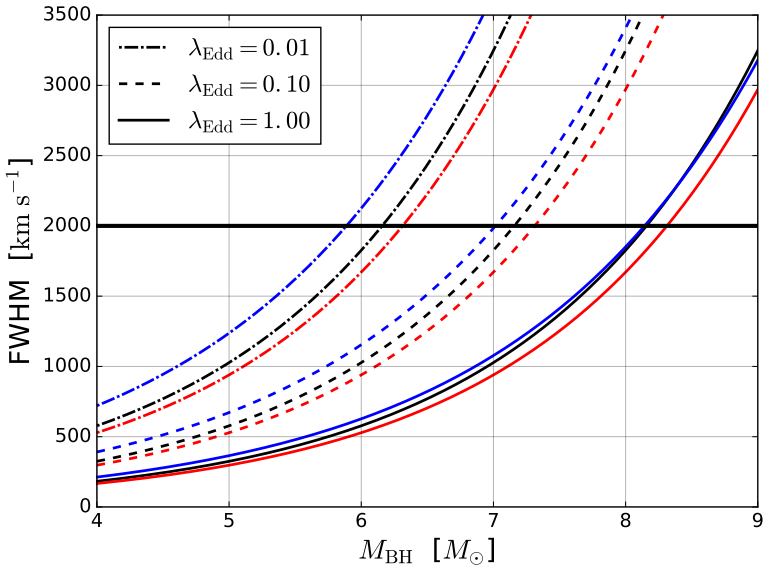

Fig 1.6: Predicted line widths of broad emission lines (black: Hβ, red: MgII, blue: CIV) as a function of black hole mass. Each line type differs depending on the Eddington ratio. The horizontal black solid line is a typical criterion of distinction between optically type-I and type-II AGNs (e.g., Merloni et al., 2014).

information is needed to classify such less luminous AGNs as 'type-I' AGNs.

It should be noted that the MIR color diagnostics is also difficult to identify less luminous AGNs. Hainline et al. (2016) investigate the MIR color for 35 BPT-selected dwarf AGNs ($M_\star < 3 \times 10^9 M_\odot$, $z < 0.055$; see Reines et al., 2013) in the SDSS DR8 data set and find that the majority of them are not identified as AGNs with the MIR color diagnostics. This indicates that in less luminous AGNs, the reprocessed dust radiation from the dusty torus is low enough that dust emission heated by star formation and PAH emission from host galaxy is dominated in MIR wavelength range. They also find that a large amount of contamination from star-forming dwarf galaxies enter the AGN MIR color selection since dust temperature and luminosity is higher in star-forming dwarf galaxies with lower-metallicity, which results in redder MIR color.

On the other hand, AGN variability can be more efficient to find less luminous AGNs because the lower luminosity AGNs tend to show larger variability amplitudes. Since the variability amplitude is independent of the line widths of the broad emission lines, detection of the variability signature is a direct way to identify type-I AGNs. Actually recent studies show that the variability-based AGN selection method can detect low mass black holes. Morokuma et al. (2016) find a low mass black hole ($M_{\rm BH} = 2.7 \times 10^6\ M_\odot$), whose line width of the broad Hα emission is 1880 km s^{-1}, from high-cadence (1 hour) optical imaging data. Baldassare et al. (2018, 2019) also find a few hundreds of low mass AGNs with host galaxy stellar mass of $M_\star < 10^{10}\ M_\odot$ from the optical variability method, although the low mass AGNs are classified as star-forming galaxies in the BPT diagram.

The variability selection is an efficient tool to identify less luminous AGNs hosting black holes with $M_{\rm BH} \lesssim 10^6\ M_\odot$. For less luminous AGNs, however the effect of host galaxies on the observed variability properties are not well investigated. In fact, Shen et al. (2011) shows that the host galaxy light contributions appear in the optical SED of the AGNs with the rest-frame 5100Å luminosity less than about 10^{45} erg s^{-1}. Additionally the luminosity dependence of variability amplitude in low luminosity AGNs is not clear in structure function analysis. Figure 1.7 shows the luminosity dependence of variability amplitude and shows

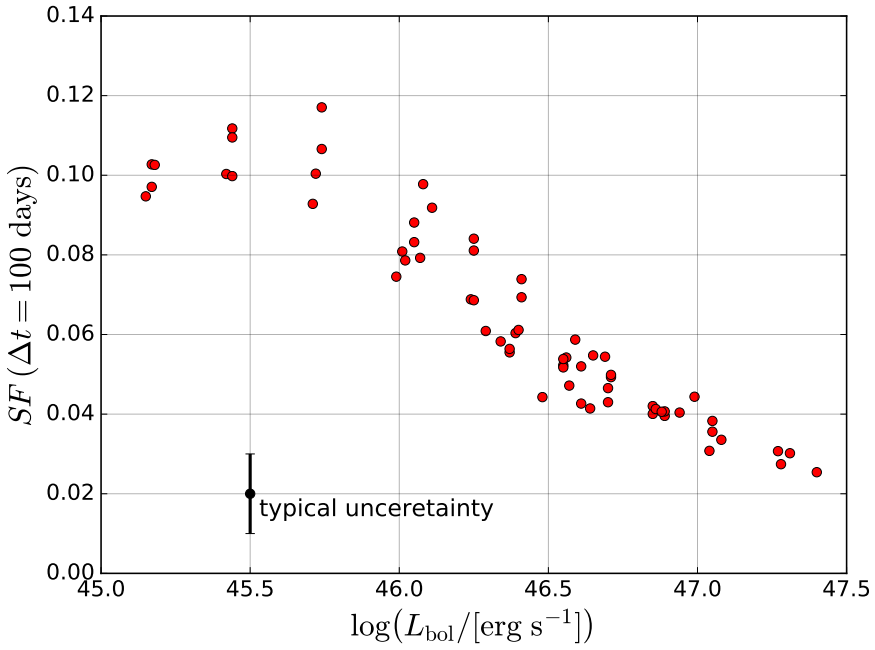

Fig 1.7: Luminosity dependence of variability amplitude at time-lag of 100 days, based on $\sim$ 28000 luminous broad line AGNs with the r-band light curves in the Palomar Transient Factory and intermediate Palomar Transient Factory (PTF/iPTF) surveys. It can be clearly seen that the variability amplitude is higher in lower AGN luminosity, however the lowest luminosity sample does not show this trend. This figure is reproduced by table 1 in Caplar et al. (2017).

that the variability amplitude at the lowest luminosity are slightly decreased possibly due to the contribution from the host galaxy light. To identify less luminous AGNs through variability analysis, we also need to know how the host galaxy light affects the optical variability properties.

Conducting variability analysis to identify less luminous AGNs and to investigate variability properties of less luminous AGNs, deep multi-epoch observations are needed. To assess the depth of observations for detecting variability signature from less luminous AGNs, which are, for example, not detected in the Chandra COSMOS Legacy Survey, we use an empirical relation between X-ray flux and optical band magnitude of AGNs (Tananbaum et al., 1979; Maccacaro et al., 1988). Figure 1.8 shows the relation for type-I AGNs, which are spectroscopically- or photometrically-identified as unobscured AGNs (Marchesi

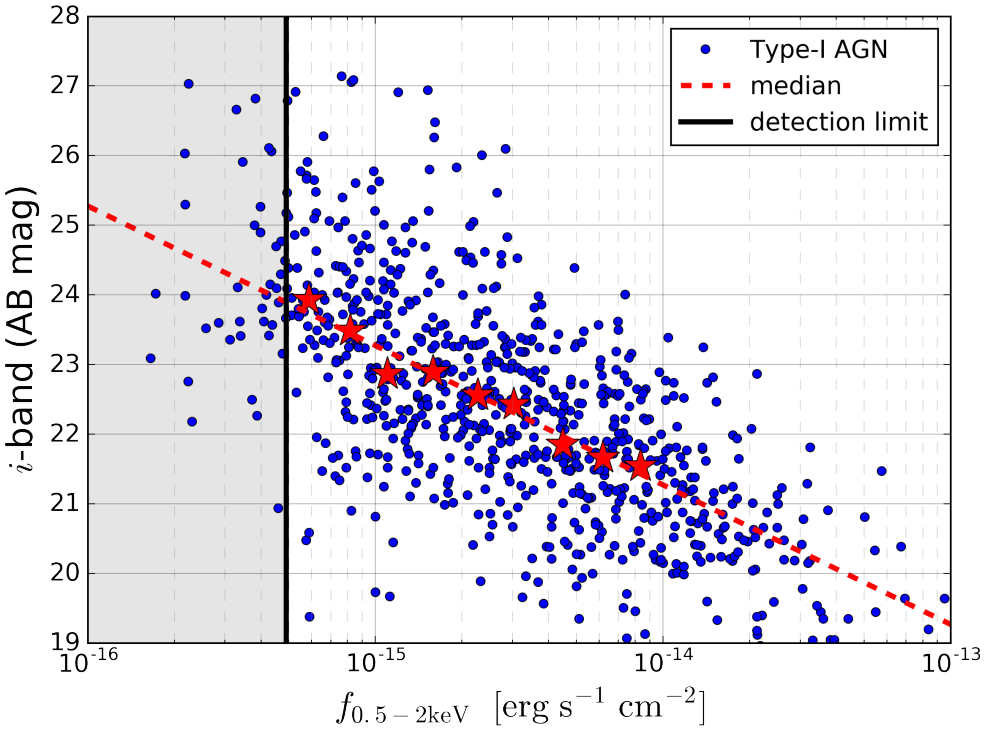

Fig 1.8: i-band magnitude vs soft-band (0.5-2 keV) X-ray flux plot for type-I AGNs. The black vertical line is the soft-band detection limit (50% completeness level) in the Chandra COSMOS Legacy Survey (Civano et al., 2016). The red star symbols are the median values of i-band magnitude distributions in each soft-band X-ray flux bin and the red dashed line is the result of fitting with a linear function. The data points are taken from the catalog presented by Marchesi et al. (2016).

et al., 2016). We calculate the median i-band magnitudes of type-I AGNs in soft-band flux bins ($f_{0.5\text{-}2\mathrm{keV}} \leq 1.0 \times 10^{-14}$ erg s^{-1} cm^{-2}) and fit them with a following linear function,

$$i\text{-mag} = a \left[-2.5 \log \left(\frac{f_{0.5\text{-}2\mathrm{keV}}}{f_{\mathrm{soft,limit}}} \right) \right] + b, \tag{1.3.2}$$

$$f_{\mathrm{soft,limit}} = 4.9 \times 10^{-16} \quad [\mathrm{erg\ s^{-1}\ cm^{-2}}],$$

where a and b are fitting free parameters and $f_{\mathrm{soft,limit}}$ is the soft-band detection

limit in Chandra COSMOS Legacy Survey. The best fitted parameters are $a = 0.80$ and $b = 23.89$, and the best fitted function is shown in the red dashed line in Figure 1.8. Equation (1.3.2) shows the typical i-band magnitude for type-I AGN at a given X-ray flux in the soft-band.

Here we consider the case of detecting the variability signature from AGNs with soft-band X-ray flux of 10^{-16} erg s^{-1} cm^{-2} ($\sim$ 1.5 mag deeper than the detection limit of the Chandra COSMOS Legacy Survey). From equation (1.3.2), the objects have typically 25.27 mag in i-band. If the objects show 10% flux variation in i-band, the magnitude difference is 0.10 mag. To detect such flux variation from differential images, we need additionally 0.15 mag (a factor of $\sqrt{2}$ in flux difference) deeper observations. This means that to detect variability signature from such X-ray undetected AGNs we need deep observations, in which the limiting magnitudes are deeper than at least 25.52 mag.

1.4 Purposes of This Thesis

In order to detect less luminous AGNs with variability method, deep multi-band imaging data with moderate cadence are essential. Since AGNs are relatively rare objects, wide sky coverage is also important to obtain a sufficient number of objects for statistical analysis. Recently Hyper Suprime-Cam Subaru Strategic Program (HSC SSP; Aihara et al., 2018a,b; Miyazaki et al., 2018; Komiyama et al., 2018; Kawanomoto et al., 2018; Furusawa et al., 2018; Bosch et al., 2018; Huang et al., 2018; Coupon et al., 2018) transient survey observations were carried out as a part of the UltraDeep layer from May 2014 to April 2017 with 5 broad band filters (g, r, i, z, y) in the COSMOS field (Yasuda et al., 2019). The main purpose of the UltraDeep layer in the HSC SSP survey is to probe high redshift galaxies and supernovae, and the limiting magnitude of each epoch in this field ($g, r, i \sim 26$, $z \sim 25$ and $y \sim 24$ mag; see figure 4 in Yasuda et al., 2019) is much deeper than the previous variability surveys ($r_{\rm P1} \sim 22$ mag for the Pan-STARRS 1 Survey; Simm et al. (2015), $r \sim 23.5$ mag for the VLT Survey Telescope Survey; De Cicco et al. (2019)). Thanks to these deep multi-epoch observations, we can identify AGNs which are not detected in X-ray imaging (see Section 1.3). The observations were carried with fair cadence with more than 8 epochs for each filter. Using the deep multi-epoch/band imaging data, we conduct optical variability analysis to obtain a new sample of variability-selected AGNs especially for faint objects that have not been studied so far and investigate the variability properties of less luminosity AGNs and the contributions of host galaxy light in the variability analysis.

In summary, the main purposes of this thesis are

- to identify wide luminosity range of AGNs, especially less luminous AGNs, from variability method,
- to study variability properties of less luminous AGNs,
- to investigate the host galaxy contribution to the AGN variability properties.

This thesis consists of the following sections. In Section 2, we introduce the data set of the HSC SSP UltraDeep observation in the COSMOS filed and show how to reduce the data set and how to identify robust variable AGNs. In Section 3, we show the basic properties of these variability-selected AGNs. We also present X-ray stacking analysis for X-ray undetected sample in the variability-selected AGNs. In Section 4, we investigate the optical variability properties for the variability-selected AGNs through examination of structure function. In Section 5, we discuss the effects of the host galaxy contribution to the variability properties, and examine the host galaxy properties of the variability-selected low luminous AGNs. The interpretation of X-ray undetected variable AGNs are also discussed in this section. Finally we summarize our results in Section 6.

Throughout this thesis we assume ΛCDM cosmological parameters of $\Omega_m = 0.3$, $\Omega_\Lambda = 0.7$ and Hubble constant $H_0 = 70$ km s^{-1} Mpc^{-1}. We use the AB magnitude system (Oke & Gunn, 1983; Fukugita et al., 1996) for all filters.

2 Identification of Variable AGNs

In this section, we introduce how to select variable AGNs from the HSC SSP data set. In Section 2.1, we introduce the HSC SSP survey and the data set we used in our variability analysis. Then we show reduction processes for taking aperture photometry and evaluate significance of flux differences for the main targets in Section 2.2. In Section 2.3, we show the selection method to identify robust variable AGNs.

2.1 Data Set

The HSC SSP survey consists of three main layers, called as **Wide**, **Deep**, and **UltraDeep**. Each field covers the area of 1400 deg^2 (Spring and autumn equatorial stripes, Hectomap) for Wide layer, 27 deg^2 (XMM-LSS, E-COSMOS, ELAIS-N1, DEEP2-F3) for Deep layer, and 3.5 deg^2 (SXDS, COSMOS) for UltraDeep layer, respectively (Aihara et al., 2018b). The depth of each layer is a few magnitude deeper (r-band magnitude $\sim$ 26, 27, 28 for Wide, Deep, and UltraDeep, respectively) than the previous surveys of comparable area, therefore the HSC SSP survey achieves the most powerful imaging data in the world.

In our variability analysis, we focus on the UltraDeep layer. This layer is one of the deepest observation in the HSC SSP survey therefore a suitable field for our variability study of less luminous AGNs. Especially, we use the data in the COSMOS field, where large number of multi-wavelength observations were carried out so far; X-ray (XMM-Newton/Chandra; Hasinger et al., 2007; Elvis et al., 2009; Civano et al., 2016; Marchesi et al., 2016), UV (GALEX; Zamojski et al., 2007), optical (HST/Subaru; Koekemoer et al., 2007; Taniguchi et al., 2007; Taniguchi et al., 2015), near-infrared (VISTA; McCracken et al., 2010, 2012), mid-infrared (Spitzer; Sanders et al., 2007; Steinhardt et al., 2014), far-infrared (Herschel; Lutz et al., 2011; Oliver et al., 2012), and radio (VLA; Schinnerer et al., 2007, 2010; Smolčić et al., 2017). All of these photometric measurements and the results of SED fitting are summarized in Laigle et al. (2016) (hereafter

COSMOS2015). The HSC SSP UltraDeep observations in this field were observed in May 2014 to April 2017. The all epoch data were reduced by using HSC pipeline (Bosch et al., 2018) version 4.0.5 with default configuration parameters.

HSC SSP multi-band observations were carried out with HSC g, r, i, z, and y-band filters. In our variability analysis, we did not use the y-band data since the y-band data is shallow and the scattered light[*2] still remains in the coadd images (Yasuda et al., 2019).

The HSC r-band and i-band filters were replaced to the new ones, referred as $r2$-band and $i2$-band with improved uniformity (Kawanomoto et al., 2018) on June 24, 2016 and February 2, 2016, respectively. No notable systematic differences in photometry are found in our analysis. For simplicity, hereafter we refer to both of them as r, and i-band filters without distinction.

In the HSC imaging data, the observed regions are specified as **tract** and **patch**. A tract field corresponds to a square field with 1.5 degrees on a side and each tract is divided into 9×9 patches, each of which has 4200 pixels ($\sim$ 11.8 arcmin) wide. The two adjacent tracts (patches) are overlapped each other with 1 arcmin (200 pixels, which correspond to 33.6 arcsec). To simplicity, we refer to a patch as 4000 pixels field with no overlaps from contiguous patches. Additionally we define **sub-patch** as a quarter patch field.

The COSMOS field is located in the **tract-9813** field. Within this tract, we confine our variability analysis field to the 41 patch regions which were observed in all the epochs and which are overlapped with the deep X-ray observation (total effective exposure time is larger than 150 ks in the Chandra COSMOS Legacy Survey; Civano et al., 2016). The X-ray effective exposure time map and the HSC SSP observed field is shown in Figure 2.1.

[*2] https://hsc-release.mtk.nao.ac.jp/doc/index.php/known-problems-in-dr1/

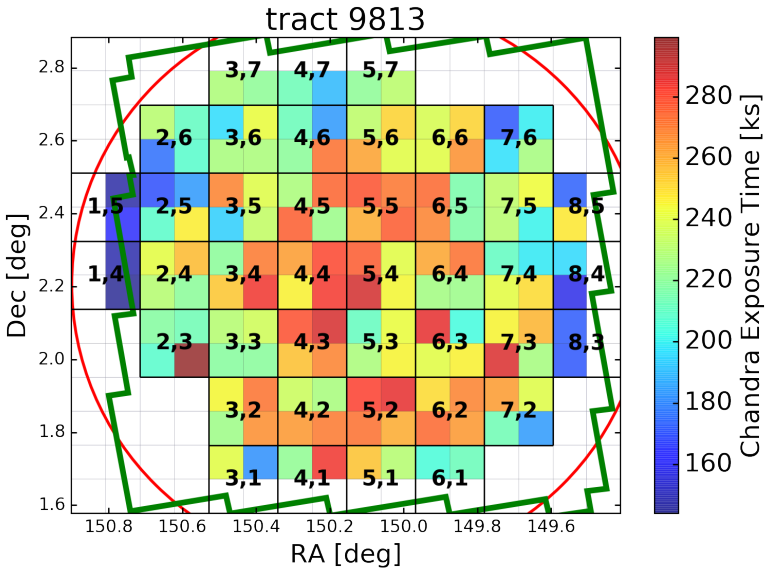

Fig 2.1: The HSC filed of view in the COSMOS region (red circle). We performed variability analysis in the color-mapped area. The color map corresponds to the median Chandra X-ray effective exposure time within each sub-patch field. The green solid area is the full mosaic of HST observation (Koekemoer et al., 2007). The patch identifications are printed on the maps.

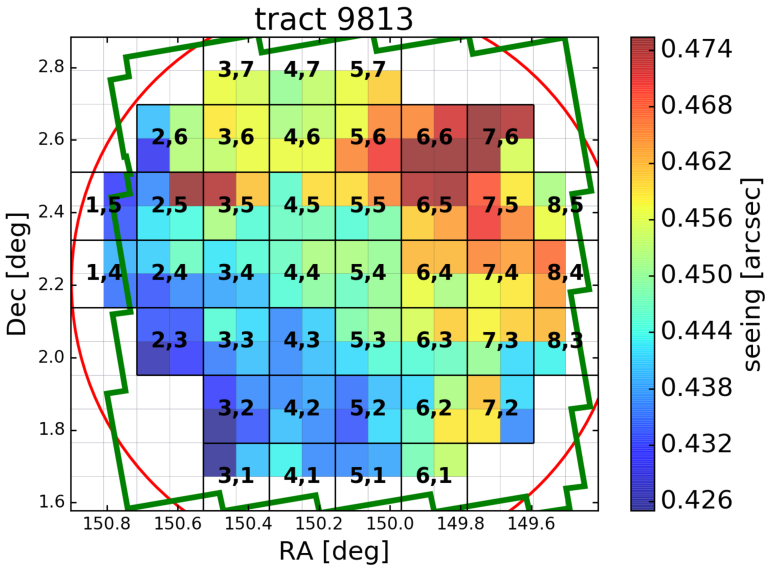

Fig 2.2: The same as Figure 2.1, but the color map corresponds to the median PSF size within each sub-patch field. This data was taken in 2017-02-02 with i-band filter.

We used only the good seeing data, where the median FWHM of point sources among all sub-patches is less than 1 arcsec (the procedure to estimate the FWHM is described in later). The total number of epochs for our variability analysis is 8, 10, 13, 15 for g, r, i, and z-band, respectively, therefore we can consider 28, 45, 78, 105 pairs of the epochs for each filter. The observational information in each epoch/filter are summarized in Table 2.1. The limiting magnitudes are calculated from random apertures in each sub-patch field. The aperture radius is set to be 1.5 times of FWHM of point sources after PSF matching among all epochs in each filter. The calculation process of limiting magnitude is described in Section 2.2.3 in detail. The median values of limiting magnitudes in each epoch are also summarized in Table 2.1.

Table 2.1: Summaries of the HSC SSP UltraDeep COSMOS Survey

		g-band			r-band			i-band			z-band		
Date	MJD	Δt	PSF	$m_{\rm lim}$	Δt	PSF	$m_{\rm lim}$	Δt	PSF	$m_{\rm lim}$	Δt	PSF	$m_{\rm lim}$
(1)	(2)	(3)	(4)	(5)	(3)	(4)	(5)	(3)	(4)	(5)	(3)	(4)	(5)
2014-03-28	56744		-		0	0.53	26.03	0	0.74	25.31	0	0.83	24.75
2014-11-18	56979	0	0.72	26.24		-			-			-	
2015-01-16	57038		-			-			-		294	0.48	25.33
2015-01-21	57043		-			-		299	0.53	25.66		-	
2015-03-18	57099		-		355	0.51	25.84		-			-	
2015-05-17	57159	180	0.90	25.89		-			-			-	
2015-05-21	57163		-			-		419	0.57	25.46		-	
2016-01-15	57402		-			-			-		658	0.82	24.67
2016-03-07	57454	475	0.72	26.18		-			-			-	
2016-03-09	57456		-		712	0.94	25.51		-			-	
2016-03-12	57459		-			-			-		715	0.49	24.72
2016-11-23	57715		-			-			-		971	0.69	24.50
2016-11-25	57717		-			-		973	0.76	25.15		-	
2016-11-28	57720		-		976	0.72	25.60		-			-	
2016-11-29	57721		-			-			-		977	0.97	24.65
2017-01-02	57755	776	0.65	25.96		-		1011	0.64	25.53	1011	0.72	24.58
2017-01-21	57774		-			-			-		1030	0.49	25.20
2017-01-23	57776		-		1032	0.77	25.60	1032	0.66	25.57		-	
2017-01-30	57783		-			-		1039	0.71	25.14	1039	0.60	24.88
2017-02-01	57785	806	0.61	25.58		-			-			-	
2017-02-02	57786		-		1042	0.61	25.59	1042	0.45	24.78		-	
2017-02-21	57805		-			-			-		1061	0.61	24.68
2017-02-23	57807		-		1063	0.87	25.59		-			-	
2017-02-25	57809		-			-		1065	0.65	25.02		-	
2017-03-04	57816		-			-		1072	0.59	25.48	1072	0.60	24.68
2017-03-06	57818		-		1074	0.69	25.58		-			-	
2017-03-22	57834	855	0.79	25.97		-			-		1090	0.54	24.71
2017-03-23	57835		-			-		1091	0.62	24.98		-	
2017-03-25	57837		-		1093	0.90	25.37		-			-	
2017-03-29	57841	862	0.87	25.73		-			-		1097	0.71	24.57
2017-03-30	57842		-			-		1098	0.92	25.17		-	
2017-04-23	57866		-		1122	0.88	25.30		-		1122	0.76	24.37
2017-04-26	57869	890	0.83	25.58		-			-			-	
2017-04-27	57870		-			-		1126	0.53	24.98		-	
2017-04-29	57872		-			-			-		1128	0.70	24.24

(1) Observed date in the format of yyyy-mm-dd.
(2) Modified Julian Date of the observed date.
(3) Days from the first observation for each filter.
(4) Median FWHM of PSF among all sub-patches. The unit is arcsecond.
(5) Median limiting magnitude (S/N=5) among all sub-patches.

2.2 Data Reduction

To identify variable AGNs from observed images, we need to perform aperture photometry and evaluate the deviation of flux-difference in each epoch-pair. In this subsection, we introduce the procedure of these calculations in detail. First we explain the main targets we conducted variability analysis in Section 2.2.1. Then we homogenized the PSF in the data between each epoch-pair, shown in Section 2.2.2. In Section 2.2.3, we performed fixed aperture photometry for the targets. Finally we calculated flux-differences between one epoch to another and evaluated the deviation of target's flux-difference in Section 2.2.4.

2.2.1 Main Targets

To calculate aperture photometry in our variability analysis, we first collected targets' positions from the HSC SSP multi-stacked catalog (hereafter **HSC catalog**). This data can be retrieved from the HSC Direct SQL Search[*3]. We here used the `s16a_udeep.forced` catalog in the public data release 1 (PDR1).

To obtain clean sources, we removed the objects from the sample in the HSC catalog by using the flags of bad pixels (`flags_pixel_bad`), edges of images (`flags_pixel_edge`), cosmic ray (`flags_pixel_cr_venter`), saturation (`flags_pixel_saturated_center`), and interpolated by the surrounding pixels (`flags_pixel_interpolated_center`). In addition, we also removed the objects using the bright objects flag which shows that the object is affected by the nearby bright stars (`flags_pixel_bright_object_any`). The SQL keywords of these flags are summarized in Table 2.2 and the full SQL script is described in Appendix A.

As mentioned in the previous section, the multi-wavelength observations were conducted in the COMSOS field. In order to analyze with these multi-wavelength data, we then matched the sources in the HSC catalog with the objects listed in

[*3] The public data release is now available in https://hsc-release.mtk.nao.ac.jp.

Table 2.2: HSC Direct SQL selection flag

keyword	description	boolean
`detect_is_primary`	primary object[*1]	True
`flags_pixel_bad`	on bad pixels of CCDs	False
`flags_pixel_edge`	at the edges of images	False
`flags_pixel_cr_center`[*2]	affected by cosmic rays	False
`flags_pixel_saturated_center`[*2]	saturated	False
`flags_pixel_interpolated_center`[*2]	interpolated	False
`flags_pixel_bright_object_any`[*3]	affected by bright objects	False

[*1] These objects are selected as isolated objects or deblended children.
[*2] This flag is judged within 3 pixels around source's center position.
[*3] This flag is judged within sources's footprint.

the COSMOS2015 within 0.6 arcsecond distance. It is noted that some objects listed in the COSMOS2015 are matched with more than two objects listed in the HSC catalog. This is mainly occurred to the object which is deblended from a parent object by the HSC deblending algorithm. We removed such objects for constructing clean variable objects. We also confined to the objects, which are brighter than 26 magnitude in i-band, to remove the objects which are not detected in each epoch imaging data. This magnitude threshold is ~ 0.3 magnitude deeper than that of each epoch imaging data (Table 2.1). Finally we selected 271475 targets (hereafter **parent sample**) in total and we used this sample to perform aperture photometry described in Section 2.2.3.

2.2.2 PSF Measurement and Matching

While HSC covers a wide field of view (~ 1.5 deg^2) in one shot, the PSF varies not only in observed date but also on the position in the field. Before conducting aperture photometry, we corrected the PSF differences for each position in each epoch-pair.

The PSF size was calculated from the point sources in each sub-patch field.

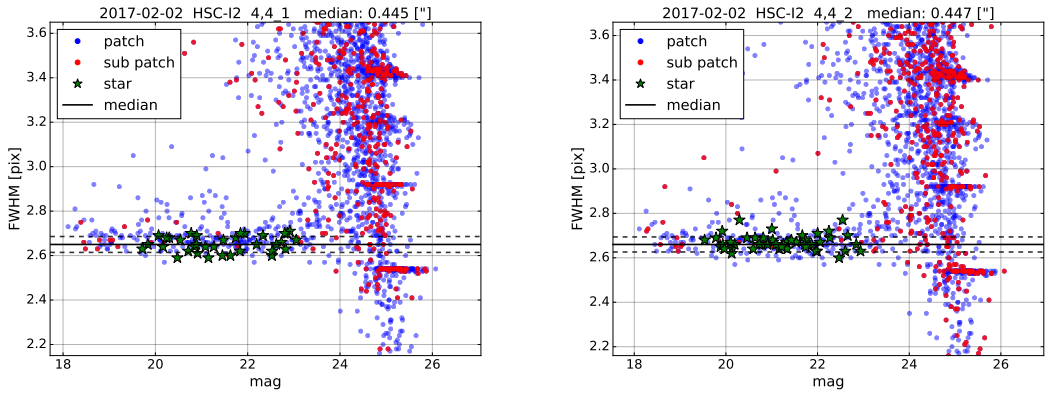

(a) sub-patch 1 (b) sub-patch 2

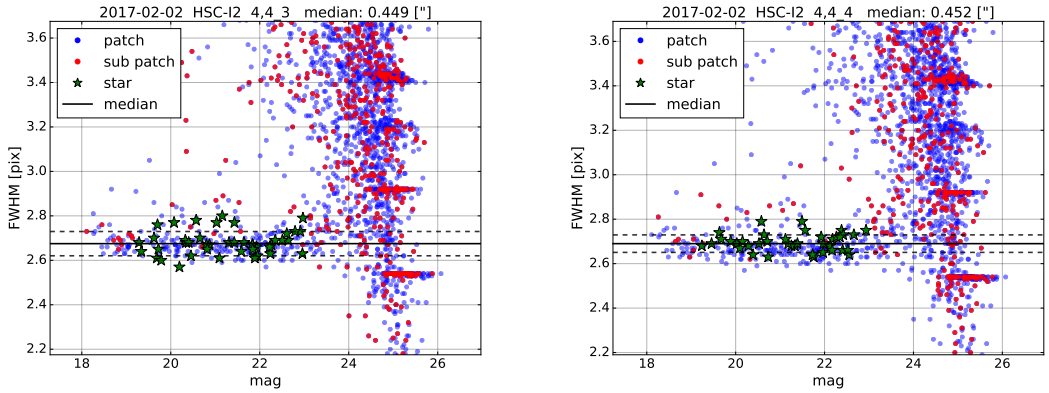

(c) sub-patch 3 (d) sub-patch 4

Fig 2.3: PSF values as a function of magnitude at patch 4,4 field observed in 2017-02-02 with i-band filter. Four panels correspond to the distributions in each sub-patch field. The blue points are results of objects in the patch field and the red points are results of objects in the sub-patch field. The green symbols are the point sources for calculating PSF size in each sub-patch field. The black solid line is the median PSF size for point sources and the black dashed lines are those standard deviations. The pixel scale for HSC image is 0.168 arcsecond.

Point sources were selected from the information of 2nd order adaptive moment calculated by using Hirata-Seljak-Mandelbaum (HSM) algorithms (Hirata & Seljak, 2003; Mandelbaum et al., 2005), which is available in the HSC catalog. We selected the objects whose 2nd order moments (`moment_11`, `moment_22`) are almost equal to the PSF 2nd order moments at each position (`psfmoment_11`, `psfmoment_22`), described in the following conditions:

$$\frac{\texttt{moment\_11}}{\texttt{psfmoment\_11}} < 1.1, \quad \frac{\texttt{moment\_22}}{\texttt{psfmoment\_22}} < 1.1. \tag{2.2.1}$$

The number of point sources is about a few times of ten in each sub-patch field. Then we calculated FWHM of the point sources from `SExtractor v2.19.5` and derived the median FWHM values in each sub-patch field for all the bands/epoch data. Figure 2.3 shows the distributions of FWHM for the sample in the 4,4 patch (four sub-patches; 4,4_1, 4,4_2, 4,4_3, and 4,4_4) field observed in 2017-02-02 with i-band filter. It is clear that the point sources selected from equation (2.2.1) are located in the stellar sequence, where the FWHM of PSF is almost constant in a wide range of magnitude. The median values of the FWHM in each epoch are summarized in the Table 2.1. The PSF maps for all the epochs data are shown in Appendix B.

For the matching of the PSF sizes, we used IRAF `gauss` task. From this task, we matched the FWHM of PSF to the worst value between 'one epoch-pair'. The PSF-matched images were used to calculate the significance of flux differences in each epoch-pair, shown in Section 2.2.4. We also matched the FWHM of PSF to the worst value among 'all epochs' in each filter. These images were used to calculate the cross-correlation coefficients of inter-band light curves in later (Section 2.3.2).

2.2.3 Aperture Photometry

After PSF matching, we conducted aperture photometry using IRAF **phot** task. In our variability analysis, we set the 'fixed' aperture radius to be 1.5× FWHM of the matched PSF, and adopted the center position of the aperture to be the coordinates of the main targets listed in the HSC catalog. The local average value of the sky background was evaluated in a circular annulus with

the inner and outer radius of 2.0 and 2.5 times the FWHM value, respectively.

We also examined the limiting magnitudes in each sub-patch field from the following procedure. First we performed the aperture photometry on randomly selected positions without the positions of main targets. The aperture radius were set to be the same size as the photometry for the main targets. Then we constructed the histogram of their counts and fitted with a Gauss function to estimate the standard deviation of the sky background. This deviation is regarded as the 1σ sky fluctuation in the aperture of the main targets. The limiting magnitude was calculated from 5 times of this sky fluctuation (i.e., signal to noise ratio S/N = 5). If the objects have fainter than the limiting magnitudes in both epochs in a given epoch-pair, we flagged such targets with '**faint**' in the epoch-pair. The maps of limiting magnitude for the images, whose PSFs were matched to the worst one among 'all epochs' in each filter, are shown in Appendix C and the median limiting magnitudes in the field for each epoch are summarized in Table 2.1.

In aperture photometry, nearby sources may affect and cause fake variation due to the slight change of seeing in locally. We confined our targets to those objects where the photometric aperture is not overlapped with other objects. If the surface brightness of the adjacent sources at the radius of the aperture larger than 2σ of the sky background, or the surface brightness of the target itself, we flagged such target with '**neighbor**'. It is noted that the number of *neighbor*-flagged objects depends on the seeing size and the depth of imaging, i.e., different at each epoch-pair. This flag was used to select variable sources in later (Section 2.3.1).

2.2.4 Probability of Flux Difference

Using the photometric results in a given epoch-pair, we calculated flux-differences, defined as one epoch flux value subtracted from another epoch one, for all the targets. An example of distribution of the flux-differences is shown in

the top panel of Figure 2.4.

The variation of the flux differences is larger in brighter objects due to the dominance of their own Poisson error. To evaluate the deviations of flux difference for each magnitude bin, we fitted the distribution (Δf) with a Gauss function; $N_k \exp\left[-(\Delta f_k - \mu_k)^2/2\sigma_k^2\right]$, with three free parameters, the normalization (N), mean value (μ), and standard deviation (σ) of the k-th magnitude bin. Here we set magnitude bin to be 0.2 for the brighter samples (magnitude larger than 23) and to be 0.1 for the fainter ones (magnitude down to the limiting magnitude). The bottom panel of Figure 2.4 shows the standard deviation for each magnitude bin. Then we fitted these standard deviations with a model function which is based on the error propagations of the photometric errors. The fitting result is also shown as the black solid curve in the bottom panel. The shaded region is the area estimated from the 1σ sky fluctuations in both epochs, and consistent with our results in the faintest magnitude bin, which is due to the dominance of sky background in the photometry.

Using these magnitude-dependent standard deviations, we evaluated the significance of flux differences for all the targets in a given epoch-pair. The significance were assessed by the following probability,

$$P_i\ (\Delta f_i \mid \mu_i, \sigma_i) = \frac{1}{\sqrt{2\pi\sigma_i^2}} \exp\left[-\frac{(\Delta f_i - \mu_i)^2}{2\sigma_i^2}\right], \tag{2.2.2}$$

where Δf is a object flux-difference, and μ and σ are the mean and standard deviation of flux-difference at the object magnitude in i-th epoch-pair. Since the distribution of flux-differences follows a Gauss distribution, we can evaluate the significance of object's flux-difference from equation (2.2.2). We calculated the probability for all the targets in all the epoch-pairs.

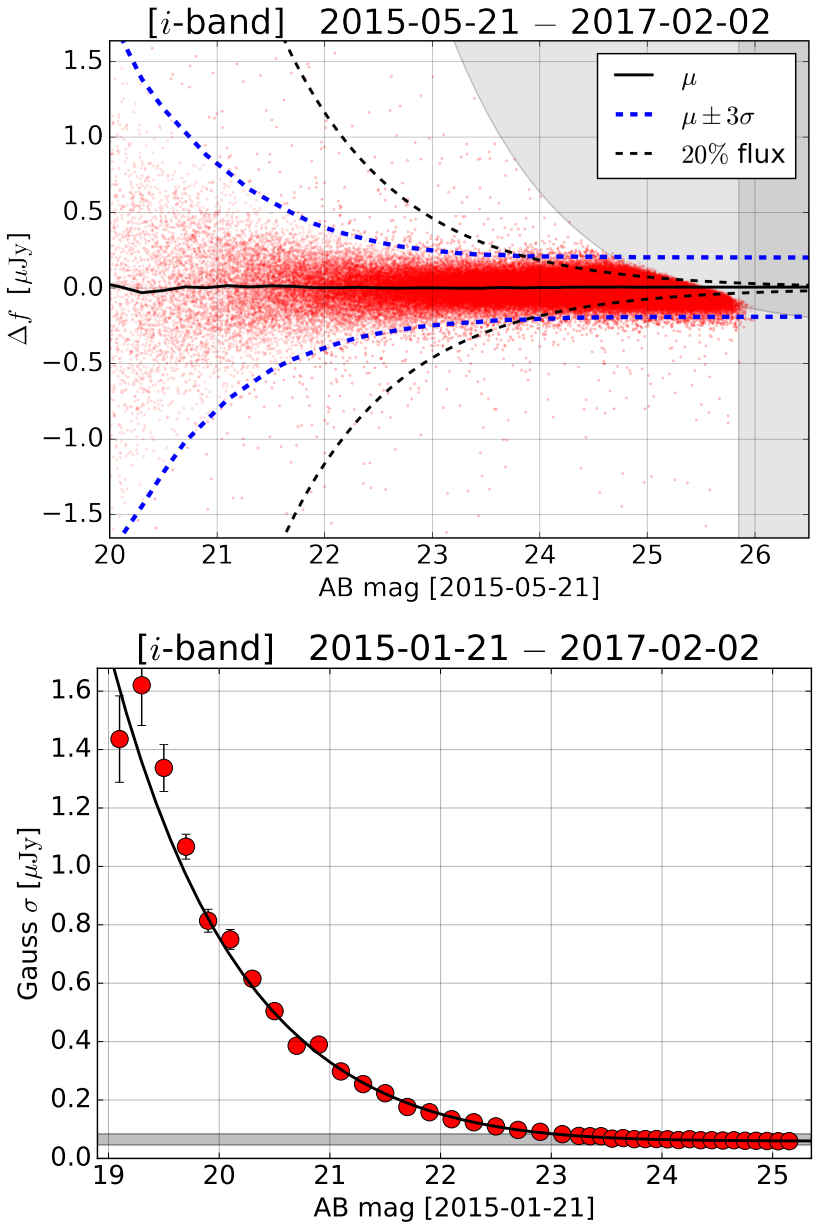

Fig 2.4: (Top) Distribution of flux differences (2015-05-21 and 2017-02-02 epochs pair in i-band filter). The black solid line is the center of a Gauss function for each magnitude. The blue dashed lines are the three times standard deviation from the center. The black dashed lines are the 20% flux levels. The shaded regions are areas where the signal to noise ratios are less than 5.0 in both epochs. (Bottom) The fitting result of the standard deviations in each magnitude bin. The solid line is the best fitted result. The shaded region is the area where the noise is dominated by the sky background.

2.3 Selection Method

In this subsection, we show how to identify variable AGN candidates from the observational data set. The procedure consists of three steps. First we use the ensemble probabilities to evaluate variability significance in each filter described in Section 2.3.1. Next we select the objects which have good cross-correlation between two-band light curves described in Section 2.3.2. Finally we conduct visual inspection to remove spurious samples described in Section 2.3.3. After selecting variable AGNs, we check variability-detection rate in our method by using the variability-selected AGNs in the previous surveys as shown in Section 2.3.4.

2.3.1 Ensemble Probability

In Section 2.2.4, we evaluated the variability significance in each epoch-pair by the probability described as equation (2.2.2). We collect the probabilities for all the epoch-pairs in each filter, we evaluate the significance of variability in each filter. This probability-based variability significance in each filter (hereafter we refer to this probability as **ensemble probability**) are defined as:

$$\begin{aligned} P_{\mathrm{band}}(n) &= \prod_{i}^{n} P_i\ (\Delta f_i \mid \mu_i, \sigma_i) \\ &= \prod_{i}^{n} \frac{1}{\sqrt{2\pi\sigma_i^2}} \exp\left[-\frac{(\Delta f_i - \mu_i)^2}{2\sigma_i^2}\right], \end{aligned} \tag{2.3.1}$$

where Δf is flux-difference of a target, μ and σ are the mean and standard deviation at the target's magnitude in i-th epoch-pair, which were calculated in Section 2.2.4. n is the number of epoch-pairs where the target is not flagged as $faint$ nor $neighbor$, described in Section 2.2.3. It is noted that the maximum value of n is 28, 45, 78, 105 for g, r, i, and z-band, respectively.

The smaller ensemble probability means more significant flux variation. To

select variable objects, we set a threshold by considering the minimum ensemble probability of non-variable objects ($P_{\rm min}(n)$) that occupy a large fraction of the parent sample. Non-variable objects are defined as follows: First we consider the following function to decide the critical value of flux-difference, $x_{\rm crit}$,

$$F(n, x_{\rm crit}) \equiv \prod_{i}^{n} P_i \left(\frac{|\Delta f_i - \mu_i|}{\sigma_i} \leq x_{\rm crit} \mid \mu_i, \sigma_i \right) = \left[\int_{-x_{\rm crit}}^{x_{\rm crit}} \frac{1}{\sqrt{2\pi}} \exp\left(-x^2/2\right) dx \right]^n . \quad (2.3.2)$$

This function means the fraction of objects which have never experienced the absolute flux-difference ($|\Delta f_i - \mu_i|$) more than $x_{\rm crit}\sigma_i$ in all the n epoch-pairs. In our analysis, we set $F = 0.95$, which corresponds that 95% of the sources are assumed to be non-variable objects for the data in one band filter. Once F is set, the critical value $x_{\rm crit}$ only depends on the number of epoch-pairs, e.g., $x_{\rm crit} \sim 3.12$, 3.25, 3.41, 3.49 for $n = 28$, 45, 78, and 105 (the maximum number of epoch-pairs for g, r, i, and z-band), respectively. Then we find the objects which have never experienced the absolute flux-difference more than $x_{\rm crit}\sigma_i$ in all the n epoch-pair. Hereafter we refer these objects as ***non-Var*** sample. Using the *non-Var* sample, we calculate the minimum ensemble probability $P_{\rm min}(n)$ for each filter. We then search for the objects which satisfy the following condition:

$$P_{\rm band}(n) < P_{\rm min}(n), \quad (2.3.3)$$

and set a flag of '***variability***' in this filter to the objects.

The top panel of Figure 2.5 shows the cumulative distributions of ensemble probabilities in each filter (n is the maximum epoch-pairs in each filter). The bottom panel of Figure 2.5 shows the same distribution as the top panel but only for the well known (i.e., previously cataloged) broad line AGNs (BLAGNs) in the parent sample. We use the X-ray catalog (hereafter **Chandra catalog**; Marchesi et al., 2016), the COSMOS2015 catalog, and HSC catalog to select the

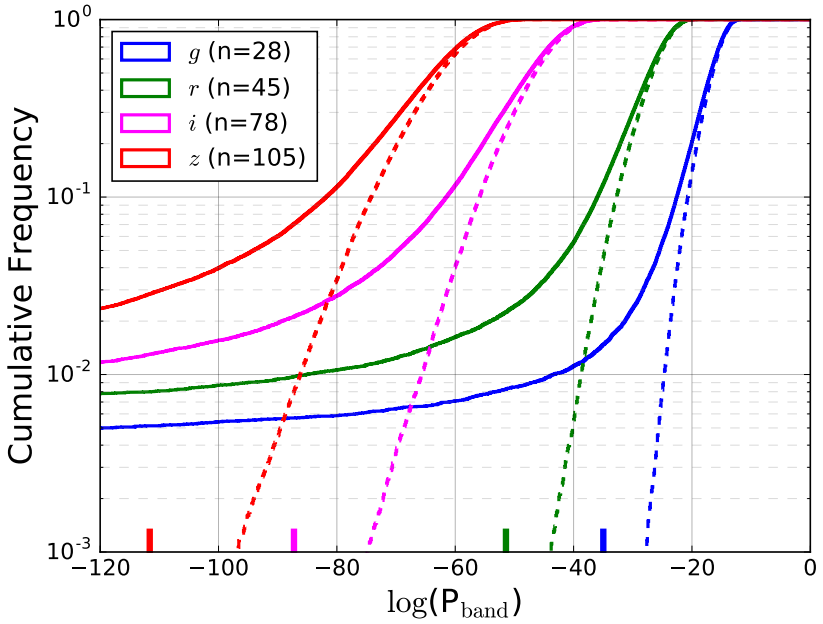

(a) Parent sample

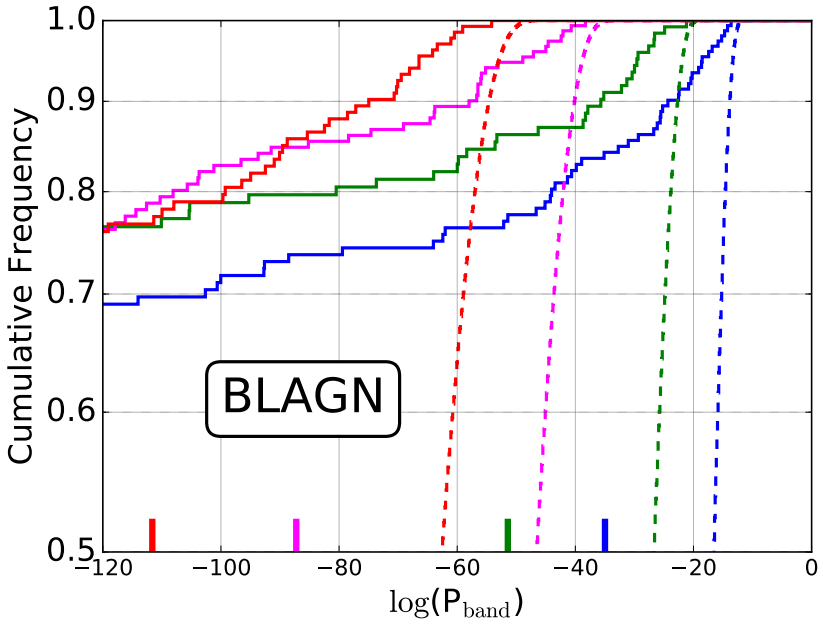

(b) BLAGNs

Fig 2.5: Cumulative distribution of ensemble probability for (a) the parent sample and (b) the known BLAGNs in each filter (blue: g-band, green: r-band, magenta: i-band, red: z-band). The vertical short lines show the values of $P_{\rm min}(n)$ for each filter.

known BLAGNs from all of the following criteria;

$$\text{(i) and (ii) and (iii) and (iv)},$$

where

(i) `spec_type` = 1 from the Chandra catalog, which are broad line (FWHM > 2000 km s^{-1}) AGNs identified by spectroscopic information.

(ii) `Qg` ≥ 1.5 from the Chandra catalog, which means clear spectroscopic redshift is available.

(iii) $21 \leq m_i \leq 24$ from the HSC catalog, which is cmodel i-band magnitude.

(iv) Objects which are not identified as stars.

The stars are selected from `TYPE` = 1 from the COSMOS2015 catalog (identified from SED fitting), or `star_flag` ≥ 1 from the Chandra catalog (spectroscopically, photometrically, and visually identified), or spectroscopic redshift *spec-z* = 0 from the HSC catalog (hereafter this flag is referred to as **star-flag**). It is clearly shown in Figure 2.5 that $\gtrsim 75\%$ of BLAGNs are classified as significant variable objects in each filter.

We then apply the following criterion to obtain more robust variable candidates,

$$n_{\rm band} \geq 2, \tag{2.3.4}$$

where $n_{\rm band}$ is the number of *variability*-flagged filters. From this criterion, we find 1744 variable candidates (0.64% of the parent sample). Although this criterion may remove real variable objects, it is found to be useful to remove the single-band fake variable sources which may be affected by spurious such as passing artificial satellites or bad pixels. We check the fraction of the objects missed in this criterion by using the known BLAGNs and find that 83% of the BLAGNs satisfy the criterion (2.3.4) and other 4% of the BLAGNs show $n_{\rm band} = 1$ (the other 13% of them show $n_{\rm band} = 0$).

2.3.2 Cross-Correlation Coefficients of the Multi-band Light Curves

Since AGN variability shows strong inter-band correlations over the wide range of optical wavelength, densely-sampled light curves of a real AGN should have a strong cross-correlation. To make the selection of variable AGNs more robust, we apply additional criterion by using cross-correlations of the multi-band light curves.

We calculate the cross-correlation coefficients of each pair of two *variability*-flagged band light curves for the variable candidates. It is noted that if $n_{\rm band} = 2$, 3, or 4, we calculate cross-correlation coefficients of 1, 3, or 6 of two *variability*-flagged band light curves, respectively. Here we consider that the two band photometries obtained within 5 days are quasi-simultaneous observations, which yields more than 5 data point pairs for calculating cross-correlations ($n_{\rm pair}$ in Table 2.3). Using these data point pairs, we calculate the cross-correlation coefficient $R_{\rm A,B}$ between band-A and band-B as:

$$R_{\rm A,B} = \frac{\sum_i^{n_{\rm pair}} \left(f_{{\rm A},i} - \langle f_{\rm A} \rangle\right) \left(f_{{\rm B},i} - \langle f_{\rm B} \rangle\right)}{\sqrt{\sum_j^{n_{\rm pair}} \left(f_{{\rm A},j} - \langle f_{\rm A} \rangle\right)^2} \sqrt{\sum_k^{n_{\rm pair}} \left(f_{{\rm B},k} - \langle f_{\rm B} \rangle\right)^2}}, \tag{2.3.5}$$

where f is the observed flux and $\langle f \rangle$ is the time-averaged flux. It is noted that in this calculation, aperture photometry was re-performed where the PSF sizes of the two band images of all the epochs were homogenized to the largest PSF size among the images (see Section 2.2.3).

Figure 2.6 shows the cumulative distributions of the cross-correlation coefficients between two-band pairs. Each line represents the case for *non-Var* sample (black), classified in both filters, objects with $n_{\rm band} = 2$ (magenta), $n_{\rm band} = 3$ (green), and $n_{\rm band} = 4$ (blue). The red line shows the case for the known BLAGNs which indeed shows stronger correlations than the *variability*-flagged samples.

To select robust variable sample, we set a criterion for each cross-correlation

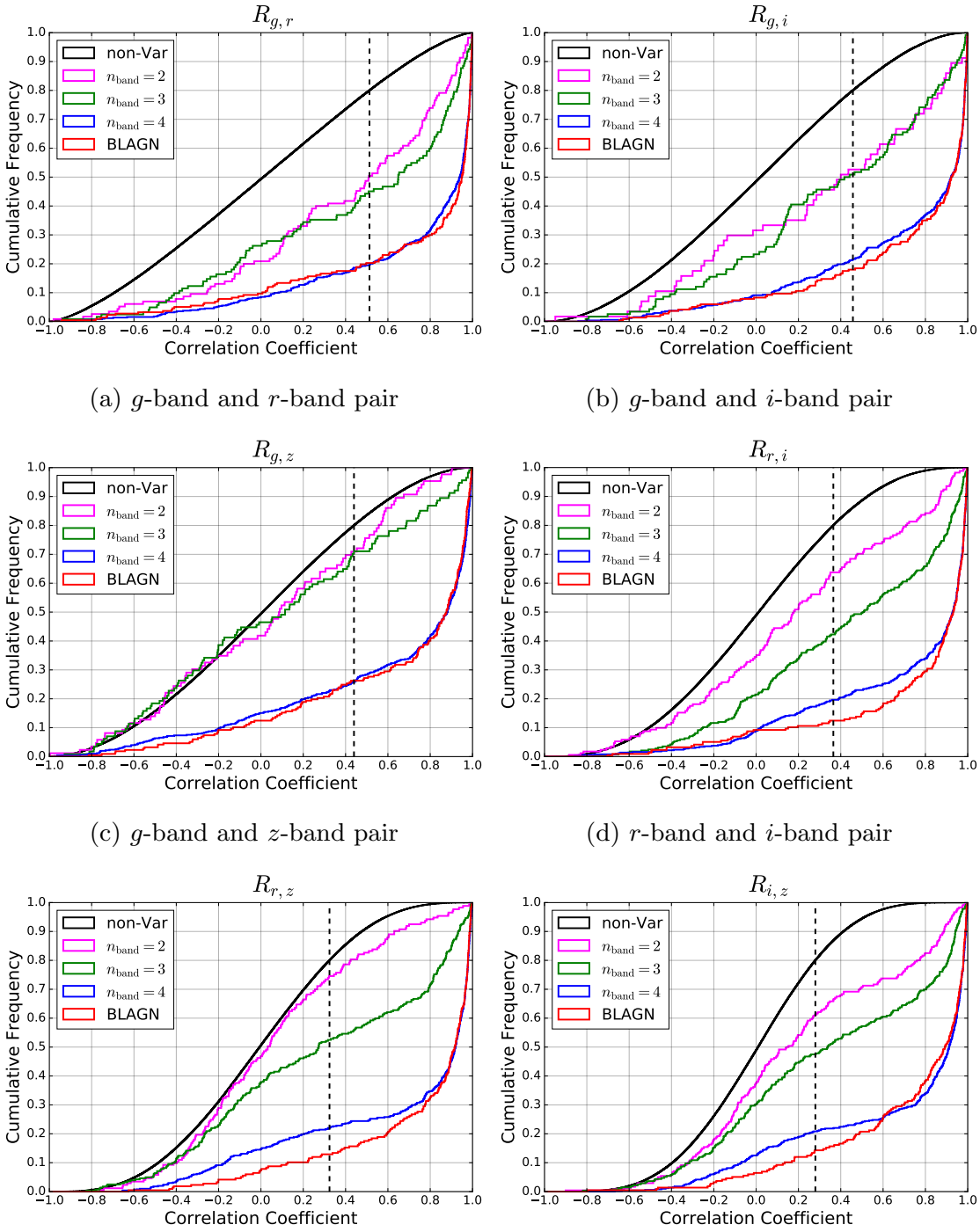

(a) g-band and r-band pair

(b) g-band and i-band pair

(c) g-band and z-band pair

(d) r-band and i-band pair

(e) r-band and z-band pair

(f) i-band and z-band pair

Fig 2.6: Cumulative distribution of the cross-correlation coefficients between two-band light curves. The black distribution is calculated from the non-Var sample. The magenta, green, blue distribution is a result of the objects that satisfy the case of $n_{\rm band} = 2$, 3, and 4, respectively. The red distribution is the result of the known BLAGNs. The vertical dashed lines show the threshold $R_{\rm crit}$.

Table 2.3: Cross-correlation coefficient criteria

band pair	$n_{\rm pair}$	$R_{\rm crit}$
g, r	5	0.513
g, i	6	0.457
g, z	6	0.440
r, i	8	0.365
r, z	9	0.324
i, z	12	0.280

coefficient in which only the top 20% of *non-Var* sample show the value, and set the flag of '***correlation***' in this band-pair. These critical values ($R_{\rm crit}$) are shown in the black dashed lines and listed in Table 2.3. About more than 75% of the known BLAGNs satisfy this criterion in each cross-correlation coefficient as seen in Figure 2.6. We require for variable objects to satisfy this cross-correlation coefficient criterion in at least one band-pair, namely,

$$n_{\rm corr} \geq 1, \tag{2.3.6}$$

where $n_{\rm corr}$ denotes the number of *correlation*-flagged band-pairs. After applying this criteria, we can recover $\sim$ 82% of all the known BLAGNs and $\sim$ 99% of BLAGNs which satisfy the criteria (2.3.4). Finally we obtain 1078 variable candidates in total (0.40% of the parent sample, and 62% of the objects which satisfy the criteria (2.3.4)).

2.3.3 Visual Inspection

By applying the criteria (2.3.4) and (2.3.6), we obtain 1078 variable candidates. These are robust candidates, but some possible false signal variable still remain. As we are interested in AGNs, supernovae should also be classified among them.

For the purpose, we conduct visual inspection of the images and light curves. Mainly we visually classify,

(i) objects which are clearly affected by the satellite, bad pixels, adjacent objects, and bright stars,

(ii) supernova candidates which have single burst light curves or show off-nuclear brightening,

(iii) spurious objects which are large extended objects.

In our visual inspection, 196 objects ($\sim 18\%$) are identified as case (i). Examples of these objects are shown in Figure 2.7. We also identify 186 objects as case (ii). An example of the supernova candidate is shown in Figure 2.8, which clearly shows an off-nuclear transient and supernova like light curves. Furthermore we identify 134 objects as case (iii). Finally we remove 71 variable stars and candidates by using the star-flag (see Section 2.3.1). Consequently we obtain 491 variable AGN candidates, of which 441 objects ($\sim 90\%$) are listed in the Chandra catalog. The examples of X-ray detected variable AGNs and X-ray undetected variable AGNs are shown in Figure 2.9 and Figure 2.10, respectively.

A schematic flowchart for identifying the variable AGNs in our analysis is summarized in Figure 2.11.

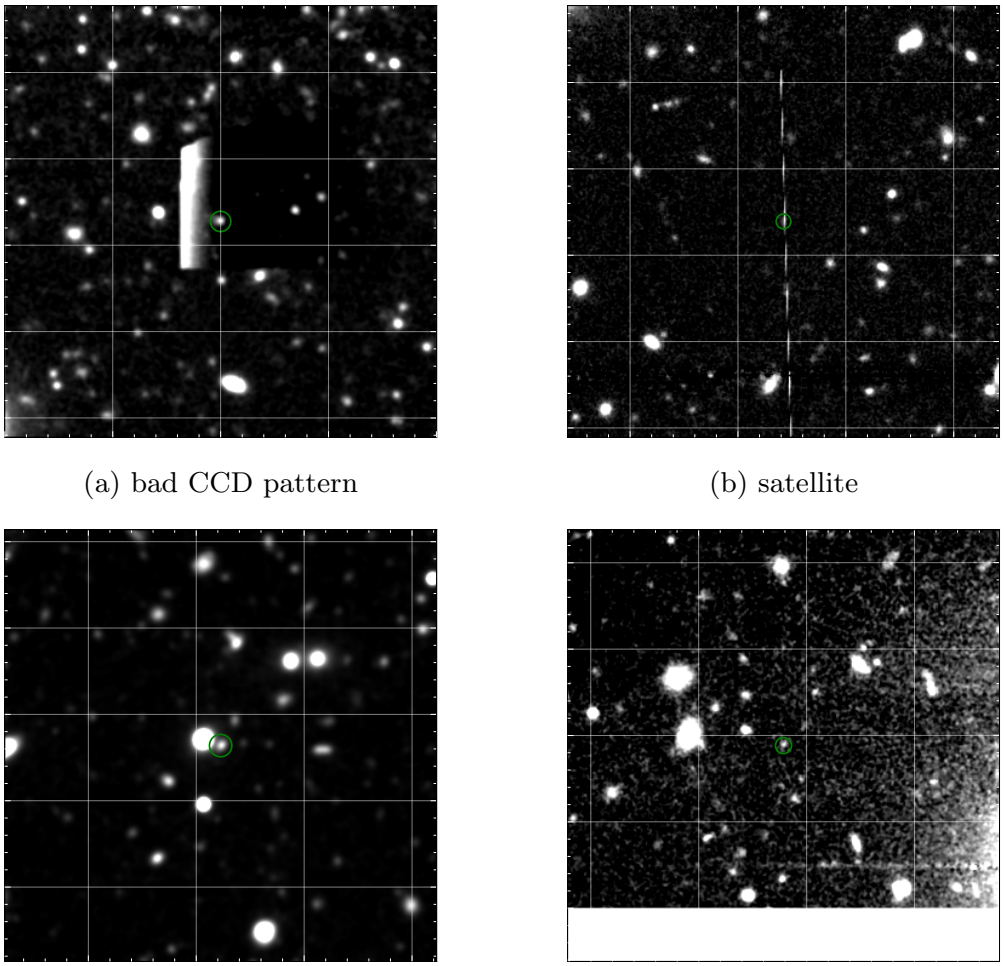

(a) bad CCD pattern

(b) satellite

(c) neighbor object

(d) bright object

Fig 2.7: Postage stamp images of bogus samples. The image size is 1 square arcmin. The green circle in each image show the aperture size.

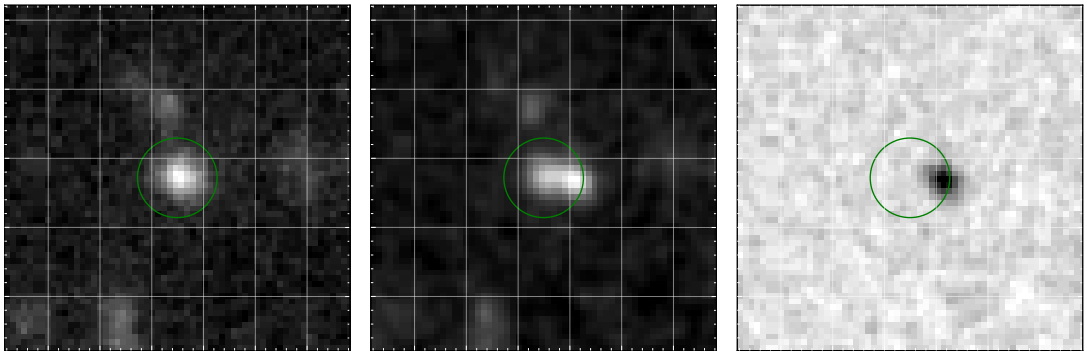

(a) g-band [2014-11-18] (b) g-band [2017-02-01] (c) subtracted

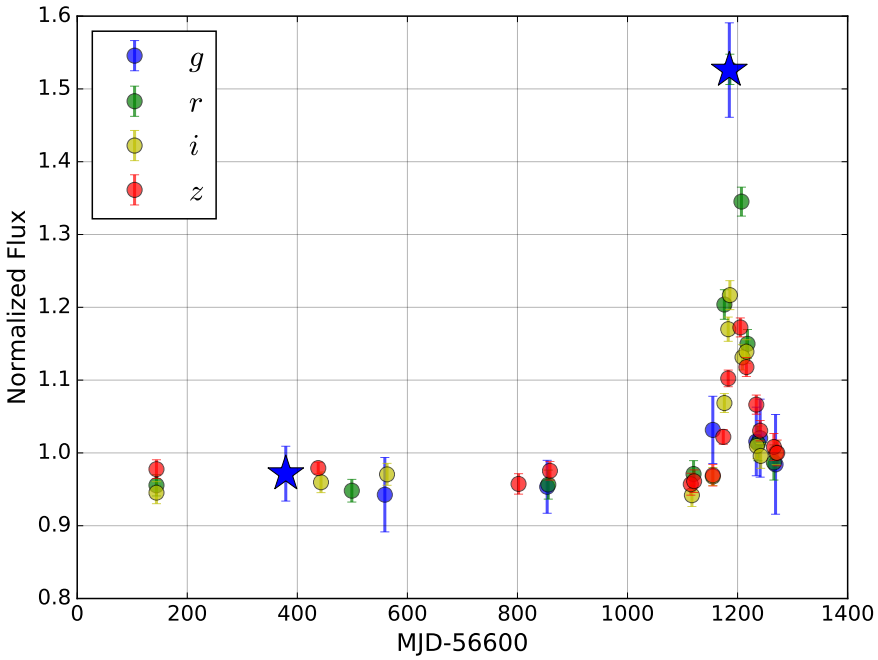

(d) light curve

Fig 2.8: Postage stamp images and light curve of a supernova. These image sizes in the left two are 10 square arcseconds. Green circles plotted on each image correspond to the aperture size analyzed here. Star symbols in the light curves are the dates shown in the left two images (a) and (b).

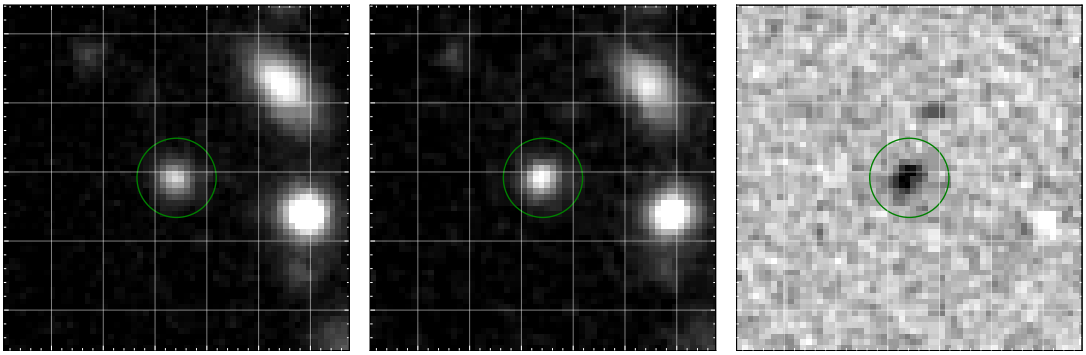

(a) i-band [2014-03-28] (b) i-band [2017-02-25] (c) subtracted

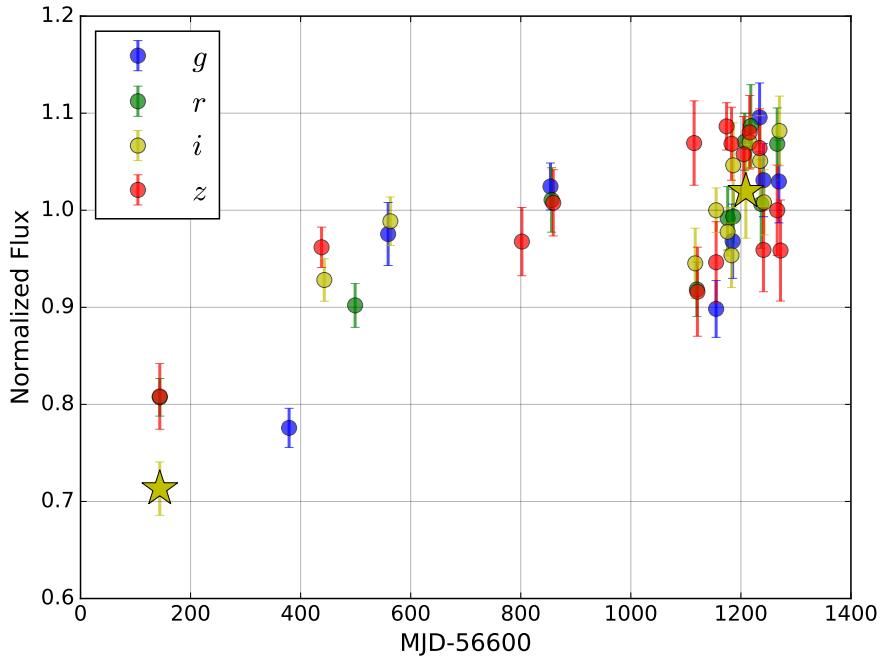

(d) light curve

Fig 2.9: Postage stamp images and light curve of a X-ray detected AGN. The image sizes in the left two are 10 square arcseconds. Green circles plotted on each image correspond to the aperture size analyzed here. Star symbols in the light curves are the dates shown in the left two images (a) and (b).

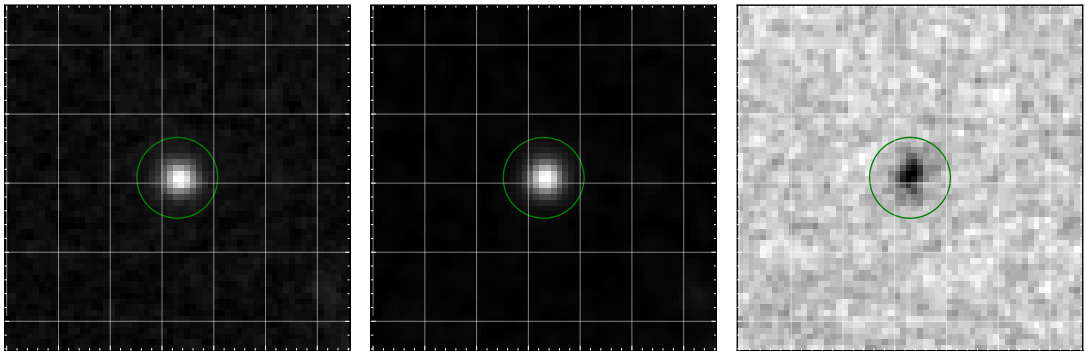

(a) i-band [2014-03-28] (b) i-band [2017-03-04] (c) subtracted

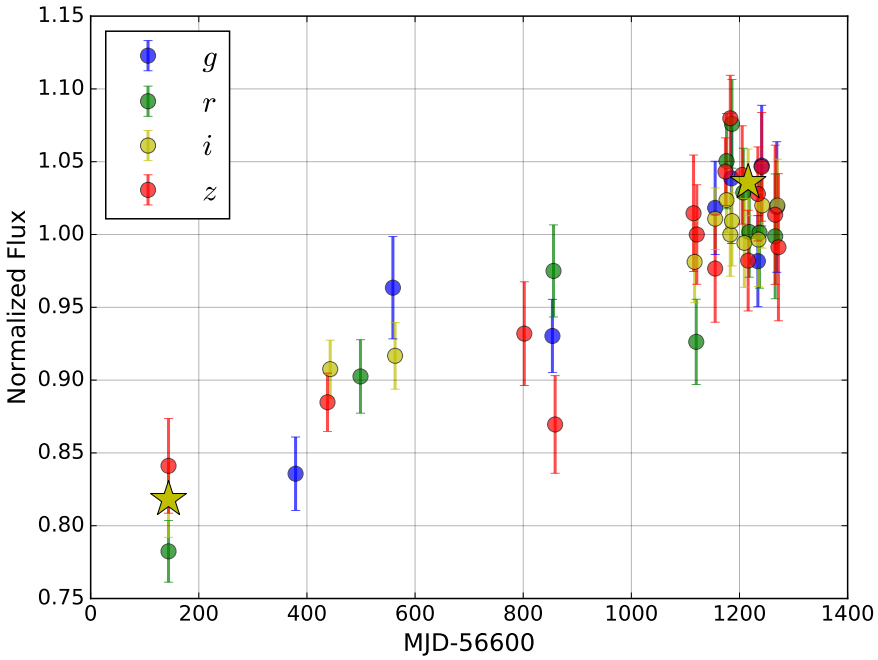

(d) light curve

Fig 2.10: Postage stamp images and light curve of a X-ray undetected AGN. The image sizes in the left two are 10 square arcseconds. Green circles plotted on each image correspond to the aperture size analyzed here. Star symbols in the light curves are the dates shown in the left two images (a) and (b).

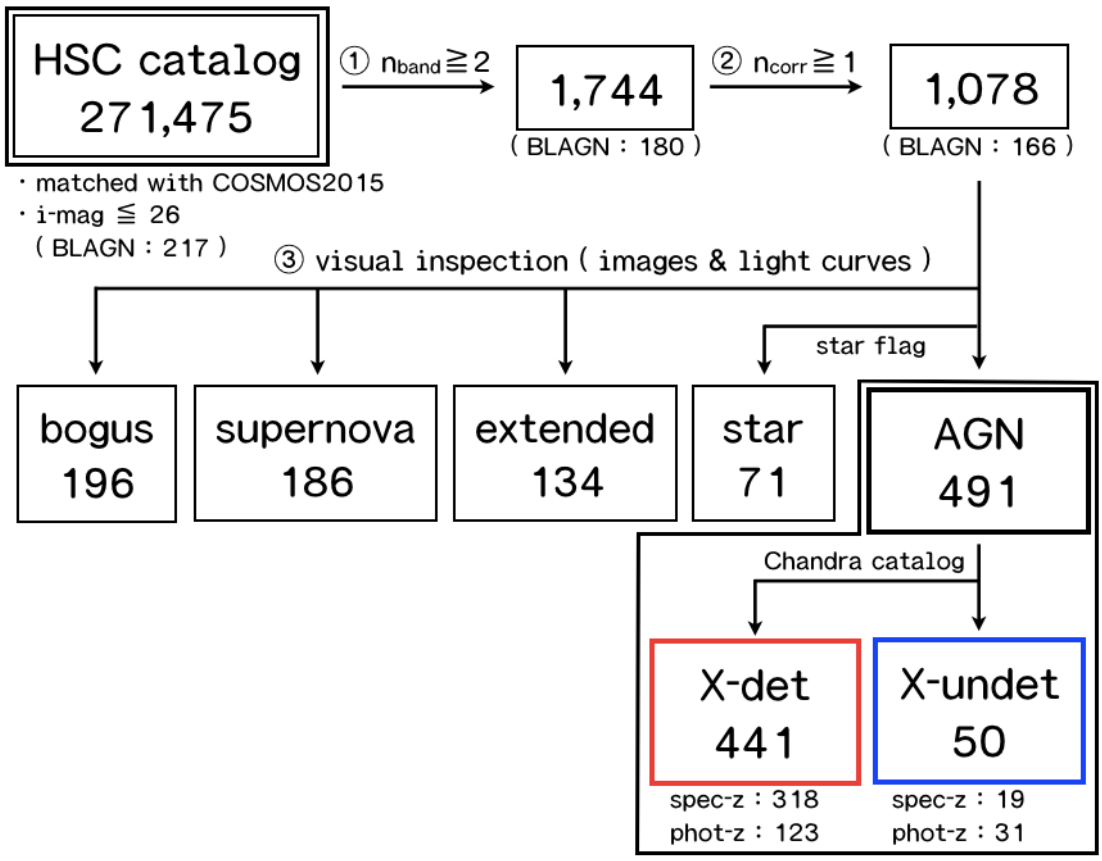

Fig 2.11: Flowchart of identifying variable AGNs in our method.

2.3.4 Comparison with the Previous Variability Survey

To check consistency of our variability method with other variability methods for variability search, we compare our sample of variability AGNs to the previous results. In the COSMOS field, variability surveys were conducted by using data from the PanSTARRS1 (PS1) survey (Simm et al., 2015) and the VLT Survey Telescope (VST) survey (De Cicco et al., 2019).

Simm et al. (2015) carried out optical variability analysis for X-ray detected QSOs which have a secure optical counterpart and have point-like light profile, using the PS1 data in the 5 broad bands ($g_{\rm P1}$, $r_{\rm P1}$, $i_{\rm P1}$, $z_{\rm P1}$, $y_{\rm P1}$) covering a period of about four years from November 2009 to March 2014, obtained as a part of the 3π survey and the Medium Deep Field (MDF04) survey (Chambers et al., 2016). The depth (5σ median limiting magnitude) of each survey is 22.1 ($g_{\rm P1}$), 21.9 ($r_{\rm P1}$), 21.6 ($i_{\rm P1}$), and 19.9 ($y_{\rm P1}$) for individual 3π survey data and 22.5 ($g_{\rm P1}$), 22.3 ($r_{\rm P1}$), 22.0 ($i_{\rm P1}$), and 21.3 ($y_{\rm P1}$) for individual MDF04 survey data, respectively. 90 ($g_{\rm P1}$), 54 ($r_{\rm P1}$), 14 ($i_{\rm P1}$), 37 ($z_{\rm P1}$), 8 ($y_{\rm P1}$) sources among 285 X-ray detected objects in the 3π survey data and 184 ($g_{\rm P1}$), 181 ($r_{\rm P1}$), 162 ($i_{\rm P1}$), 131 ($z_{\rm P1}$), 74 ($y_{\rm P1}$) sources among 331 X-ray detected objects in the MDF04 survey data are identified as variable AGNs.

De Cicco et al. (2019) carried out r-band variability-based AGN search using the data from the VST survey (the 5σ depth of single visits are $r \lesssim 24.6$ mag) from late 2011 to early 2015 with 54 visits. They find 299 optically variable AGN candidates (1.3% of main sample) among which 232 sources are high-confidence candidates with $r \leq 23.5$ mag.

Inside of our survey field (Figure 2.1), there are 116 PS1 variable AGNs and 235 VST variable AGNs. We cross-match these objects with our variable AGNs and find that almost all PS1 variable AGNs (115/116) and 83% of VST sample (194/235) are matched with our variable AGNs. The recovery rate for the VST sample is low, but we should note that the VST sample can be contaminated by false-positive variable sources (45 out of the 235 VST objects are low-confidence variable AGNs; see De Cicco et al., 2019). If we consider only high-confidence

sample (190 objects), 90% (173/190) of the VST sample are matched to our variability-selected AGNs. These results suggest that our variable AGN sample recovers more than 90% of the previous variable AGN samples at $r \lesssim 23.5$.

The final catalog of our all variability selected AGNs are summarized in Appendix D, and in the following section we focus on only these objects.

3 Properties of Variability-Selected AGNs

3.1 Basic Information

We obtained 491 variable AGN candidates, 441 ($\sim 90\%$) of which are detected in the X-ray (hereafter **X-det** sample) and the other 50 ($\sim$ 10%) are X-ray undetected (**X-undet** sample). Figure 3.1 shows the standard deviations σ_m of the g-band light curves for the 491 variable AGN candidates and the 271475 parent sample (Section 2.2.1), where σ_m for each object is defined as:

$$\sigma_m^2 = \frac{1}{n_{\rm epoch}} \sum_i^{n_{\rm epoch}} \left(m_i - \langle m(t) \rangle \right)^2, \tag{3.1.1}$$

where m_i is the magnitude at i-th epoch, $\langle m(t) \rangle$ is the time-averaged magnitude, and $n_{\rm epoch}$ is the number of epochs in which a target is not flagged as *faint* nor *neighbor* described in Section 2.2.3. As shown in Figure 3.1, almost all of our variable AGNs (both X-det and X-undet samples) show more than 95-th percentile of the distribution of σ_m.

The i-band magnitude histogram of our variable AGN sample is shown in Figure 3.2. The depth of the HSC SSP survey enable us to identify robust sample of variable objects down to $i \sim 25$ mag, which is more than a few magnitude deeper than the previous time-domain surveys in the COSMOS field, such as PS1 and VST surveys (Section 2.3.4). The median magnitudes of X-det and X-undet samples are 21.87 and 22.69, respectively. This suggests that X-ray fainter sources have fainter optical emission. We also plot the redshift distribution of our variable AGNs in Figure 3.3. The redshift information are obtained from the spectroscopic redshift ($z_{\rm spec}$) information in the HSC catalog (including zCOSMOS DR3 (Lilly et al., 2009), PRIMUS DR1 (Coil et al., 2011; Cool et al., 2013), VVDS (Le Fèvre et al., 2013), SDSS DR12 (Alam et al., 2015), FMOS-COSMOS (Silverman et al., 2015), 3D-HST (Momcheva et al., 2016)) and the DEIMOS 10K Spectroscopic Survey Catalog (DEIMOS catalog; Hasinger et al.,

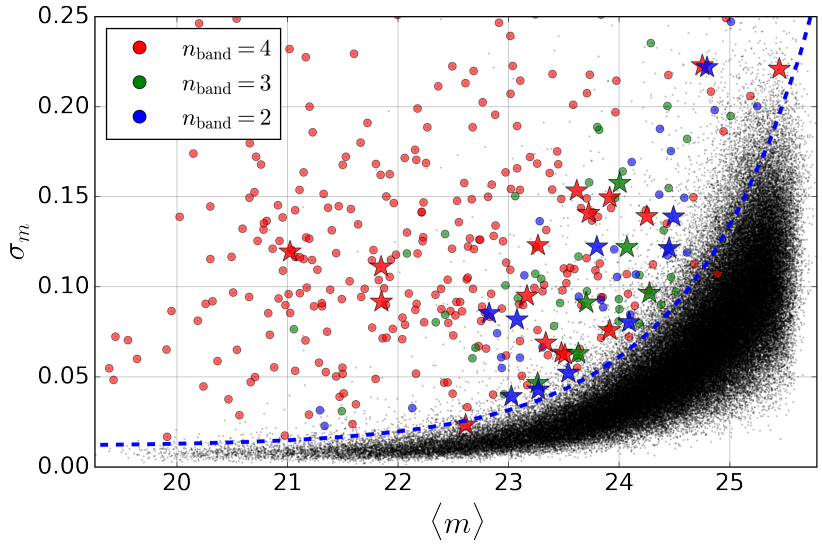

Fig 3.1: Standard deviation σ_m of the g-band light curve. The black points are the parent sample and the colored points are the variable AGNs with 4 (red), 3 (green), 2 (blue) *variability*-flagged bands. The blue dashed line is the 95-th percentile of the distribution of σ_m as a function of the time-averaged magnitude $\langle m(t) \rangle$. The round and star symbols are results for X-det sample and X-undet sample, respectively. These objects are plotted for only the objects which are detected $S/N \geq 5$ in all dates.

2018). If there is no spectroscopic information, for the X-det objects, we use the `z_best` values in the Chandra catalog which are photometric redshifts obtained by the SED fitting with galaxy and AGN hybrid SED templates. The typical uncertainty of these photometric redshifts is $\sigma_{\Delta z/(1+z_{\rm spec})} \sim 0.03$ and a fraction of outliers is $< 8\%$ (Marchesi et al., 2016). For X-undet objects, we use the `ZPDF` values in the COSMOS2015 catalog, which are obtained by SED fitting with only galaxy templates. The uncertainty for these photometric redshifts is $\sigma_{\Delta z/(1+z_{\rm spec})} \lesssim 0.1$ for $i < 24$ mag (Laigle et al., 2016).

337 objects (69%) have the spectroscopic redshifts. 123 objects (25%) have the photometric redshifts by the galaxy-AGN hybrid templates, and 31 objects (6%) have the photometric redshifts by the galaxy templates. Our sample covers a wide range of rest-frame time-interval and wavelength where the highest redshift object is at $z = 4.26$.

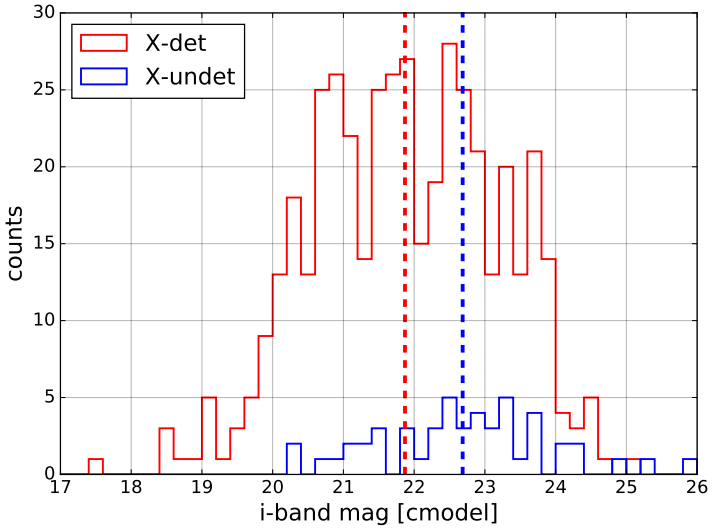

Fig 3.2: Histograms of i-band magnitude for our variable AGN samples. The red (blue) histogram is the distribution of X-ray detected (undetected) objects in our variable sample. The vertical dashed lines are the median values for each sample.

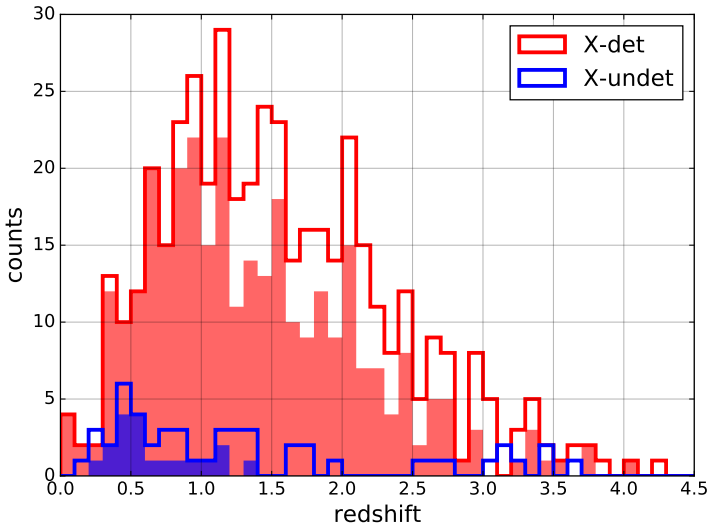

Fig 3.3: Redshift distributions for our variable AGN sample. The red (blue) histogram is the distribution of the X-ray detected (undetected) objects in our variable sample. Spectroscopic redshift distributions are shown in filled histograms.

Figure 3.4 shows the AGN bolometric luminosity as a function of redshift of our variable AGN sample. The results of the X-ray stacking for X-undet samples are also shown with the blue points with error bars. The method of the X-ray stacking analysis is described in the next subsection in detail. The bolometric luminosity is calculated from the X-ray luminosity assuming the luminosity-dependent bolometric collection factor (Lusso et al., 2012). To calculate the bolometric luminosity, we use the hard-band (2-10 keV) luminosities if available and use the soft-band (0.5-2 keV) luminosities for the hard X-ray undetected objects. The bolometric luminosity range of our variable sample is $10^{43.0-46.5}$ erg s^{-1}.

Using our variable AGN sample, we can investigate AGN variability properties over a wide range of rest-frame time intervals of 1-1000 days, rest-frame wavelengths of 1000-5000 Å, and the AGN bolometric luminosities of $10^{43.0-46.5}$ erg s^{-1}, which will be discussed in Section 4.

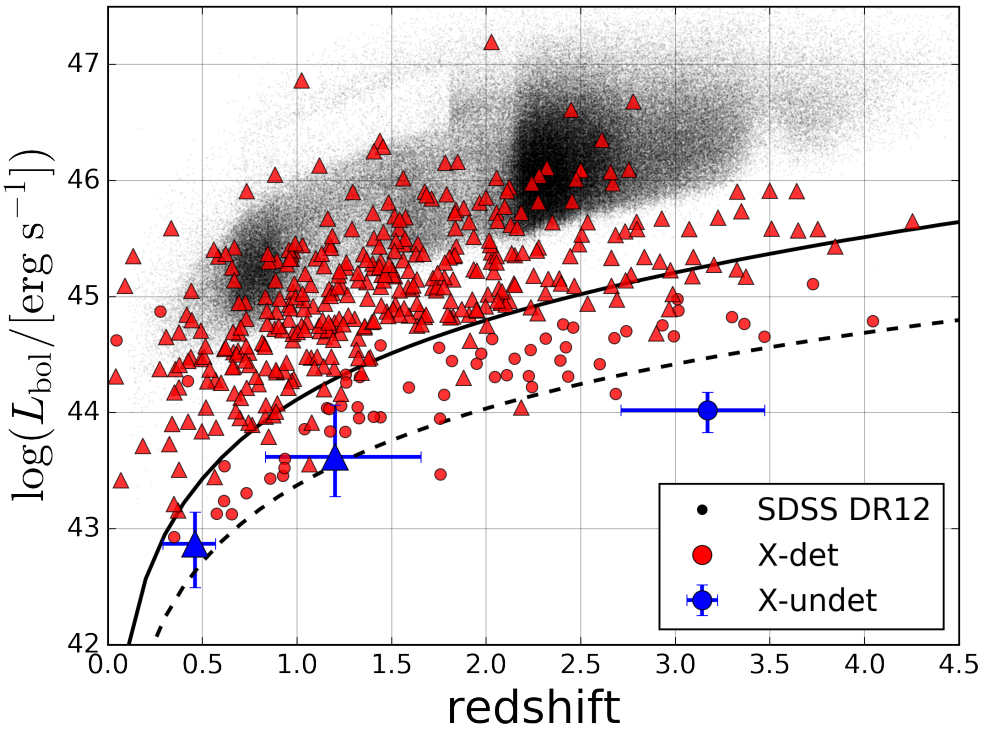

Fig 3.4: Redshift distributions for our variable AGN sample. The luminosities calculated from the hard (soft) band X-ray luminosity are shown as triangle (circle) symbol. The red (blue) points are X-ray detected (undetected) samples. The X-ray undetected samples are calculated from the stacking analysis described in section 3.2.3. The solid (dashed) line is the Chandra flux limit of hard (soft) band (20% completeness; Civano et al., 2016). The black points are data set of SDSS Quasar DR12 taken from Kozłowski (2017).

3.2 Stacking Analysis for X-ray Undetected Variable AGNs

3.2.1 Stacking Analysis

In this subsection, we focus on the X-undet objects (50 out of 491 our variable AGN sample). They are probably AGNs with lower X-ray flux than the Chandra detection limit for individual sources. We check their statistical X-ray properties by using the Chandra X-ray stacking analysis tool, CSTACK v4.32 (Miyaji et al., 2008)[*4]. Using 117 observations from the Chandra COSMOS Legacy survey data (the total exposure time is 4.8 Ms; Civano et al., 2016), CSTACK can calculate exposure-weighted mean X-ray count rates in the soft (0.5-2 keV) and hard (2-8 keV) bands by stacking Chandra images centered at given sky positions.

Since the number of the X-undet objects is limited, we divide the X-undet objects into three redshift bins; $z \leq 0.7$, $0.7 < z \leq 2.0$, and $z > 2.0$, where the median redshifts are $z_{\rm med} = 0.46$, 1.20, and 3.17, respectively (see Figure 3.5, Table 3.1).

We briefly show how to calculate the stacked source count rate in the CSTACK analysis (please see the manual pages in detail). First CSTACK collect the observational data which has the object's off-axis angles at the input coordinates are below the `maxoff` value (8 arcmin by default). In this time, CSTACK remove the data which are heavily affected by the X-ray source listed in the catalog of the Chandra Legacy Survey. Then CSTACK calculate the source counts within the circle defined by the radius parameter of `src_rad`. Since the Chandra PSF with the off-axis angle varies, this radius is defined the 90% enclosed counts fraction radius (r_{90}) by default, with a minimum of 1.0 arcsec and a maximum of inner radius parameter for background counting of `bkg_rad`. The background counts are estimated from a circular annulus with the inner radius of `bkg_rad` (7 arcsec by defalt) and the outer radius of `img_size` (30 arcsec by default) centered at the input coordinates. Also CSTACK extracts the mean exposure time of objects and background fields. After subtraction of background count,

[*4] http://cstack.ucsd.edu/ or http://lambic.astrosen.unam.mx/cstack/

Table 3.1: The statistical properties of stacked samples

bins	$N_{stacked}$	Exp. (ks)	z_{med}	$\log(M_{\star,med})$ ($M_\odot$)	$\log(SFR_{med})$ ($M_\odot$ yr^{-1})
(1)	(2)	(3)	(4)	(5)	(6)
$z \leq 0.7$	18	1,855	0.46	10.05	0.53
(low mass)	9	915	0.34	9.10	0.14
(high mass)	9	940	0.51	10.61	0.75
$0.7 < z \leq 2.0$	22	2,330	1.20	10.08	1.18
(low mass)	11	1,225	1.29	9.14	0.97
(high mass)	11	1,105	1.18	10.58	1.73
$z > 2.0$	10	967	3.17	10.28	1.89

(1) Stacked bin.
(2) The number of stacked samples.
(3) Total exposure time in stacked image.
(4) The median redshift in the stacked sample.
(5) The median stellar mass in the stacked sample.
(6) The median star formation rate in the stacked sample.

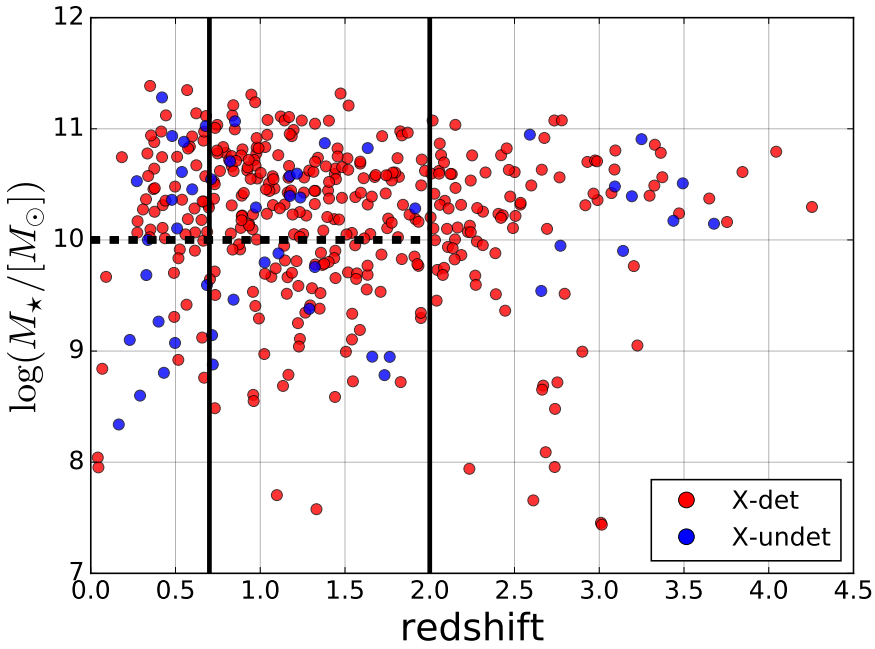

Fig 3.5: Stellar mass as a function of redshift for our variability samples. The red and blue points are X-det sample and X-undet sample, respectively. The CSTACK samples are divided into 3 bins for the redshift (the black solid lines) and into 2 bins for the stellar mass (the dashed line).

the source count rate is corrected for the fraction of the PSF that falls into the extraction radius (r_{90}). Finally CSTACK calculates the exposure-weighted mean of the net source count rates. To check the significance of the stacked count rates, CSTACK conducts a bootstrap re-sampling analysis that provides the distribution of the stacked count rates for 500 re-sampled catalogs, each of which consists of the same number of objects as the input objects and selected at random from the input objects allowing duplicates. In our analysis, we choose the default parameters in the CSTACK analysis.

The results of the CSTACK X-ray stacking analysis are summarized in Table 3.2 and postage stamps of the staked X-ray images are shown in Figure 3.6. X-ray emissions are statistically detected ($S/N \geq 2$) in the lowest redshift bin sample in both band, $0.7 < z \leq 2.0$ bin sample in hard-band, and $z > 2.0$ bin sample in soft-band. We then obtain the X-ray flux from the stacked X-ray count rates by adopting the conversion factor from the PIMMS[*5] utility. The conversion factor[*6] from 0.5-2 keV (2-8 keV) count rate to 0.5-2 keV (2-10 keV) X-ray band flux is 6.563×10^{-12} erg cm^{-2} count^{-1} (2.784×10^{-11} erg cm^{-2} count^{-1}), where a power-law photon index $\Gamma = 1.4$ and a Galactic column density of $N_{\rm H} = 2.6 \times 10^{20}$ cm^{-2} (Kalberla et al., 2005) are assumed. The choice of the power-law photon index $\Gamma = 1.4$ is not only because of consistency with Civano et al. (2016), but it is also the slope of the cosmic X-ray background (Hickox & Markevitch, 2006). For each redshift bin, the observed X-ray flux is converted to rest-frame flux by using a k-correction factor $(1 + z_{\rm med})^{\Gamma-2}$. We finally derive the X-ray luminosity for each band and the bolometric luminosity using the luminosity distance at $z_{\rm med}$ and the luminosity-dependent bolometric collection factor (Lusso et al., 2012). The results are summarized in Table 3.2 and plotted as the blue points in Figure 3.4. As shown in Figure 3.4, we conclude that the X-undet samples indeed have the lower flux than the Chandra detection limit.

[*5] http://cxc.harvard.edu/toolkit/pimms.jsp

[*6] We use the ACIS-I response for Chandra Cycle 14.

Table 3.2: Stacking results for each bin

bins	soft-band CR (0.5-2 keV) (μ counts s^{-1})	S/N	soft-band $\log(L_{0.5\text{-}2\mathrm{keV}})$ (erg s^{-1})	hard-band CR (2-8 keV) (μ counts s^{-1})	S/N	hard-band $\log(L_{2\text{-}10\mathrm{keV}})$ (erg s^{-1})	$\log(L_{\mathrm{bol}})$ (erg s^{-1})
(1)	(2)	(3)	(4)	(2)	(3)	(4)	(5)
$z \leq 0.7$	$9.18^{+3.85}_{-4.12}$	2.1	$40.59^{+0.31}_{-0.42}$	$30.8^{+7.75}_{-9.93}$	3.5	$41.75^{+0.28}_{-0.39}$	$42.88^{+0.28}_{-0.39}$
(low mass)	$4.54^{+4.99}_{-4.73}$	< 1.0	< 40.32	$32.6^{+13.2}_{-17.1}$	2.2	$41.49^{+0.48}_{-0.35}$	$42.62^{+0.48}_{-0.35}$
(high mass)	$13.1^{+7.17}_{-6.22}$	1.9	< 41.04	$29.9^{+11.4}_{-10.2}$	2.9	$41.84^{+0.23}_{-0.21}$	$42.97^{+0.23}_{-0.21}$
$0.7 < z \leq 2.0$	$6.09^{+4.84}_{-5.05}$	1.2	< 41.58	$20.4^{+6.58}_{-6.43}$	3.1	$42.48^{+0.45}_{-0.35}$	$43.62^{+0.45}_{-0.35}$
(low mass)	$-4.23^{+3.40}_{-3.11}$	< 1.0	< 41.15	$21.9^{+11.3}_{-9.80}$	2.1	$42.58^{+0.41}_{-0.44}$	$43.71^{+0.41}_{-0.44}$
(high mass)	$18.1^{+8.54}_{-6.61}$	2.4	$41.79^{+0.35}_{-0.34}$	$18.1^{+8.48}_{-8.69}$	2.2	$42.41^{+0.35}_{-0.36}$	$43.54^{+0.35}_{-0.36}$
$z > 2.0$	$23.0^{+8.98}_{-8.00}$	2.6	$42.77^{+0.20}_{-0.21}$	$15.8^{+8.61}_{-7.10}$	1.9	< 43.43	$^{*}44.01^{+0.20}_{-0.21}$

(1) Stacked bin.
(2) Net source count rates for each band (0.5-2 keV, 2-8 keV).
(3) Signal to noise ratio for each band.
(4) X-ray luminosities for each band (0.5-2 keV, 2-10 keV).
(5) Bolometric luminosity calculated from stacked hard band X-ray luminosity.
For the lower S/N data (S/N < 2), the luminosities are calculated from the $+1\sigma$ variation of the noise value. Asterisk symbol in the column (5) means that the bolometric luminosity is calculated from the soft band luminosity due to low S/N of hard band X-ray luminosity.

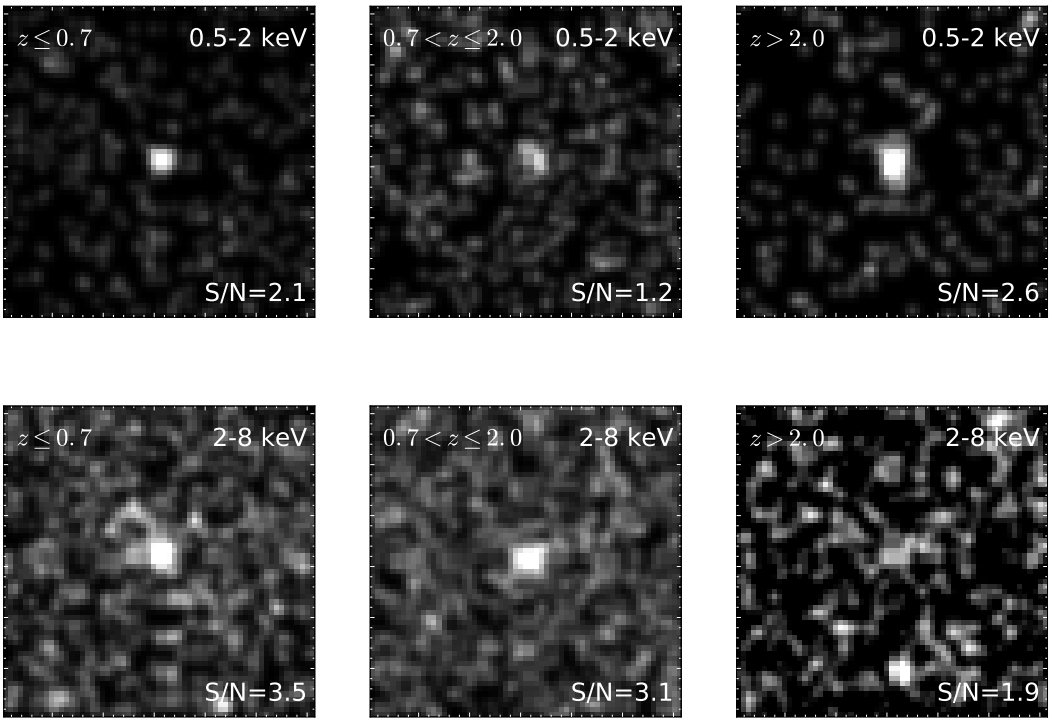

Fig 3.6: Stacked images for each redshift bin.

3.2.2 Other X-ray Contributions

In addition to the AGN emission, X-ray binaries (XRBs) in the AGN host galaxies can also be the sources of the observed X-ray emission. The X-ray contribution from XRBs consists of radiations from low mass XRBs and high mass XRBs, and their total luminosities are proportional to the stellar mass ($M_\star$) and the star formation rate (SFR) of the host galaxy. Lehmer et al. (2016) investigate the redshift dependence of the contributions of the XRBs in normal galaxies, and provide the following empirical relation:

$$L^{\rm XRB}_{2-10{\rm keV}} = \alpha(1+z)^\gamma \left(\frac{M_\star}{M_\odot}\right) + \beta(1+z)^\delta \left(\frac{\rm SFR}{M_\odot\ {\rm yr}^{-1}}\right) \quad [{\rm erg\ s}^{-1}], \tag{3.2.1}$$

where $\log\alpha = 29.30 \pm 0.28$, $\log\beta = 39.40 \pm 0.08$, $\gamma = 2.19 \pm 0.99$, $\delta = 1.02 \pm 0.22$, and the scatter of 0.17 dex (the best-fit values for the 6 Ms Chandra Deep Field South data, see Lehmer et al., 2016). We adopt the median values of redshift, stellar mass, and SFR to evaluate the contributions of the XRBs to the X-undet samples. We use the stellar mass and SFR from `MASS_BEST` and `SFR_BEST` values listed in the COSMOS2015 catalog, which are products of a SED fitting (Laigle et al., 2016). The median values of the stellar mass and SFR for each redshift bin are summarized in Table 3.1. From these values, X-ray contributions from XRBs are $\log(L_{\rm 2\text{-}10keV}/[{\rm erg\ s}^{-1}]) = 40.2$, 41.0, and 42.0 for $z \leq 0.7$, $0.7 < z \leq 2.0$, and $z > 2.0$ bin, respectively. The contributions of XRBs are about 1.5 dex fainter than the stacked hard-band luminosities ($\sim 3\%$ in the stacked luminosities, see Table 3.2), indicates that the stacked hard-band X-ray luminosities are dominated from the X-ray emission from nucleus.

Another possible source of the X-ray emission is thermal plasma ($\sim$sub-keV temperature) in the AGN host galaxy inter-stellar medium (ISM), which mainly contributes to the soft-band X-ray luminosity. Since this diffuse X-ray emission

arises from collective effects of supernova remnants and winds from massive stars, the soft-band X-ray luminosity depends on the SFR. Mineo et al. (2012) derive an empirical relationship between the diffuse X-ray luminosity and SFR for nearby late-type galaxies as:

$$L^{\rm Hot}_{0.5-2{\rm keV}} = (8.3 \pm 0.1) \times 10^{38} \left(\frac{\rm SFR}{M_\odot \ {\rm yr}^{-1}} \right) \ \ [{\rm erg \ s}^{-1}], \qquad (3.2.2)$$

with an intrinsic scatter of 0.34 dex. From this equation, we calculate the effect of the ISM diffuse X-ray emission in the soft-band X-ray luminosity for our stacked samples. Using the median SFR value in each redshift bin (Table 3.1), we estimate the X-ray contributions from the hot ISM, $\log(L_{0.5\text{-}2{\rm keV}}/[{\rm erg \ s}^{-1}]) = 39.4$, 40.1, and 40.8 for $z \leq 0.7$, $0.7 < z \leq 2.0$, and $z > 2.0$ bin, respectively, shows that the soft-band X-ray contributions from the ISM diffuse X-ray emissions are about 1 dex fainter than the stacked soft-band X-ray luminosities ($< 10\%$ in the stacked luminosities, see Table 3.2).

It should be noted that Ultra Luminous X-ray sources (ULXs) may also contribute to the stacked X-ray emission in the X-undet samples. ULXs are usually defined as off-nuclear point-like X-ray sources and typically have X-ray luminosities $> 10^{39}$ erg s^{-1} (e.g. Feng & Soria, 2011). The total X-ray luminosity of ULXs in elliptical galaxies are small ($< 10^{40}$ erg s^{-1}), while one third of spiral galaxies have luminosities $\geq 5 \times 10^{39}$ erg s^{-1} and about 10 % of ULSx have luminosities $> 10^{40}$ erg s^{-1} (Swartz et al., 2004; Walton et al., 2011). The X-ray luminosities of our samples, however, are still significantly higher than the expected ULX emission.

Thus the total X-ray luminosities from XRBs, hot ISM, and ULXs are too small to explain the stacked X-ray luminosities and the estimates suggest that X-ray emission of the stacked samples is dominated by the emission from AGNs.

3.2.3 Hardness Ratio

For the stacked samples, we calculate the Hardness Ratio defined as:

$$HR = \frac{H - S}{H + S} \tag{3.2.3}$$

where H and S are the net source count rates in the hard-band (2-8 keV) and the soft-band (0.5-2 keV), respectively. The HR reflects the shape of the X-ray spectrum that can be characterized by the intrinsic power-law photon index Γ, absorption column density $N_{\rm H}$, and redshift. To calculate HR, we use the Bayesian Estimation of Hardness Ratios (BEHR) tool (Park et al., 2006). Input parameters for calculating HR in the BEHR tool are used from the outputs of the CSTACK analysis. The input parameters and the results of HR are summarized in Table 3.3.

Figure 3.7 shows the HR distribution as a function of redshift for the stacked samples, X-ray detected variable objects, and the X-ray detected non-variable objects in the Chandra catalog. The median value of HR for the X-ray detected variable objects is -0.33, which is softer than the median value of HR for the X-ray detected non-variable objects; -0.07.

It is interesting to note that the stacked X-undet samples have higher HR values than most of the X-det objects in our variable AGN sample and comparable to the X-ray detected non-variable objects. This can be interpreted that there is a significant amount of X-ray absorbing materials in the line of sight which absorb X-ray photons in lower energy band ($\lesssim 5$ keV).

We also divide the X-undet variable samples into two sub-samples by the stellar mass. Since the number of X-undet objects is limited, we here use the X-undet objects at $z \leq 2$ (Figure 3.5). The CSTACK X-ray stacking results for the low mass ($M_\star < 10^{10} M_\odot$) and high mass ($M_\star \geq 10^{10} M_\odot$) sub-samples are shown in Table 3.2 and Figure 3.8. Statistically significant ($S/N > 2$) X-ray signals are still detected in the hard-band for all the stacked bins, but X-ray signal is

Table 3.3: BEHR inputs and outputs

bin	soft-band (0.5-2 keV)			hard-band (2-8 keV)			HR
	`softsrc` (counts)	`softbkg` (counts)	`softarea` (pixels)	`hardsrc` (counts)	`hardbkg` (counts)	`hardarea` (pixels)	
(1)	(2)	(3)	(4)	(2)	(3)	(4)	(5)
$z \leq 0.7$	36	275	12.48	122	775	10.30	$0.54^{+0.21}_{-0.16}$
(low mass)	13	127	12.84	60	377	10.55	> 0.68
(high mass)	23	148	12.03	62	398	10.12	$0.37^{+0.28}_{-0.30}$
$0.7 < z \leq 2.0$	40	352	12.77	139	1060	11.26	$0.59^{+0.22}_{-0.21}$
(low mass)	9	193	12.23	71	548	11.41	> 0.90
(high mass)	31	159	13.41	68	512	11.12	$0.048^{+0.32}_{-0.22}$
$z > 2.0$	30	152	15.76	53	475	13.07	$-0.14^{+0.33}_{-0.26}$

(1) Stacked bin.
(2) Source counts.
(3) Background counts.
(4) Effective aperture area.
(5) Hardness ratio.

detected in the soft-band for only high-mass and high-redshift bin. The HRs of these sub-samples are also plotted in Figure 3.7 (yellow points with error bars). It is found that the low mass sub-samples show harder X-ray spectra than those of the high mass subsamples in both of the redshift bins. The PIMMS utility shows that if we assume the Galactic column density $N_{\rm H} = 2.6 \times 10^{20}$ cm^{-2} and the intrinsic photon-index $\Gamma = 1.8$ with the source column density $N_{\rm H} = 10^{22.5}$, $10^{23.0}$, $10^{23.5}$ cm^{-2}, the observed HRs are 0.268, 0.805, 0.996 at $z = 0.46$ and -0.096, 0.303, 0.812 at $z = 1.20$, respectively. These HR values are similar to our results for the X-undet samples (see Table 3.3 and Figure 3.7). From these results, we argue that X-undet sample contains a significant fraction of the X-ray obscured but optically unobscured (variable) type-I AGN and that the effects of absorption in X-ray is higher in lower mass bin sample. The physical interpretations of these X-ray obscured optically variable objects are discussed in Section 5.2.

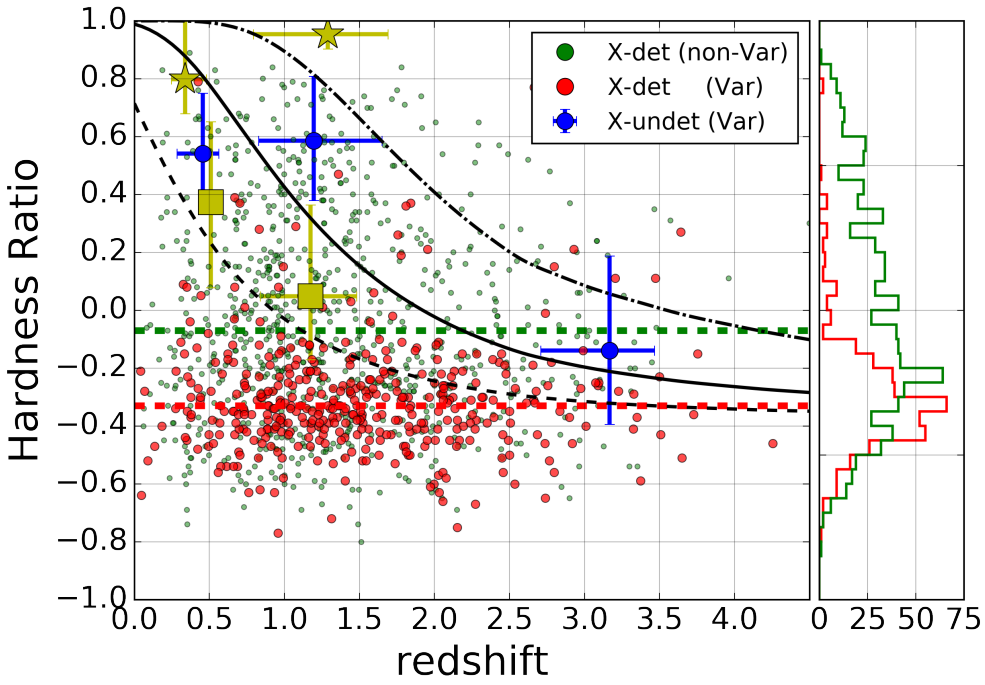

Fig 3.7: Hardness ratio as a function of redshift. The blue (red) points are results of X-ray detected (undetected) objects in our variability sample. The dashed lines are median values for each sample. The green points are results of our stacking analysis for X-ray undetected objects in our variability samples ($z \leq 0.7$, $0.7 < z \leq 2.0$, $z \geq 2$ bins). The yellow points are also results of our stacking analysis but for low mass (higher HR value) and high mass (lower one). The blue and red lines are the median values for variable and non-variable objects in X-ray detected objects, respectively. The black curve is the model prediction assuming the power low spectrum with the photon-index $\Gamma = 1.8$ and source column density $N_{\rm H} = 10^{22.5}$ cm^{-2} (dashed), 10^{23} cm^{-2} (solid), and $10^{23.5}$ cm^{-2} (dashed-dot), respectively. The histograms of HR for X-det variable samples and X-det non-variable samples are shown in the right side.

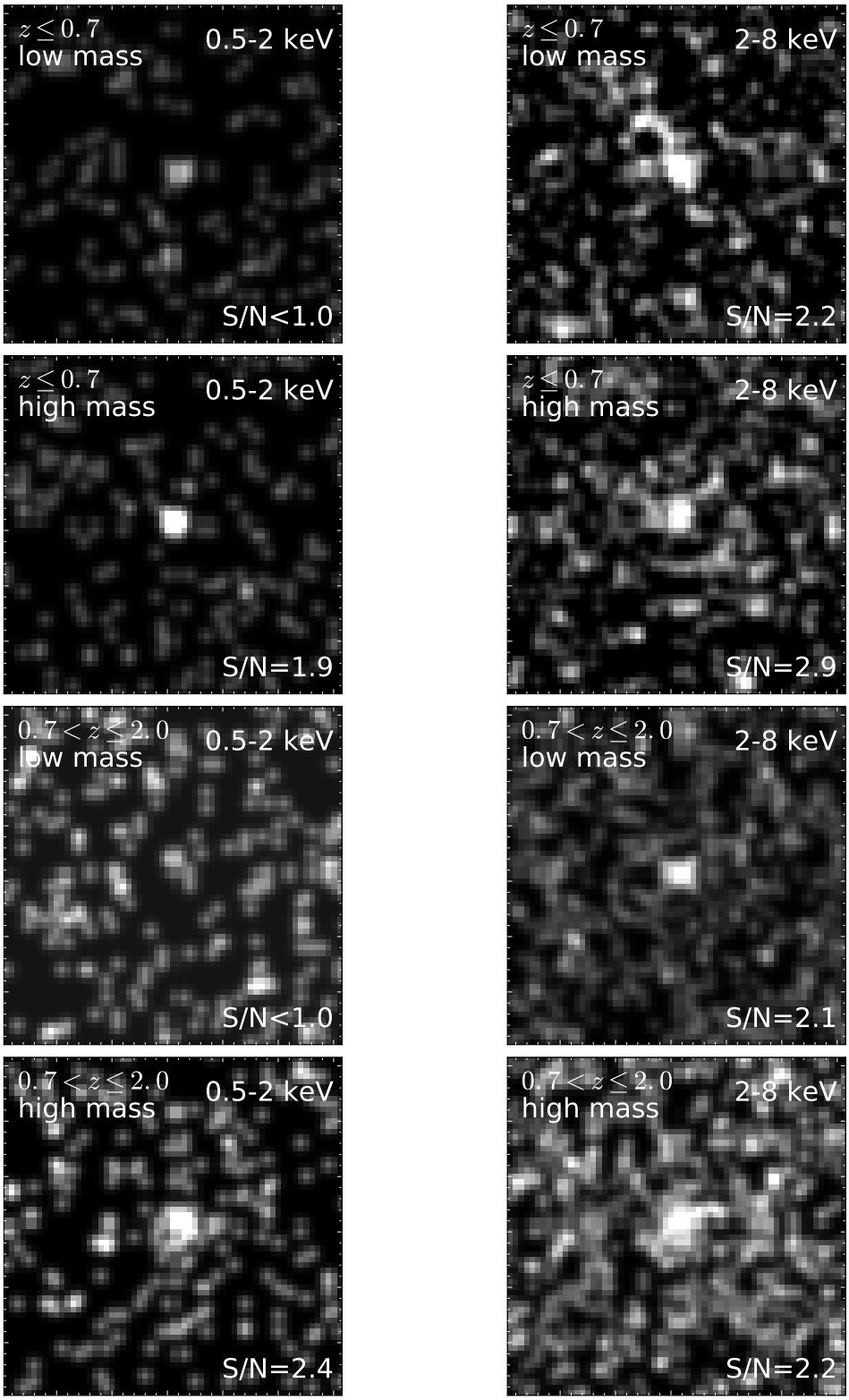

Fig 3.8: Stacked images for each redshift/stellar mass bin in each band (left: soft-band, right: hard-band).

3.3 Dust Covering Factor

The detection of the variability in AGNs means that we directly see UV-optical accretion disk emission, which is not obscured by AGN dust tori. The dust covering factor of AGNs, which is defined as a ratio of optically-obscured AGNs to the entire AGN population, can be constrained by a variability detection fraction among the X-ray detected AGNs.

Within our HSC variability survey area in the COSMOS field, 743 X-ray detected AGNs at $0.5 \leq z \leq 2.5$ (the redshift information is obtained in the same manner as described in Section 3.1) and brighter than the hard-band X-ray flux limit at 50% completeness level for the Chandra COSMOS Legacy survey, $f_{2-10\mathrm{keV}} = 3.1 \times 10^{15}$ erg s^{-1} cm^{-2} (Civano et al., 2016), have counterparts in our HSC parent sample (Section 2.2.1). The selected sample is shown in Figure 3.9. Among them, 284 are variable objects and the other 459 objects are non-variable objects. We then calculate the non-variable fraction in each hard-band X-ray luminosity bins of $\log(L_{2-10\mathrm{keV}}/[\mathrm{erg\ s^{-1}}]) =$ 42.5-43.0, 43.0-43.5, 43.5-44.0, and 44.0-44.5. The result is indicated by blue dashed line in Figure 3.10. As described in the Section 2.3.2, our variability selection method misses about 18% of the known BLAGNs. To correct for the number of unselected variable AGNs in our variability selection method, we calculate an fraction f_{corr}, defined as a fraction of non-variable BLAGNs among the known BLAGNs in each luminosity bin, and multiply a factor of $100/(100 - f_{\mathrm{corr}})$ to the number of the variable objects in each luminosity bin. The corrected covering factors are shown as blue points with error bars in Figure 3.10. The error bars are calculated from the Poisson errors of the number of samples.

The derived fraction shows a similar trend as that obtained by Merloni et al. (2014) who select optically unobscured AGNs by spectroscopic detection of the broad emission lines (FWHM $\geq$ 2000 km s^{-1}) or photometrically unobscured AGNs by results of SED fitting (see also Salvato et al., 2011), and also shows a similar trend as X-ray absorbed fraction (Swift/BAT survey, see Ricci et al., 2017a,b; Ichikawa et al., 2019), whose classification of the X-ray absorbed sources

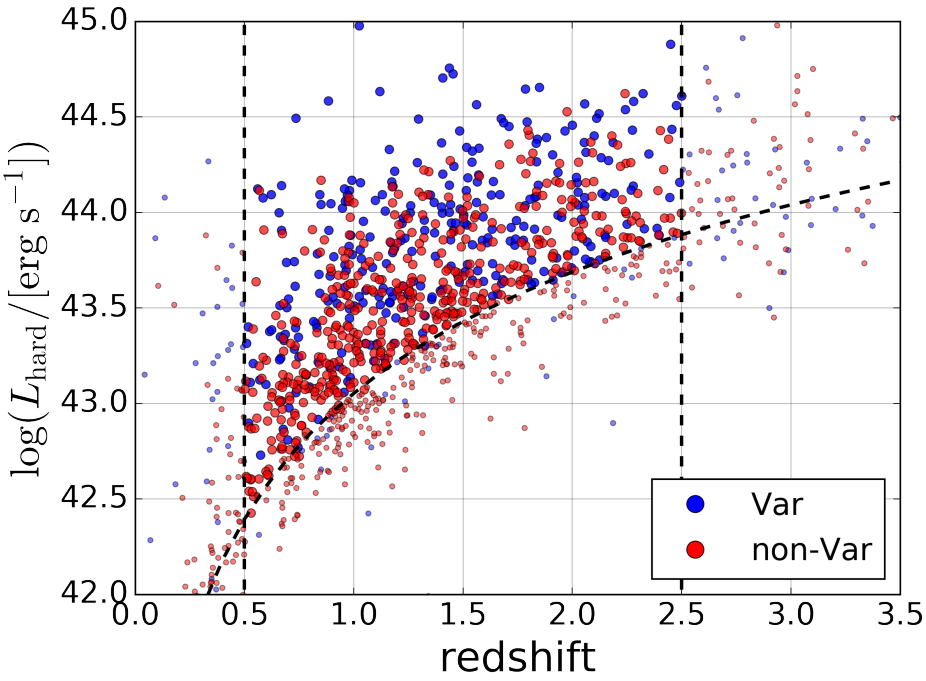

Fig 3.9: Hard-band X-ray luminosity of X-ray detected objects in the parent sample as a function of redshift. The big circles are selected samples for calculating the dust covering factor. The dashed lines are selection boundaries to construct more significant sample. The blue points correspond to X-det sample and the red points are X-ray detected non-variable objects.

is based on gas column densities from X-ray spectral fitting. Our variability-based covering factors show slightly lower values compared to the Merloni et al. (2014)'s covering factors. The difference indicates that the our variability-based AGN selection method is more efficiently selecting unobscured AGNs than the optical spectroscopic or photometric AGN selection method. We note that low black hole mass AGNs can have broad emission lines with the widths of FWHM less than 2000 km s^{-1} and such objects can be misclassified as optically obscured type-II AGNs in optical spectroscopy-based classification (see Section 1.3). The variability selection is independent of the line width of the broad emission line for unobscured AGNs, thus our results show lower dust covering factor than the results of Merloni et al. (2014).

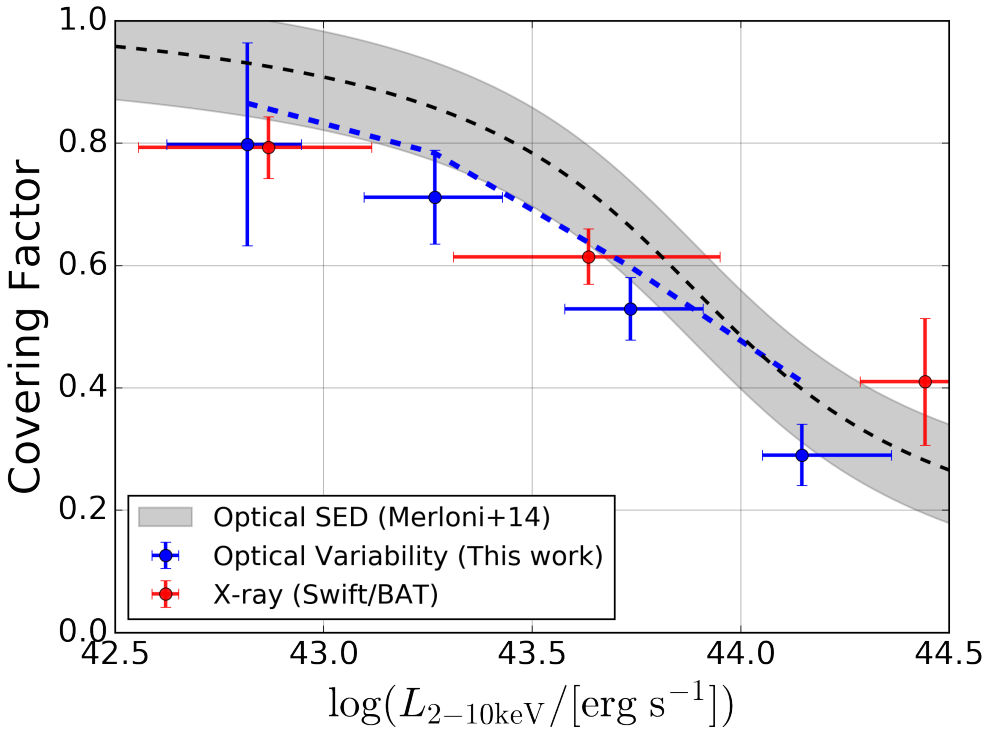

Fig 3.10: Covering factor as a function of AGN hard-band X-ray luminosity. The blue dashed line is a result obtained for our variable AGN sample and the blue points with error bars are values corrected for the detection rate of the known BLAGN in each luminosity bin. The black dashed line is the obscured fraction from the optical diagnostics (equation (1) in Merloni et al., 2014). The error range of the optical result (~ 0.08) is shown as the black shaded region. The red points with error bars are results of X-ray absorbed fraction from the Swift-BAT observations (Ricci et al., 2017a,b; Ichikawa et al., 2019).

3.4 Mid Infrared Color Diagnostics

In AGNs, radiation from hot/warm dust produces a mid-infrared (MIR) bump in the SED, while in normal galaxies, stellar continuum (e.g., 1.6 μm bump), PAH emission, and some warm dust radiation heated by the star-forming regions are the dominant components in MIR wavelength range (see also Figure 1.4). The difference of the MIR SED shape between AGNs and non-AGNs can be clearly seen in the MIR color-color space. Lacy et al. (2004, 2007) propose a MIR color method to identify AGNs using four channel data (3.6, 4.5, 5.8, and 8.0 μm for ch1, ch2, ch3, and ch4, respectively) of the Infrared Array Camera (IRAC, Fazio et al., 2004) of the Spitzer Space Telescope. Lacy's MIR color diagnostics can be described as:

$$
\begin{aligned}
&[3.6] - [5.8] > -0.25 \\
&[4.5] - [8.0] > -0.5 \\
&[4.5] - [8.0] \leq 0.8\,([3.6] - [5.8]) + 1.25
\end{aligned}
$$

where [3.6], [4.5], [5.8], and [8.0] are the AB magnitude for ch1, ch2, ch3, and ch4 of the IRAC, respectively.

We first investigate whether our variability-selected AGN sample satisfies this MIR color criteria for AGNs or not. The top panels in Figure 3.11 show MIR color-color diagram for our variability-selected AGN samples (left panel: X-det sample, right panel: X-undet sample). Here we plot objects with statistically significant MIR detections (large circles; $S/N \geq 3$ magnitude limit for $3''$ aperture photometry; ch1: 25.5, ch2: 25.5, ch3: 23.0, ch4: 22.9 mag; Laigle et al., 2016). 413 out of 441 X-det sample and 32 out of 50 X-undet sample are plotted here. It is clear that more than half of our samples satisfy the Lacy's selection criteria, but a fraction of objects is located outside of the AGN wedge. 90 objects in the X-det sample (21.8%) and 14 objects in the X-undet sample (43.8%) do not satisfy the Lacy et al.'s criteria, which suggests that the X-undet sample is possibly more affected by the host galaxy flux than the X-det sample. In fact,

Figure 3.12 shows the MIR color-color diagram for X-det sample with color-bar of hard-band X-ray luminosity and suggests that low luminosity samples tend to be located outside the AGN wedge. To check the difference of luminosity between MIR color-selected sample and MIR color-unselected sample, we plot cumulative distributions of hard-band X-ray luminosity for each sample in Figure 3.13. We conduct the Kolmogorov–Smirnov test (KS test) and find that the luminosity distribution of MIR color-unselected sample is not the same distribution as that of MIR color-selected sample with a p-value of 8.8×10^{-5} %. Therefore we find that the X-undet samples have fainter hot/warm dust radiation than the X-det samples and tend to show similar MIR color to normal galaxies.

Stern et al. (2005) define another MIR color-color selection criterion to select AGNs, which are described as:

$$
\begin{aligned}
&[5.8] - [8.0] > -0.07 \\
&[3.6] - [4.5] > -0.2\,([5.8] - [8.0]) - 0.396 \\
&[3.6] - [4.5] > 2.5\,([5.8] - [8.0]) - 2.995.
\end{aligned}
$$

We plot this color diagnostics in the bottom panels of Figure 3.11. In this diagnostics, 101 objects in the X-det sample (24.5%) and 13 objects in the X-undet sample (40.6%) do not satisfy the Stern et al.'s criteria. A large amount of AGNs (especially low luminosity AGNs), which are not identified by MIR color diagnostics, can be identified by variability-based selection, suggesting that optical variability-based AGN selection is indeed a complementary tool to identify AGNs.

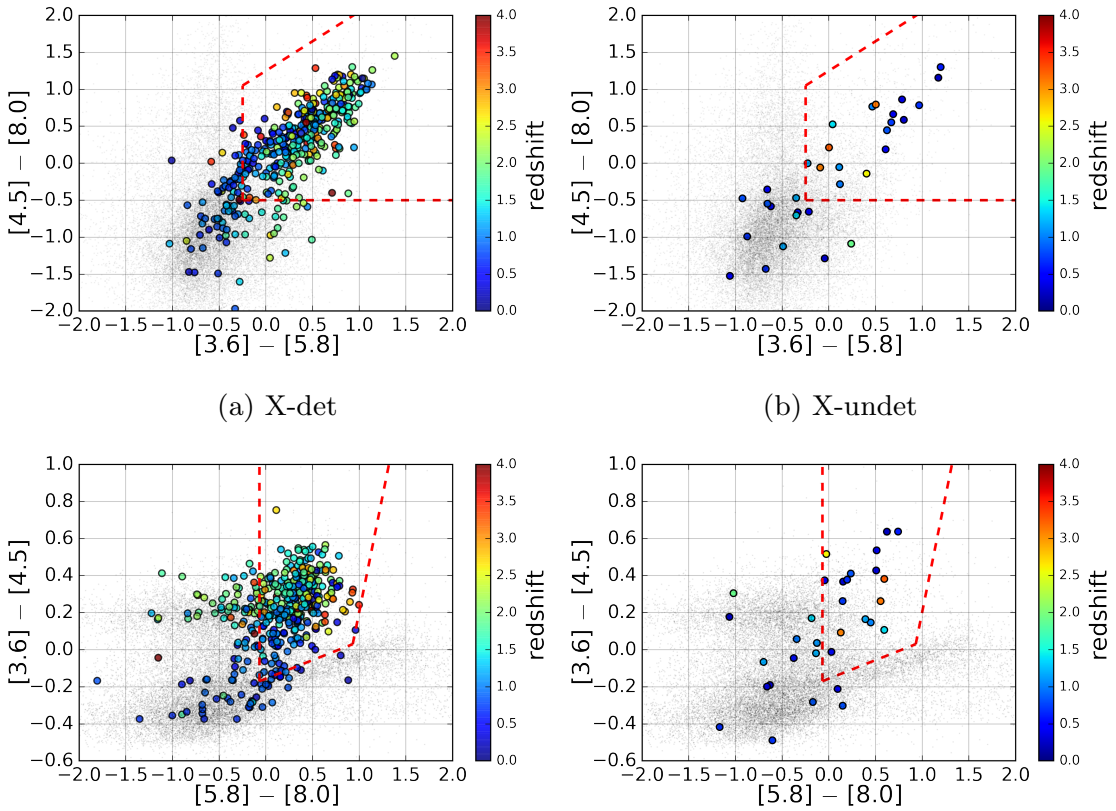

(a) X-det

(b) X-undet

(c) X-det

(d) X-undet

Fig 3.11: Mid-infrared color-color plots. The color-bars show redshift of samples. The red dashed lines are the AGN selection criteria from (top panels) Lacy et al. (2007) and (bottom panels) Stern et al. (2005) . The X-det (X-undet) samples are shown in the left (right) figures. The small gray dots are non-variable galaxies in the parent sample.

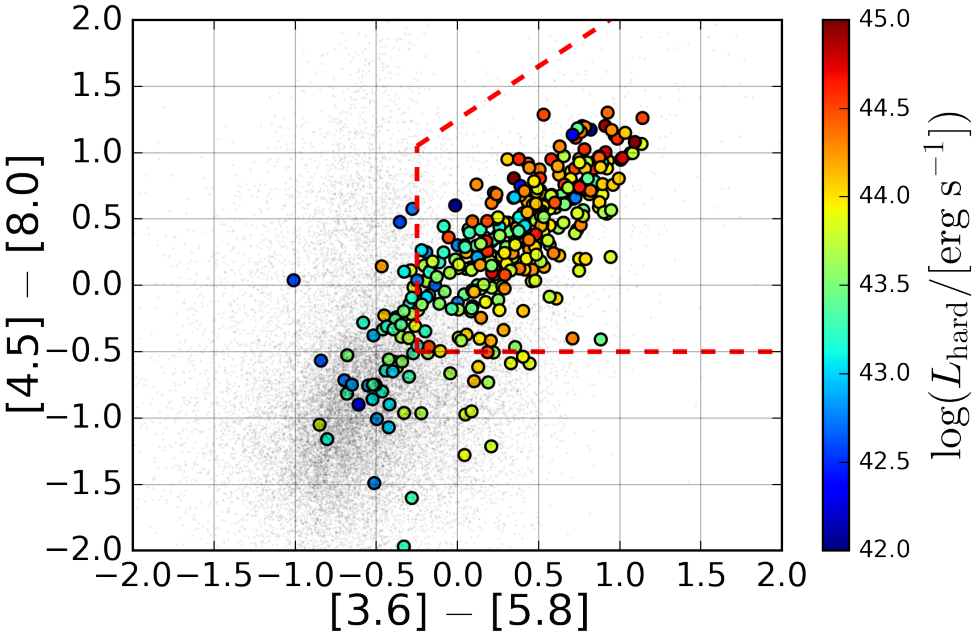

Fig 3.12: The same color-color plot as Figure 3.11 but the color-bar shows hard-band X-ray luminosity of samples.

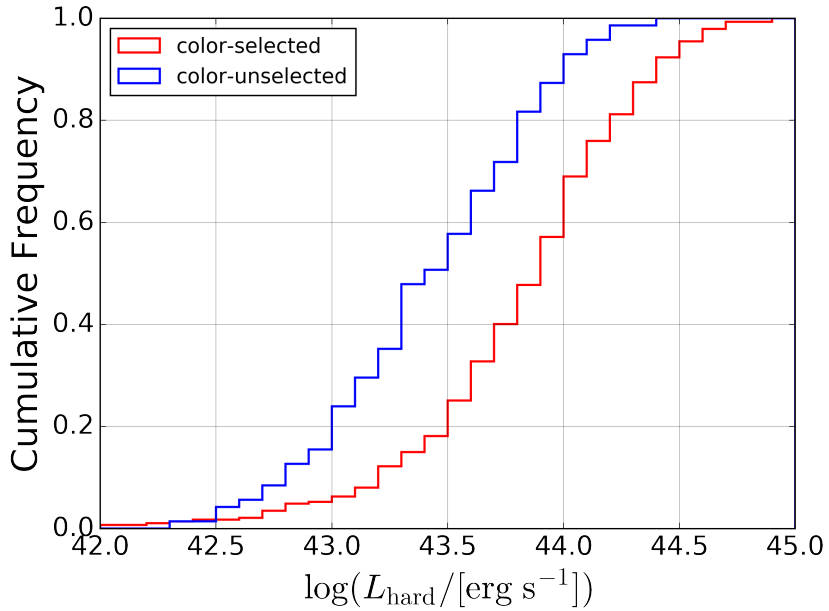

Fig 3.13: The cumulative hard-band luminosity distribution of MIR color-selected sample (red) and MIR color-unselected sample (blue).

4 Structure Function Analysis

Previous quasar studies show that the optical variability amplitude is correlated with the rest-frame wavelength and AGN luminosity, i.e., the variability amplitude is larger at shorter wavelength and lower luminosity (e.g., Vanden Berk et al., 2004). However it is unclear whether the wavelength- and luminosity-dependences of variability amplitude still holds or not for low luminosity AGNs ($L_{\rm bol} < 10^{45}$ erg s^{-1}, see Figure 1.7). In this section, we perform a structure function analysis to investigate the variability properties of our variability-selected AGNs.

Since the observational sampling of individual objects is limited, we study their ensemble structure functions, which represent typical variability amplitudes of the sample as a function of the rest-frame time-interval. We use 441 X-det sample in our variability-selected AGNs (see Section 3.1), which have redshift (72% of them have spectroscopic redshift and the other 28% have photometric redshift) and bolometric luminosity information. The overall rest-frame time-interval, rest-frame wavelength, and bolometric luminosity coverages of the X-det sample are shown in Figure 4.1. The median rest-frame wavelength and bolometric luminosity are 3165 Å and $10^{44.9}$ erg s^{-1}, respectively. The rest-frame time-interval Δt is calculated from the observed-frame time-interval $\Delta t_{\rm obs}$ and the redshift z with $\Delta t = \Delta t_{\rm obs}/(1+z)$, and the rest-frame wavelength λ is calculated from the effective wavelength of the HSC filters ($\lambda_{\rm eff}$ = 4816, 6264, 7740, and 9125Å for g, r, i, and z-band, respectively) and the redshift with $\lambda = \lambda_{\rm eff}/(1+z)$. Hereafter we refer rest-frame time-interval and rest-frame wavelength as simply 'time-interval' and 'wavelength', respectively, unless otherwise noted.

4.1 Ensemble Structure Function

The structure function (SF) is a useful tool to study the variability properties of AGNs (Vanden Berk et al., 2004; MacLeod et al., 2012; Kozłowski, 2016; Caplar et al., 2017). The SF represents the root-meen-square (RMS) of magnitude-difference of samples in a given time-interval Δt bin, i.e., typical variability amplitude at Δt, and can be written as:

$$SF_{\rm obs}(\Delta t) = \sqrt{\frac{1}{N}\sum_{N}[m(t_2) - m(t_1)]^2}, \tag{4.1.1}$$

where $m(t)$ is a magnitude at time t and N is the number of samples at time-interval Δt $(= t_2 - t_1)$ bin. To decrease the photometric noise and the contamination of host galaxy light (especially for extended sources), we here use magnitudes which are calculated by aperture photometry with the radius of PSF (i.e., aperture diameter is set to the FWHM of the PSF) after all PSFs are matched to the worst frame in each filter.

Practically, the SF can also be calculated from

$$SF_{\rm obs}(\Delta t) = 0.741 \times {\rm IQR}, \tag{4.1.2}$$

where IQR is the interquartile range between 25% and 75% of the sorted Δm distribution in each Δt bin and the coefficient 0.741 is the conversion factor from the IQR to the RMS when the Δm distribution is assumed to be a Gauss distribution. The equation (4.1.2) is useful since it is relatively insensitive to photometric outliers (MacLeod et al., 2012; Kozłowski, 2016), therefore we use equation (4.1.2) to calculate SF in our analysis. Since the SF calculated from the observed magnitude is affected by the deviation of photometric noise, we should evaluate the effect of photometric noise. To estimate the magnitude deviation caused by the photometric noise, we construct a control sample, which

is randomly selected from the *non-Var* sample with the same distributions of time-interval and magnitude as for the X-det sample, and calculate SF from this control sample in each Δt bin. Using the SF values calculated from the X-det sample and the control sample ($SF_{\rm obs}$ and $SF_{\rm noise}$, respectively), we calculate a net SF value ($SF_{\rm net}$) as follows (Kozłowski, 2016):

$$SF_{\rm net}(\Delta t) = \sqrt{SF^2_{\rm obs}(\Delta t) - SF^2_{\rm noise}(\Delta t)}. \tag{4.1.3}$$

The error bars of $SF_{\rm net}$, $SF_{\rm obs}$, and $SF_{\rm noise}$ are estimated by a bootstrap method as a following procedure: (i) We randomly select a sample (bootstrap sample) from the original sample with the same sample size to calculate $SF_{\rm obs}$. (ii) We also randomly select a control sample from the *non-Var* sample, which has the same distributions of magnitude and time-interval as for the bootstrap sample, to calculate $SF_{\rm noise}$. (iii) Using the $SF_{\rm obs}$ and $SF_{\rm noise}$, we calculate $SF_{\rm net}$ from equation (4.1.3). (iv) The processes from (i) to (iii) are conducted 1000 times, and we evaluate the scatter of the $SF_{\rm obs}$, $SF_{\rm noise}$, and $SF_{\rm net}$.

Figure 4.2 shows $SF_{\rm net}$, $SF_{\rm obs}$, and $SF_{\rm noise}$ in g-band data. It is found that $SF_{\rm noise}$ is negligible at large Δt but comparable with $SF_{\rm obs}$ at $\Delta t < 10$ days. Hereafter we refer net SF value as SF unless otherwise noted.

The SF as a function of Δt can reasonably be fitted with a power-law function,

$$SF(\Delta t) = SF_0 \left(\frac{\Delta t}{\Delta t_0} \right)^{b_t}, \tag{4.1.4}$$

where SF_0 is the value of SF at Δt_0 days time-interval and b_t is the slope of a power-law function. Here we set Δt_0 to be 100 days. In this fitting, we only use the $SF_{\rm net}$ data points between $\Delta t = 10$ days and 1 year. We also fit with a power-law function to the bootstrap re-sampling data to estimate the fitting uncertainties of the two free parameters. The best fitted results for each filter are shown in Figure 4.3 and summarized in Table 4.1. Figure 4.3 shows that the variability amplitude is larger for the shorter band filter although we do

Table 4.1: Best fitted results

filter	SF_0	b_t
g	0.210 ± 0.003	0.411 ± 0.013
r	0.160 ± 0.002	0.440 ± 0.012
i	0.133 ± 0.001	0.511 ± 0.010
z	0.097 ± 0.001	0.492 ± 0.013

not consider the luminosity-dependence on the AGN variability amplitude (see Section 4.2).

Another functional form is often assumed to explain the time-interval dependence of the AGN SF in the previous studies, following a prediction from the dumped random walk (DRW) model described as $SF(\Delta t) = SF_\infty[1 - \exp(-\Delta t/\tau)]^{1/2}$ (Kelly et al., 2009). The dumping time scale τ may be related to some physical parameters, such as black hole mass, and is typically an order of hundreds days (MacLeod et al., 2010, 2012). The DRW model predicts that the variability strength is constant ($SF = SF_\infty$) once the time-interval is larger than the dumping time scale. Figure 4.3 shows that the dumping time seems to be around 1 year for all the four filters, but this may be due to the insufficient data sampling at $\Delta t > 1$ yr. The SFs at longer timescale generally show unexpected breaks or wiggles due to the insufficient data sampling (Emmanoulopoulos et al., 2010). Although we cannot exclude the possibility that we are detecting true dumping signatures, we do not use the DRW model fitting in our analysis.

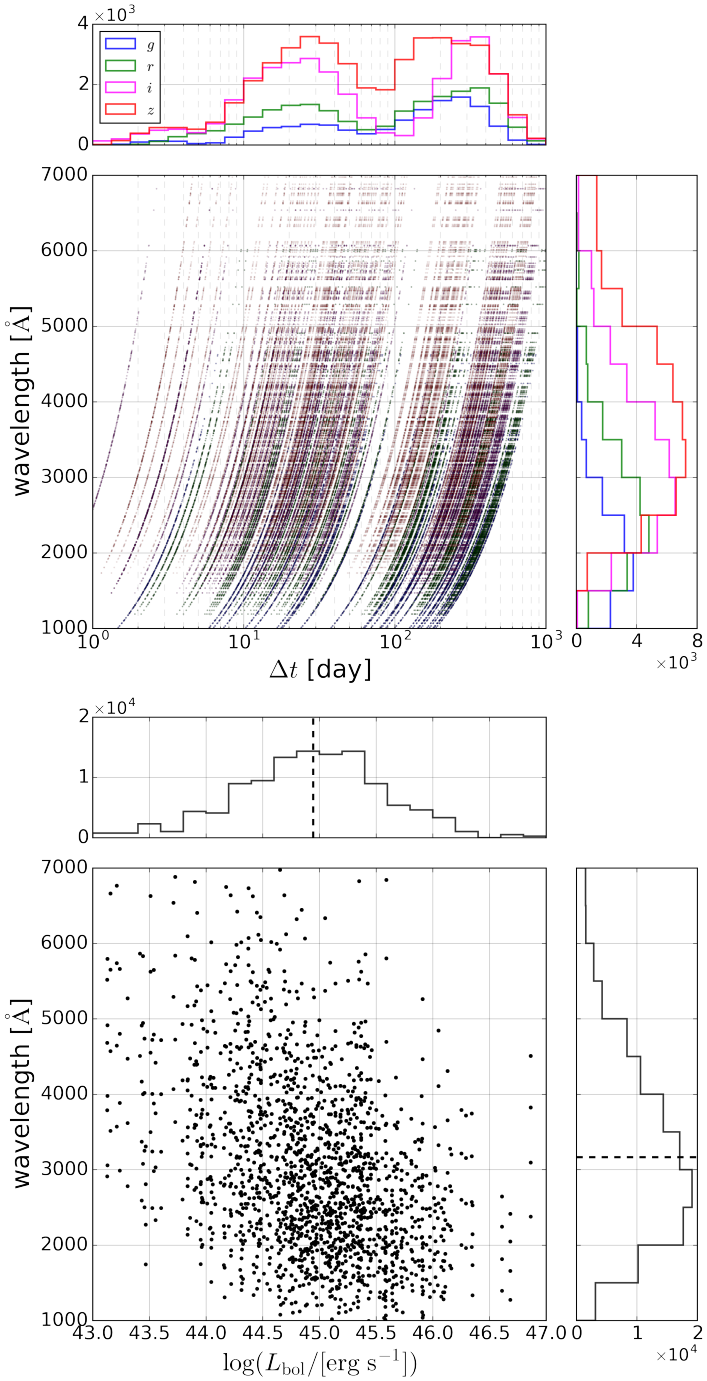

Fig 4.1: Observed data set for X-det sample in our variable AGNs are plotted in time-interval and wavelength space (top), and wavelength and AGN bolometric luminosity space (bottom). The distributions of the X-det sample in each parameter are shown as a histogram in each side of panels. The blue, green, magenta, and red-colored histograms in the top panel correspond to the data observed with g, r, i, z-band filter, respectively. The dashed lines in each histogram are the median values for all the data set in X-det sample.

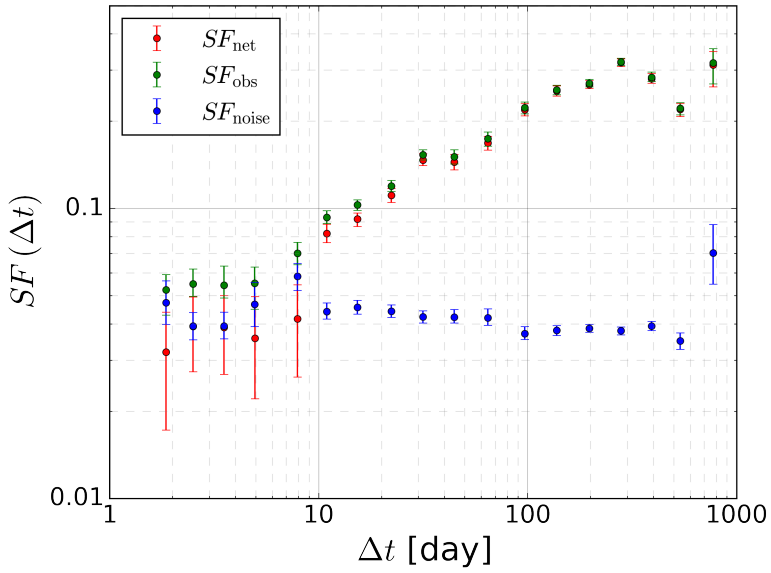

Fig 4.2: The structure function for X-det sample in g-band data. The $SF_{\rm net}$, $SF_{\rm obs}$, and $SF_{\rm noise}$ are plotted with red, green, and blue points, respectively.

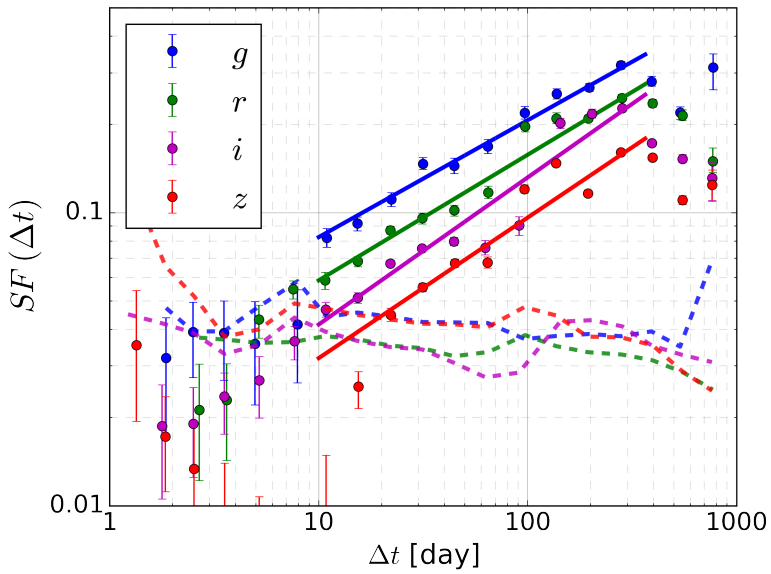

Fig 4.3: $SF_{\rm net}$ as a function of Δt for the X-det sample in g (blue), r (green), i (magenta), and z (red) band data, respectively. The solid lines are the results of best fitting with a model function and the dashed lines are $SF_{\rm noise}$ for each filter.

4.2 Dependences on Physical Parameters

In the previous quasar studies, it has been argued that the variability amplitude of AGNs mainly depends on the time-interval, wavelength, and AGN luminosity. If we make a tentative assumption that the correlation of variability amplitude with time-interval is independent of that with wavelength and with luminosity, we can write the SF described in equation (4.1.4) as the following form:

$$SF(\Delta t, \lambda, L_{\rm bol}) = SF_0(\lambda, L_{\rm bol}) \left(\frac{\Delta t}{\Delta t_0} \right)^{b_t}, \tag{4.2.1}$$

where λ is wavelength and $L_{\rm bol}$ is AGN bolometric luminosity. As the SF has a unit of magnitude, it is natural to express the SF_0 as following form:

$$SF_0(\lambda, L_{\rm bol}) = -2.5 \log V_0(\lambda, L_{\rm bol}) \tag{4.2.2}$$

$$V_0(\lambda, L_{\rm bol}) \propto V_1(\lambda)\ V_2(L_{\rm bol}), \tag{4.2.3}$$

where $V_1(\lambda)$ and $V_2(L_{\rm bol})$ denote the dependencies of SF on the wavelength and luminosity, respectively. It is noted that the SF_0 is the variability amplitude at time-interval Δt_0 and we set Δt_0 as 100 days.

To evaluate the dependences of SF on the wavelength and luminosity, namely the functions represented by $V_1(\lambda)$ and $V_2(L_{\rm bol})$, we divide the X-det sample into several luminosity- and wavelength-bins as follows; (i) luminosity bins of $\log(L_{\rm bol}/[\mathrm{erg\ s^{-1}}])$ = 44.0-44.5, 44.5-45.0, 45.0-45.5, 45.5-46.0, and (ii) wavelength bins of λ = 1500-2000, 2000-2500, 2500-3000, 3000-4000, 4000-5000Å. We further divide the sample in each bin into the sub-samples by the other quantity (i.e., wavelength for (i) and luminosity for (ii); see Figure 4.4). We then calculate the SF in the same manner as described in the previous subsection and obtain the variability amplitude at Δt = 100 days (i.e., SF_0) by a power-law

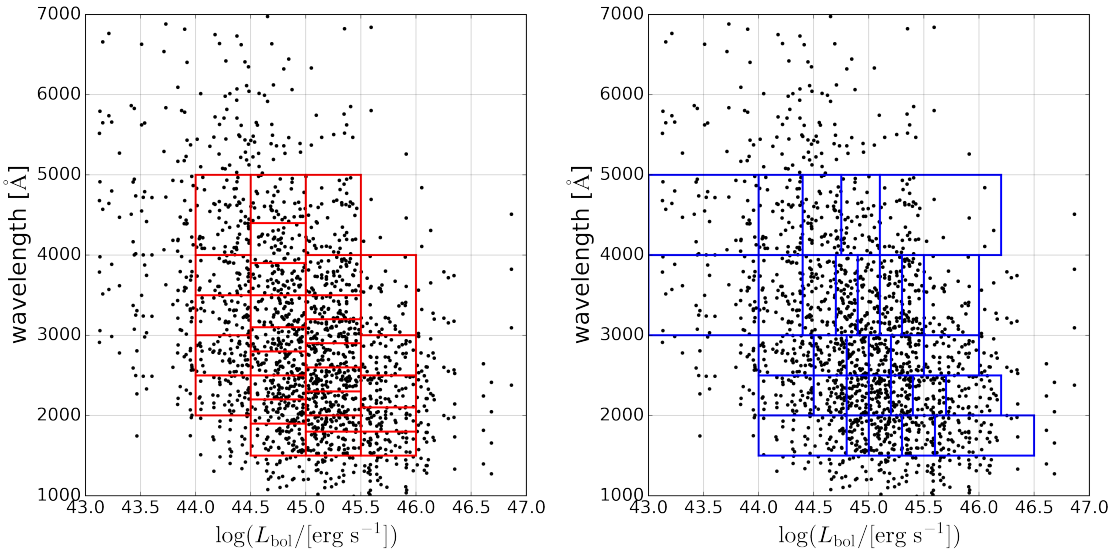

Fig 4.4: The same parameter space as the bottom panel in Figure 4.1. (Left) The red lines show the boundaries of sub-samples in each luminosity-bin. (Right) The blue lines show the boundaries of sub-samples in each wavelength-bin.

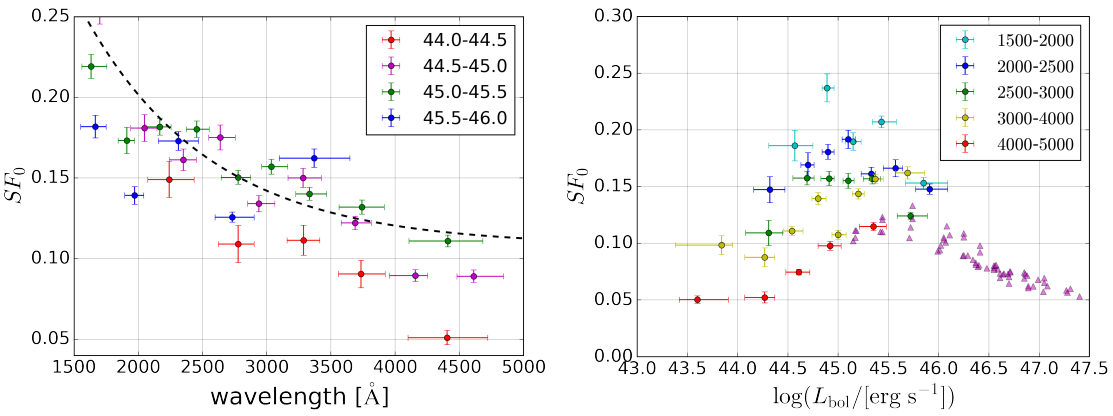

(a) wavelength-dependence (b) luminosity-dependence

Fig 4.5: SF_0 as a function of (a) wavelength and (b) luminosity. The dashed line in the left panel is the wavelength-dependence of the SDSS quasars (Vanden Berk et al., 2004). The magenta triangles in the right panel show the results of the SDSS quasars (Caplar et al., 2017).

(equation 4.1.4) fitting. Figure 4.5 shows the result of each sub-sample; the left panel shows the wavelength-dependence for each luminosity bin and the right panel shows luminosity-dependence for each wavelength bin. In the left panel of Figure 4.5, an empirical relationship between the variability amplitude and wavelength for SDSS quasars (equation (11) of Vanden Berk et al., 2004) is compared with our results. It is clear that the variability amplitudes of the X-det sample show similar wavelength-dependences to that of the SDSS quasars; the larger variability amplitude is observed at shorter wavelength. On the other hand, we find complex luminosity-dependences of the variability amplitude especially at $L_{\rm bol} \lesssim 10^{45}$ erg s^{-1}, while previous studies for the SDSS quasars ($L_{\rm bol} > 10^{45}$ erg s^{-1}) show a monotonic increase of the variability amplitude with decreasing AGN luminosity ($\propto L_{\rm bol}^{-0.5}$; e.g., Caplar et al., 2017). The luminosity-dependence of the variability amplitude is clearer in the longer wavelength samples; the variability amplitude is smaller in the lower luminosity AGNs. This trend can also be seen in the low luminosity samples of Caplar et al. (2017) (Figure 4.5), which is based on the SDSS quasars ($L_{\rm bol} > 10^{45}$ erg s^{-1}) with r-band data-set obtained by the Palomar Transient Factory and intermediate Palomar Transient Factory (PTF/iPTF) surveys.

This complex luminosity-dependence can naturally be explained by larger contamination of the host galaxy light to the lower luminosity AGNs. In fact, Shen et al. (2011) suggests that the contribution of host galaxy light to the UV-optical spectra of quasars becomes more significant in the lower luminosity AGNs ($L_{\rm bol} \lesssim 10^{46}$ erg s^{-1}). Since the AGN accretion disk emission is generally bluer than the host galaxy stellar emission at UV-optical wavelength, the contribution of host galaxy light is larger in the longer wavelength, therefore the decrement of variability amplitude is larger in the longer wavelength. The effect of the host galaxy light in SF analysis is discussed in Section 5.1 in detail.

To understand the 'intrinsic' AGN variability properties eliminating the contamination from the host galaxy light, we use the luminous and short-wavelength samples where the host galaxy flux contribution can be negligible. We examine the intrinsic AGN dependencies of variability amplitude on wavelength and luminosity with the following procedure: (i) We use the sub-samples in the lu-

minosity bins of $\log(L_{\rm bol}/[{\rm erg\ s^{-1}}]) = 45.0$-$45.5$ and 45.5-46.0 to estimate the wavelength-dependence of the variability amplitude SF_0. In this step, we ignore the luminosity-dependence between the two luminosity bins. (ii) We estimate the luminosity-dependence for the sub-samples in the wavelength bins of $\lambda = 1500$-2000, 2000-2500, and 2500-3000Å, after correcting the wavelength-dependence of SF_0. (iii) We re-evaluate the wavelength-dependence of SF_0 after correcting the luminosity-dependence of SF_0 estimated by the step (ii). (iv) We iterate the steps (ii) and (iii) 10 times.

We here use a power-law function to fit the dependences of SF_0 on wavelength and luminosity. In the step (i), since we ignore the luminosity-dependence between the two luminosity bins, the SF_0 depends on only wavelength and can be written as:

$$SF_0(\lambda) = -2.5 \log\left[a_\lambda V_1(\lambda)\right],\ V_1(\lambda) = \left(\frac{\lambda}{\lambda_0}\right)^{b_\lambda}, \tag{4.2.4}$$

where a_λ is a normalization factor at the wavelength λ_0 and b_λ is a slope of the power-law function $V_1(\lambda)$. We set λ_0 to be 3000Å. To correct the wavelength-dependence of $SF_0(\lambda, L_{\rm bol})$ in the step (ii), the following factor,

$$C_1(\lambda) = \frac{SF_0(\lambda_0)}{SF_0(\lambda)} = \frac{\log(a_\lambda)}{\log\left[a_\lambda V_1(\lambda)\right]}, \tag{4.2.5}$$

should be applied to the $SF_0(\lambda, L_{\rm bol})$ in each sub-sample. For simplicity, we use the median wavelength in each sub-sample to calculate the correction factor $C_1(\lambda)$. After the SF_0 is normalized at λ_0, the SF_0 depends on only luminosity and can be written as:

$$SF_0(L_{\rm bol}) = -2.5 \log\left[a_L V_2(L_{\rm bol})\right],\ V_2(L_{\rm bol}) = \left(\frac{L_{\rm bol}}{L_0}\right)^{b_L}, \tag{4.2.6}$$

where a_L is a normalization factor at the L_0 (we set L_0 to be 10^{45} erg s^{-1}) and b_L is a slope of the power-law function $V_2(L_{\rm bol})$. The correction of the luminosity-dependence can be written as:

$$C_2(L_{\rm bol}) = \frac{SF(L_0)}{SF(L_{\rm bol})} = \frac{\log(a_L)}{\log\left[a_L V_2(L_{\rm bol})\right]}, \tag{4.2.7}$$

and this correction factor is applied to the $SF_0(\lambda, L_{\rm bol})$ in each sub-sample to correct the luminosity-dependence of $SF_0(\lambda, L_{\rm bol})$ in the step (iii). To calculate the correction factor $C_2(L_{\rm bol})$, we use the median bolometric luminosity in each sub-sample.

The obtained wavelength and luminosity dependences after the iterations in the step (iv) are shown in the top-left and the top-right panels of Figure 4.6, respectively, and the best fitted parameters are summarized in Table 4.2. The wavelength dependence is almost consistent with the previous work for the SDSS quasars (Vanden Berk et al., 2004), and the luminosity dependence is consistent with the Caplar et al. (2017)'s result down to $L_{\rm bol} \sim 10^{45}$ erg s^{-1}, but the decrement of variability amplitude at the lower luminosity range still remains.

Using the dependences of SF_0 on wavelength and luminosity, we finally investigate the intrinsic (i.e., wavelength and luminosity-independent) dependence of SF on time-interval Δt. Using the functions $V_1(\lambda)$ and $V_2(L_{\rm bol})$, SF can be expressed as

$$SF(\Delta t, \lambda, L_{\rm bol}) = \left[-2.5\log\left(kV_1(\lambda)V_2(L_{\rm bol})\right)\right]\left(\frac{\Delta t}{\Delta t_0}\right)^{b_t}, \tag{4.2.8}$$

where k is a normalization factor, which is calculated by the following equation:

$$SF(\Delta t_0, \lambda_0, L_0) = SF_0(\lambda_0, L_0) = -2.5\log(k). \tag{4.2.9}$$

Here we assume the variability amplitude at $\Delta t_0 = 100$ days, $\lambda_0 = 3000$ Å, and

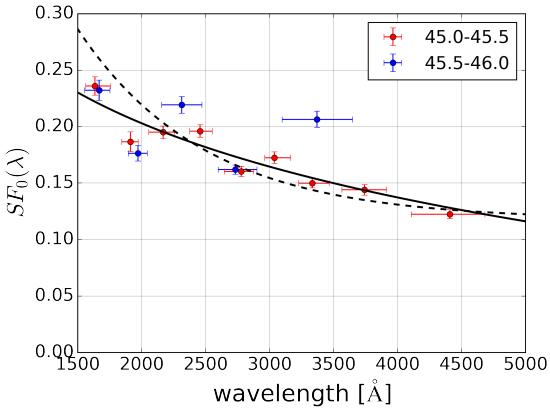

(a) wavelength dependence

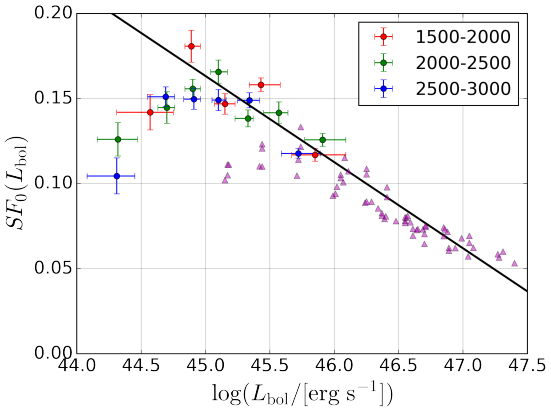

(b) luminosity dependence

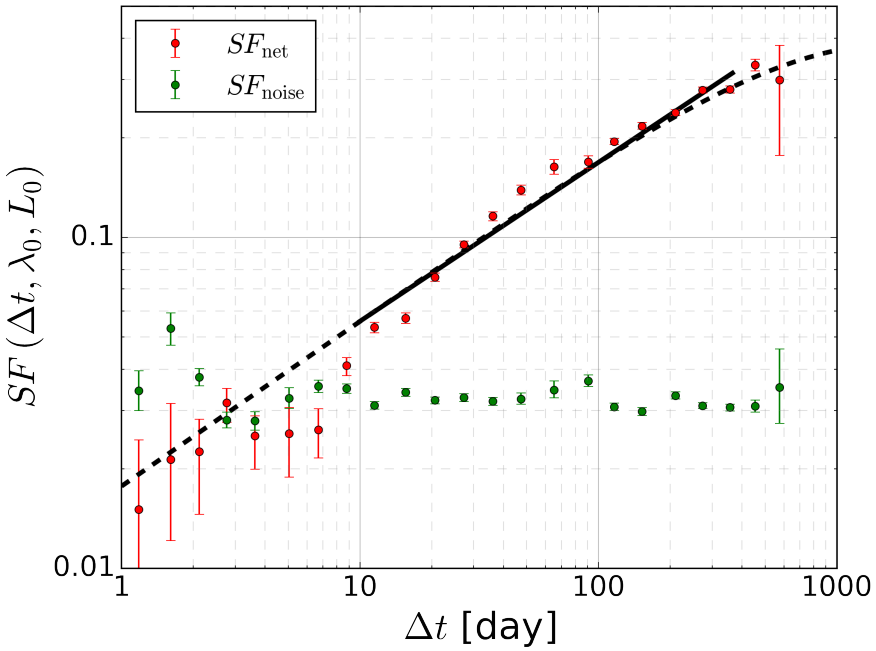

(c) time-interval dependence

Fig 4.6: The dependences of SF_0 on (a) wavelength, (b) luminosity, and (c) time-interval. The SF_0 is normalized at (a) $L_0 = 10^{45}$ erg s^{-1}, (b) $\lambda_0 = 3000$Å, and (c) L_0, λ_0. The dashed line in the panel (a) and the magenta triangles in the panel (b) are the same as Figure 4.5. The dashed line in the panel (c) is the DRW model prediction that is the case of $\tau = 500$ days and scaled at $\Delta t = 100$ days. The solid line in each panel show the best fitted result with a model function (described in the text).

$L_0 = 10^{45}$ erg s^{-1} is $-2.5\log(0.86) \sim 0.164$, which is close to the normalizations a_λ and a_L (see Figure 4.6 and Table 4.2). The correction factor for normalizing the wavelength- and luminosity-dependences is calculated from

$$C_0(\lambda, L_{\rm bol}) = \frac{SF(\Delta t, \lambda_0, L_0)}{SF(\Delta t, \lambda, L_{\rm bol})} = \frac{\log(k)}{\log\left[kV_1(\lambda)V_2(L_{\rm bol})\right]}. \qquad (4.2.10)$$

$C_0(\lambda, L_{\rm bol})$ is applied to the magnitude difference Δm for individual objects to construct the SF normalized at λ_0 and L_0. From equation (4.1.3), the same correction is also applied to the magnitude difference of the randomly selected *non-Var* samples to calculate $SF_{\rm noise}$. To construct the sample which is little affected by the host galaxy contamination, we use the the X-det sample with $\lambda \leq 3500$ Å and $L_{\rm bol} \geq 10^{45}$ erg s^{-1} and calculate the normalized SF. We then fit the normalized SF with a power-law function described in equation (4.2.1). The result is shown in the bottom panel of Figure 4.6 and the best fitted parameters are summarized in Table 4.2. We also plot a SF of the DRW model with $\tau = 500$ days (scaled to match the observed data at $\Delta t = 100$ days). As mentioned above, the SF of the DRW model has a functional form of $[1 - \exp(-\Delta t/\tau)]^{1/2}$, thus at the shorter time-interval ($\Delta t \ll \tau$), the SF is asymptotically power-law with the slope of 0.5. Our result of the power-law slope of the Δt dependence, 0.487 ± 0.007, is consistent with the value expected in the DRW model, which may indicate that the AGN variability is caused by stochastic processes, such as thermal fluctuations of the accretion disk (Dexter & Agol, 2011). It is noted that the SF in the bottom panel of Figure 4.6 seems to show the dumping feature being consistent with the DRW model with $\tau = 500$ days, but this can be due to the insufficient light curve sampling at the long interval, as mentioned before (see also Figure 4.1).

Table 4.2: Best fitted parameters

dependence	fitting function	normalization	slope
wavelength	equation (4.2.4)	$a_\lambda = 0.859 \pm 0.001$	$b_\lambda = 0.0872 \pm 0.0050$
luminosity	equation (4.2.6)	$a_L = 0.860 \pm 0.003$	$b_L = 0.0202 \pm 0.0021$
time-interval	equation (4.2.1)	$SF_0 = 0.170 \pm 0.001$	$b_t = 0.487 \pm 0.007$

5 Discussion

5.1 Host Galaxy Contamination

5.1.1 Host Galaxy to AGN Flux Ratio

The SF analysis shows that the host galaxy light affects the SF at low luminosity AGNs ($L_{\rm bol} \lesssim 10^{45}$ erg s^{-1}); the observed variability amplitude in the unit of magnitude decreases as the relative contribution of the host galaxy lights increases. To understand the effect of the host galaxy light, we add the host galaxy component to the SF analysis.

As we mentioned in Section 4, the SF represents the typical magnitude-difference at a given time-interval Δt, thus the SF, including host galaxy contribution, can be written as the following flux ratio:

$$SF_{\rm total}(\Delta t) = -2.5 \log \left(\frac{f_{\rm AGN}(t_2) + f_{\rm host}}{f_{\rm AGN}(t_1) + f_{\rm host}} \right), \quad \Delta t \equiv t_2 - t_1, \tag{5.1.1}$$

where $f_{\rm AGN}(t)$ is the AGN flux at the time t, and $f_{\rm host}$ is the host galaxy flux (assuming the stable value).

If the total flux is dominated in the AGN flux ($f_{\rm AGN} \gg f_{\rm host}$), the SF, i.e., the intrinsic AGN SF, can be written as:

$$SF_{\rm AGN}(\Delta t) = -2.5 \log \left(\frac{f_{\rm AGN}(t_2)}{f_{\rm AGN}(t_1)} \right). \tag{5.1.2}$$

Now we introduce the host galaxy to AGN flux ratio as:

$$r \equiv \frac{f_{\rm host}}{\langle f_{\rm AGN}(t) \rangle}, \tag{5.1.3}$$

where $\langle f_{\rm AGN}(t)\rangle$ is the time-averaged AGN flux. We here assume that $\langle f_{\rm AGN}(t)\rangle$ is the arithmetic mean; $\langle f_{\rm AGN}(t)\rangle = (f_{\rm AGN}(t_1) + f_{\rm AGN}(t_2))/2$. Using equations (5.1.2) and (5.1.3), equation (5.1.1) can be approximated as:

$$SF_{\rm total}(\Delta t) \sim -2.5 \log \left(\frac{10^{-0.4 SF_{\rm AGN}(\Delta t)} + r}{1+r} \right). \tag{5.1.4}$$

Thus, the host galaxy to AGN flux ratio r can be estimated from the intrinsic AGN SF ($SF_{\rm AGN}$) and the total SF ($SF_{\rm total}$) as

$$r \sim \frac{10^{-0.4 SF_{\rm total}(\Delta t)} - 10^{-0.4 SF_{\rm AGN}(\Delta t)}}{1 - 10^{-0.4 SF_{\rm total}(\Delta t)}}. \tag{5.1.5}$$

We here consider $\Delta t = 100$ days, which means that the SF can be calculated from the SF_0 and the intrinsic AGN SF can be estimated from the luminosity-dependence of SF_0 as shown in Section 4.2. We assume that the intrinsic AGN luminosity-dependence (i.e., equation (4.2.6), the solid line in the top-right panel of Figure 4.6), can be extrapolated down to the low luminosity ($L_{\rm bol} < 10^{45}$ erg s^{-1}), which is suggested from the previous studies. Gallastegui-Aizpun & Sarajedini (2014) decompose the AGN/host spectra for 5342 AGN sample at $z \lesssim 0.84$ taken from the SDSS-DR7 by using eigenspectra fitting and investigate the luminosity-dependence of SF in g, r, and i-band data-set, respectively. Their result shows that the luminosity-dependence still continues down to the AGN bolometric luminosity of $\sim 10^{43.5}$ erg s^{-1} in all the filters. Heinis et al. (2016) also perform AGN/host decomposition through SED fitting for 975 variability-selected AGNs at $z < 1$ from the PS1 survey and show that the maximum differential-flux of the AGN light curves are anti-correlated with the AGN bolometric luminosity and this anti-correlation continues to hold down to the AGN bolometric luminosity of $\sim 10^{43.5}$ erg s^{-1}.

We use the SF_0 for the sub-samples in the five wavelength bins of 1500-2000, 2000-2500, 2500-3000, 3000-4000, and 4000-5000Å, as the $SF_{\rm total}$. We then cal-

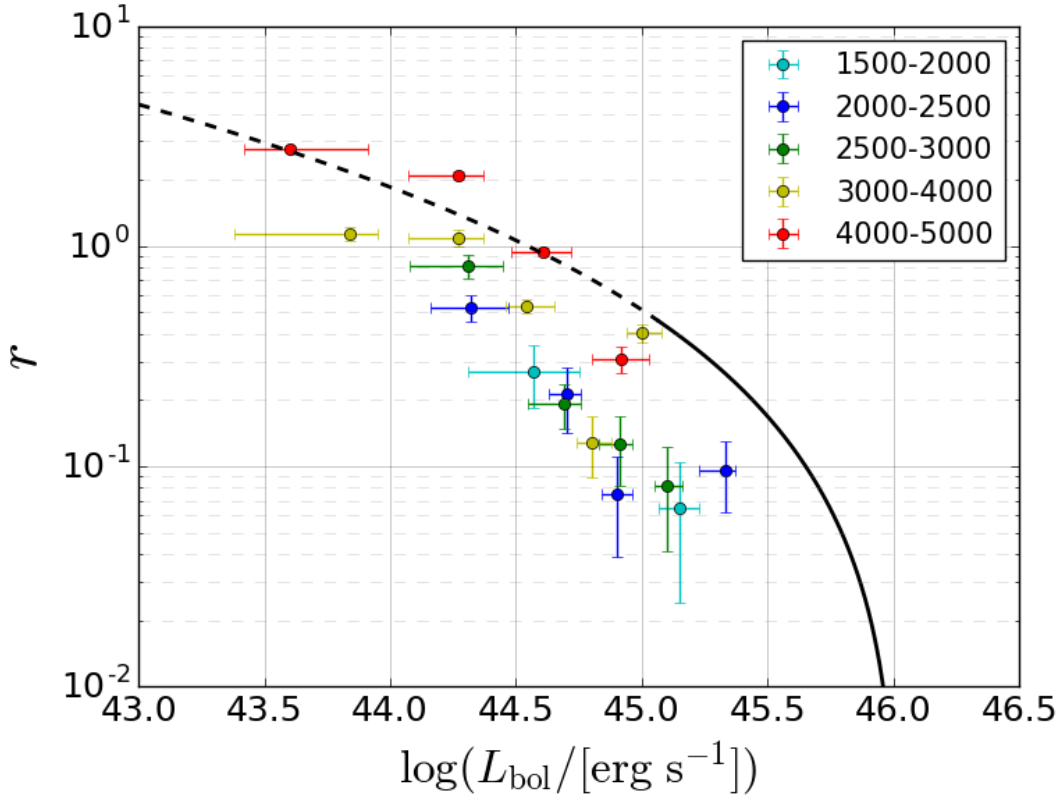

Fig 5.1: Host galaxy to AGN flux ratio for each sub-samples in wavelength-bins of 1500-2000 (cyan), 2000-2500 (blue), 2500-3000 (green), 3000-4000 (yellow), and 4000-5000Å (red). The black solid line is the host galaxy to AGN flux ratio at 5100Å for the SDSS quasars (Shen et al., 2011) and the line is extrapolated down to low luminosity as shown in the black dashed line.

culate the host galaxy to AGN flux ratio r from equation (5.1.5).

The host galaxy to AGN flux r as a function of the AGN bolometric luminosity for each wavelength-bin is shown in Figure 5.1. Figure 5.1 shows that the host galaxy to AGN flux ratio has anti-correlation with the AGN luminosity and the fraction has higher at the longer wavelengths. This luminosity-dependence of the host galaxy to AGN flux ratio is similar trend to that of Shen et al. (2011), who provide an empirical relationship between the host galaxy to AGN flux ratio at 5100Å and the total (AGN+host galaxy) monochromatic luminosity at 5100Å ($L^{\rm total}_{5100\text{Å}}$) for the SDSS quasars with luminosities of $L_{\rm bol} > 10^{45}$ erg s^{-1} (the black solid line in Figure 5.1), expressed as:

$$r_{5100\text{Å}} = 0.8052 - 1.5502x + 0.9121x^2 - 0.1577x^3, \tag{5.1.6}$$

where $x + 44 \equiv \log(L^{\rm total}_{5100\text{Å}}/[\text{erg s}^{-1}]) < 45.053$, and the contribution of the host galaxy light can be ignored at at $x + 44 > 45.053$ (see equation (1) in Shen et al. (2011)).

The approximation described in equation (5.1.5) is mathematically not clear, therefore we need to check whether the approximation is valid or not. We first use the host galaxy to AGN flux ratio r of the sub-samples in each wavelength-bin to calculate the host galaxy flux as:

$$f_{\rm host} = \langle\ f_{\rm total}(t)\ \rangle \times \frac{r}{1+r}, \tag{5.1.7}$$

where $\langle f_{\rm total}(t)\rangle$ is the time-averaged total flux (i.e., aperture flux) of individual objects in each sub-sample. Then we subtract the host galaxy flux from the total flux to calculate the AGN flux in each epoch. Using the AGN flux, we re-construct the luminosity-dependence of the SF_0 in the same procedure as described in Section 4.2 to check whether we can reproduce the intrinsic AGN dependence, i.e., equation (4.2.6) for the low luminosity sub-samples.

Figure 5.2 shows the luminosity-dependence of the SF_0 after subtraction of the host galaxy flux. It is clear that the $SF_{\rm AGN}$ in low luminosity sub-samples can be recovered by the SF_0 after subtraction of the host galaxy flux. This suggests that the approximation of equation (4.2.6) is reasonable, in other words, we can estimate the typical host galaxy to AGN flux ratio from the SF analysis.

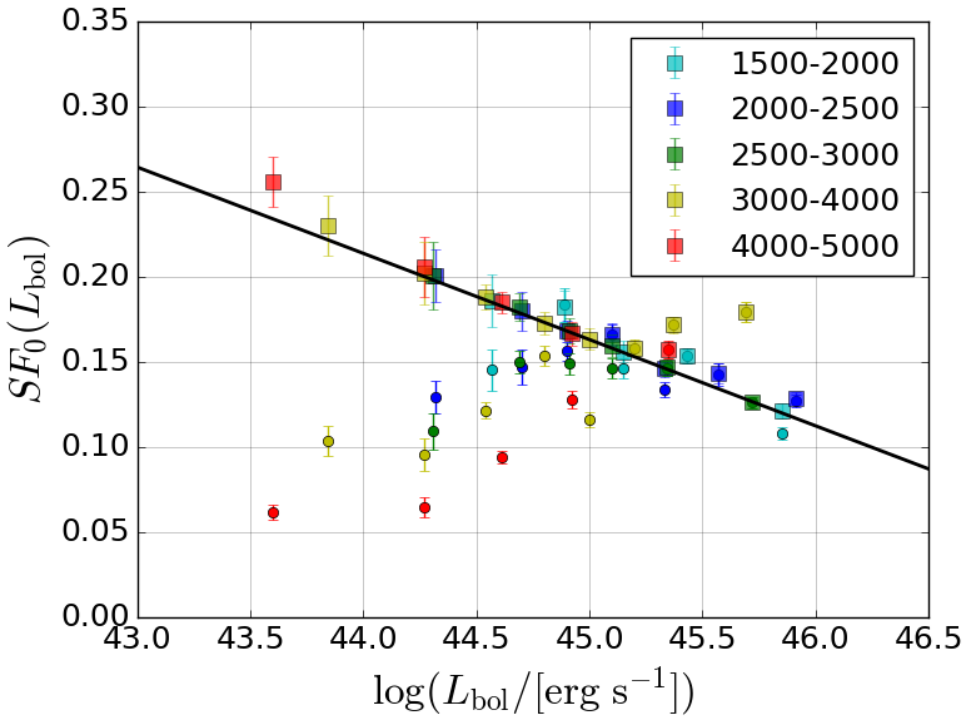

Fig 5.2: Variability amplitude as a function of the AGN bolometric luminosity. The color circles are the total SF ($SF_{\rm total}$) of the sub-samples in each wavelength-bin (normalized at 3000Å). The square points are the SF_0 of the sub-samples in each wavelength-bin after subtraction of the host galaxy flux. The solid line is the best fitted line of luminosity dependence, which is the same line as the bottom panel in Figure 4.6. It is clear that the variability amplitude after subtraction of host galaxy flux can reproduce the intrinsic AGN SF (i.e., $SF_{\rm AGN}$).

5.1.2 Constraints on the AGN Host Galaxy Type

The host galaxy to AGN flux ratio depends on not only the AGN luminosity but also wavelength (Figure 5.1), in other words, the wavelength dependence of the flux ratio of host galaxy to AGN reflects the stellar populations of the host galaxy. To constrain the types of host galaxies in our variability-selected AGNs, we construct the composite (AGN+host galaxy) SEDs to calculate the host galaxy to AGN flux ratios and compare them with our results obtained in Section 5.1.1.

To construct the composite spectra with type-I quasar and different types of galaxy SEDs, we use $QSO1$ (type-I QSO) for the quasar SED template and $Ell13$ (13 Gyr old elliptical galaxy), $S0$ (spiral-0 type galaxy), Sdm (spiral-dm type galaxy), and $M82$ (starburst galaxy) for the host galaxy SED model templates, which are presented in Polletta et al. (2007). The model SED templates are shown in Figure 5.3. We then assume the host galaxy to AGN flux ratio at 5100 Å as a function of luminosity, presented in Shen et al. (2011) (equation (5.1.6)). The bolometric correction factor for the 5100 Å monochromatic luminosity is assumed to be 9.26 (Shen et al., 2011). Under these assumptions, we construct luminosity-dependent AGN+host galaxy composite SEDs, shown in Figure 5.4), and calculate the host galaxy to AGN flux ratio in each wavelength bin ($[\lambda_1, \lambda_2]$ = [1500Å, 2000Å], [2000Å, 2500Å], [2500Å, 3000Å], [3000Å, 4000Å], and [4000Å, 5000Å]) from,

$$r = \frac{\int_{\lambda_1}^{\lambda_2} f_{\rm host}(\lambda) d\lambda}{\int_{\lambda_1}^{\lambda_2} f_{\rm AGN}(\lambda) d\lambda}, \tag{5.1.8}$$

where $f_{\rm host}$ and $f_{\rm AGN}$ are the flux values of model templates for host galaxy and AGN, respectively.

Figure 5.5 shows the results from the SF analysis described in Section 5.1.1 and the results from the SED model templates in each wavelength bin. The median

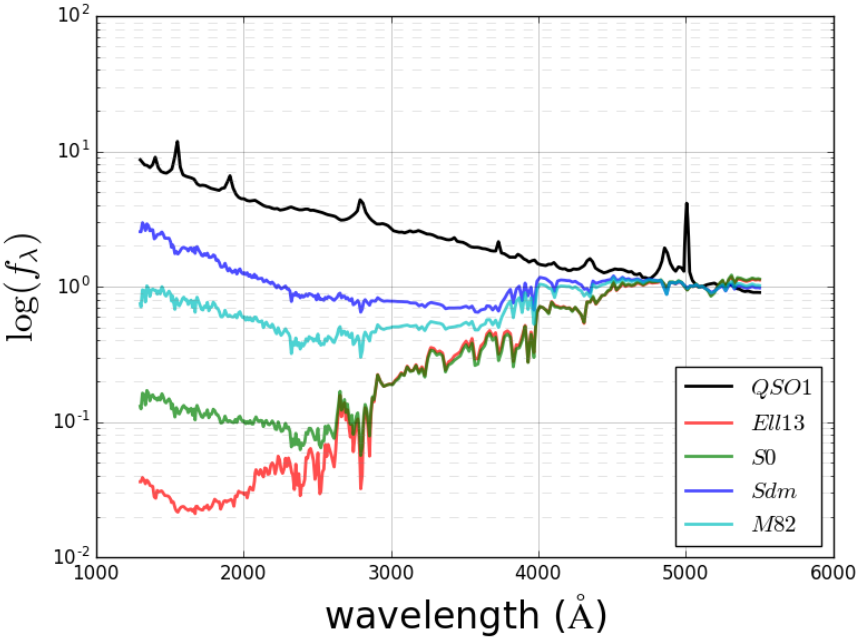

Fig 5.3: SED model templates of type-I quasar ($QSO1$) and host galaxies ($Ell13$, $S0$, Sdm, $M82$), all of which are normalized at 5100 Å.

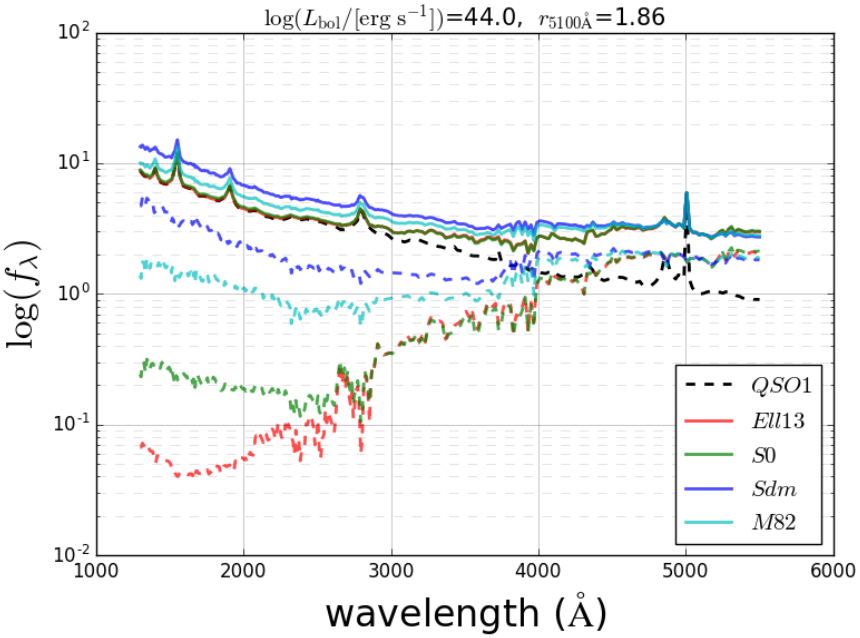

Fig 5.4: Composite SEDs (solid lines) which are assumed to be the host galaxy to AGN flux ratio at 5100 Å with $L_{\rm bol} = 10^{44}$ erg s^{-1} (Shen et al., 2011). The dashed lines are model SED templates of AGN and host galaxies.

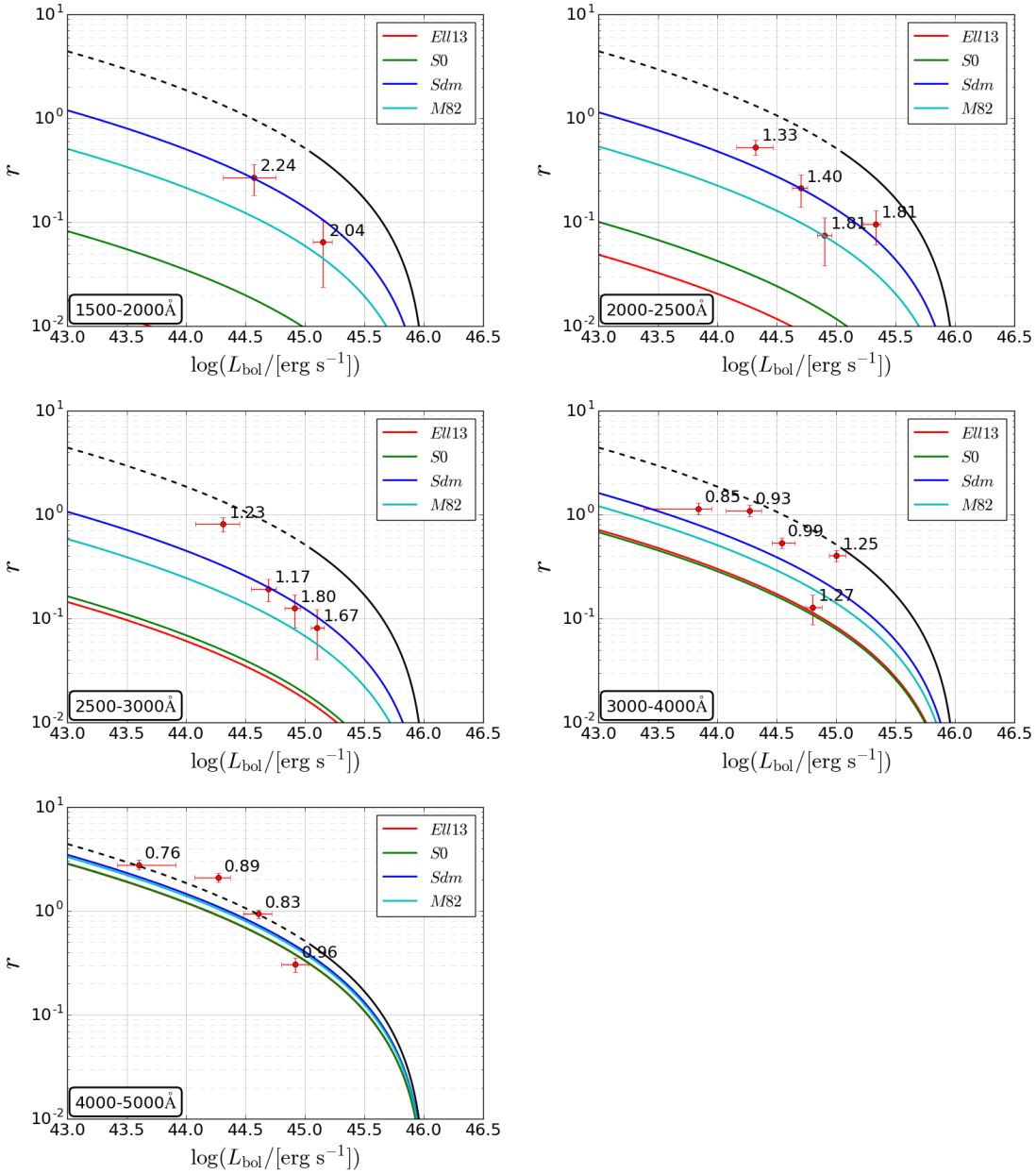

Fig 5.5: Host galaxy to AGN flux ratio as a function of the AGN bolometric luminosity. The red points in each panel are the results of sub-samples in each wavelength-bin calculated from equation (5.1.5) (top-left: 1500-2000Å, top-right: 2000-2500Å, middle-left: 2500-3000Å, middle-right: 3000-4000Å, bottom-left: 4000-5000Å). The black solid curve is the host galaxy to AGN flux ratio at 5100Å for the SDSS quasars (Shen et al., 2011) and the fraction is extrapolated to low luminosity (dashed curve) (equation (5.1.6)). The colored-curves are calculated from composite spectra assuming the host galaxy to AGN flux ratio at 5100Å and the host galaxy type (red: *Ell*13, green: *S*0, blue: *Sdm*, cyan: *M*82). The median redshift of a sub-sample is shown at near each data point.

redshifts in each subclasses are also shown near the data points in Figure 5.5. It is clearly seen in Figure 5.5 that in shorter wavelength bins ($\leq$ 3000Å), the host galaxy to AGN flux ratios of young stellar systems, like Sdm and $M82$, are larger than those of old stellar systems, such as $Ell13$ and $S0$, due to the strong UV-optical radiation from the massive stars in young stellar systems. Figure 5.5 suggests that the low luminosity variability-selected AGNs ($L_{\rm bol} \sim 10^{44-45}$ erg s^{-1}) at $0.8 \lesssim z \lesssim 2.2$ are hosted in star-forming systems such as Sdm and $M82$.

5.1.3 Host Galaxy Flux Contribution Rate to Structure Function

In section 5.1.1, we focus on the host galaxy to AGN flux ratio derived from the intrinsic AGN SF and the observed SF values. This ratio affects the decrement of the AGN variability amplitude and makes the fake dependencies of wavelength and luminosity. The amount of this effect depends not only on both wavelength and luminosity but also on the type of host galaxy. In this subsection, we test the possible effect for each types of host galaxy in SF analysis.

From equation (5.1.4), we can derive the observed SF values from the intrinsic AGN SF values and the host galaxy to AGN flux ratio. We assume the wavelength and luminosity dependences of the intrinsic AGN SF values ($SF_{\rm AGN}$) and consider the same four host galaxy types ($Ell13$, $S0$, Sdm, $M82$) as introduced in Section 5.1.2. We then calculate the host galaxy to AGN flux ratio with the same procedure described before. We consider the cases of the bolometric luminosity of $\log(L_{\rm bol}/[\text{erg s}^{-1}]) = 44.0, 44.5, 45.0, 45.5$ and 500Å wavelength-bins among 1500-5000Å for wavelength dependency, and the cases of wavelength bins of $\lambda/[\text{Å}]$ = 1500-2000, 2500-3000, 4000-5000 for luminosity dependency. Those results are plotted in Figure 5.6. For the elliptical hosted case, both dependencies are less affected by the host contribution in the shorter wavelength ($\lesssim$ 2500Å) even if the luminosity is fainter. We also plot the contribution rates, defined as $(SF_{\rm AGN} - SF_{\rm total})/SF_{\rm AGN}$, for each host galaxy type in Figure 5.7. For elliptical hosted case, the variability amplitude decreases only by 3.4% and 9.1% of

the intrinsic value at $L_{\rm bol} = 10^{43}$ erg s^{-1} for 1500-2000, 2000-2500Å bin. On the other hand, for younger stellar population systems, such as Sdm and $M82$, the host contribution is high ($\gtrsim$ 30-50%) even if the considering sample is short wavelength bin. This suggests that if less luminous AGNs are hosted in $Ell3$ or $S0$, those variability amplitude are higher and it is easier to detect them than the other younger stellar systems with variability-based AGN selection method. In other words, AGNs hosted in old stellar population systems are less affected by selection bias in variability-based AGN selection method than those hosted in young stellar population systems.

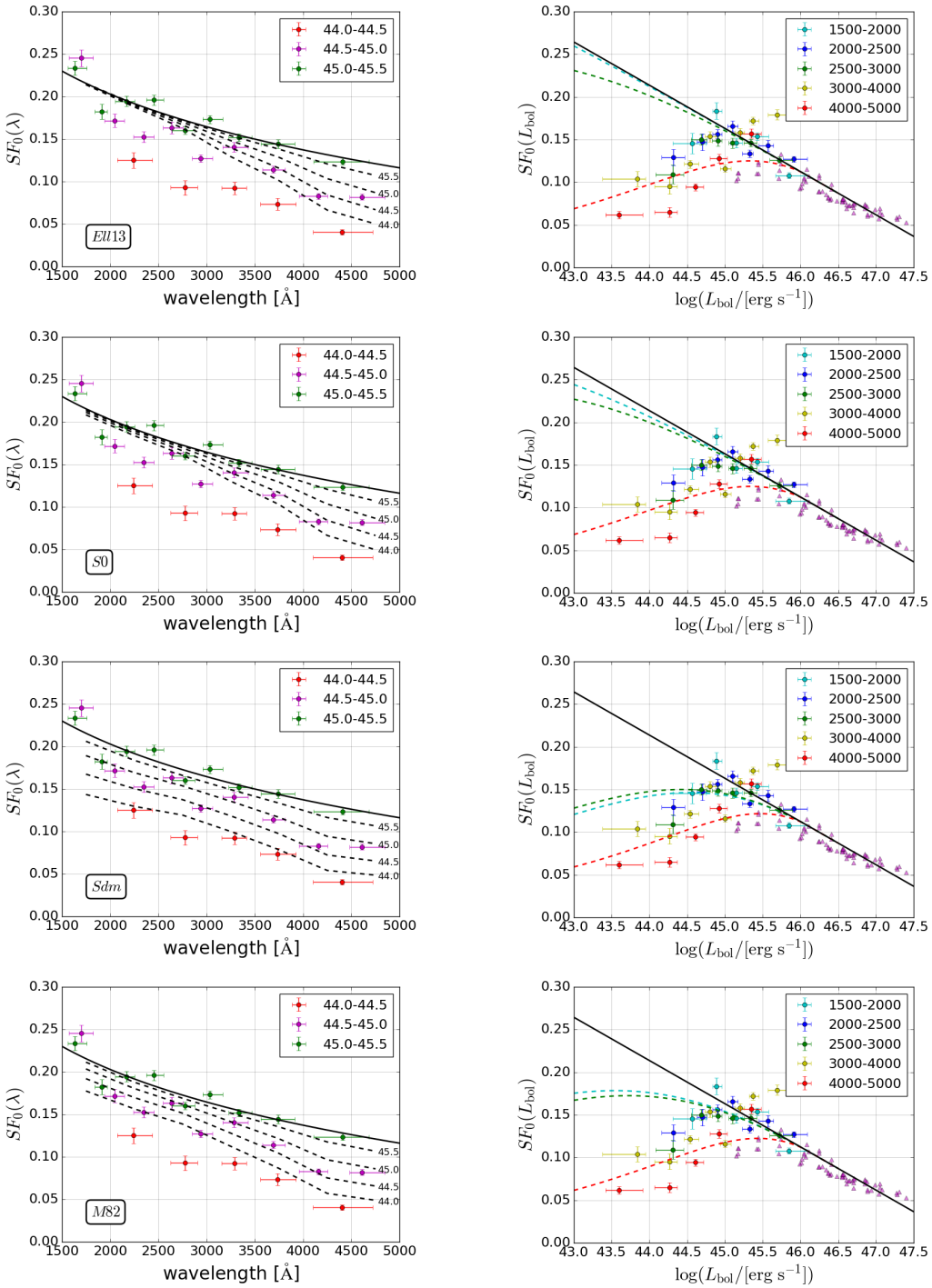

Fig 5.6: Wavelength-dependence (left) and luminosity-dependence (right) for each host galaxy type of elliptical galaxy, S0 galaxy, Sdm galaxy, and starburst galaxy (from the top to bottom panels), respectively. The black lines are the model functions (left: equation (4.2.4), right: equation (4.2.6)). The dashed lines are predicted values for the case of $\log(L_{\rm bol}/[{\rm erg\ s^{-1}}]) = 44.0$, 44.5, 45.0, and 45.5 in the left panel, and $\lambda/[\text{Å}] =$ 1500-2000 (cyan), 2500-3000 (green), and 4000-5000 (red) bins in the right panel.

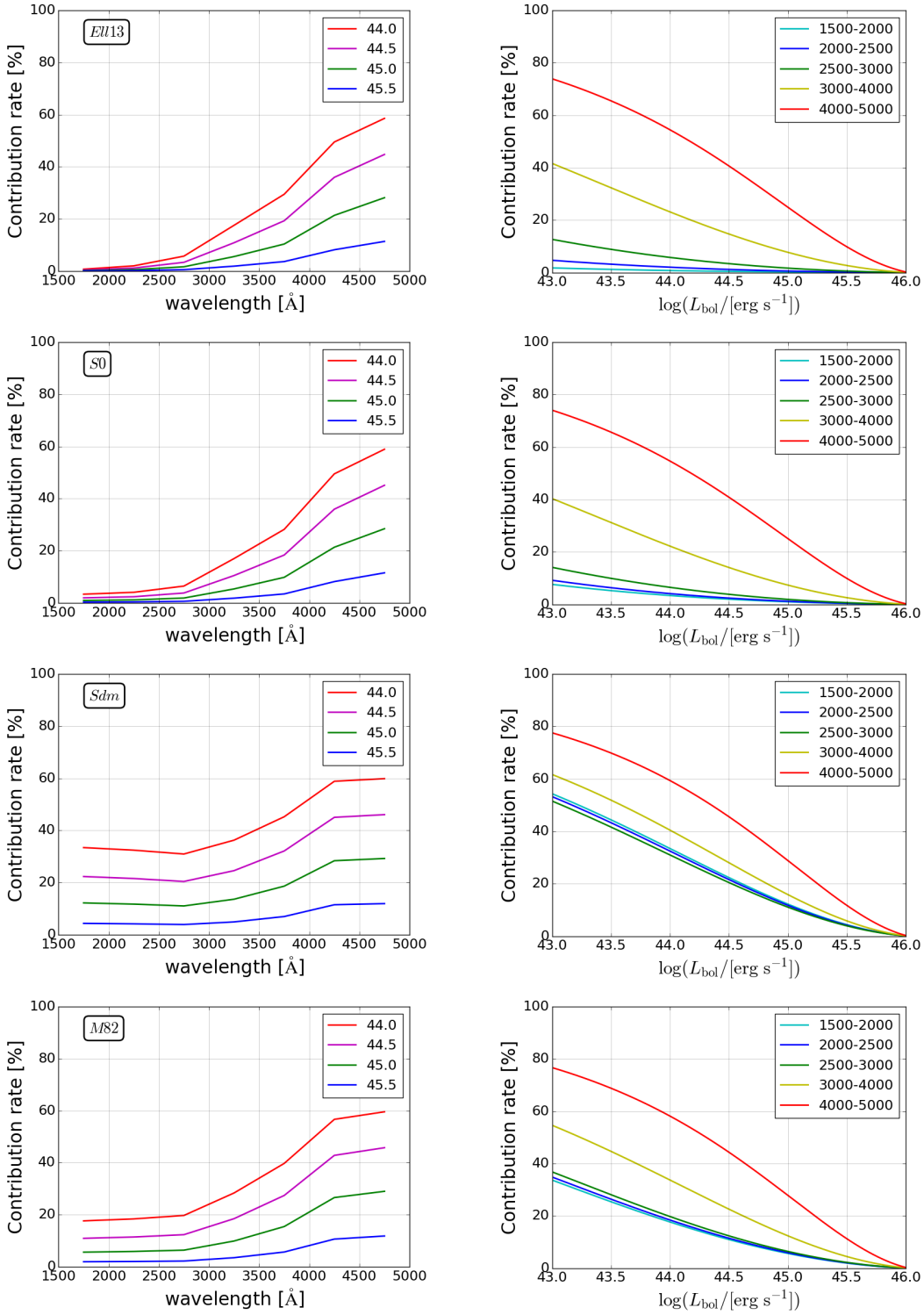

Fig 5.7: Contribution rate as a function of (left) wavelength and (right) luminosity for each host galaxy type of *Ell*13, *S*0, *Sdm*, and *M*82 (from the top to bottom panels), respectively.

5.2 Interpretations of X-ray Absorbed Variable AGNs

The X-undet samples in our variability-selected AGNs show harder stacked X-ray spectra compared to the X-det sample as described in Section 3.2. This harder X-ray spectrum is attributed to X-ray absorption in soft-band if we assume typical X-ray spectrum of type-I AGN. Among the X-undet samples, the lower mass ($M_\star < 10^{10} M_\odot$) subsamples show larger column density ($N_{\rm H} \gtrsim 10^{23}$ cm^{-2}; see Figure 3.7). Previous studies find that at least 10% of optical spectroscopically identified type-I AGNs are X-ray absorbed (Perola et al., 2004; Tozzi et al., 2006; Tajer et al., 2007; Merloni et al., 2014; Shimizu et al., 2018). Our X-undet objects constitute 10% of the entire variability-selected AGN sample, which is consistent with these previous studies for the optical spectroscopically identified type-I AGNs.

What are these optically-unobscured type-I AGNs with significant X-ray absorption? One explanation for these objects is to consider a putative 'neutral gas torus', which is a geometrically thick, dust-free absorption material colocated with or inside of the BLR. The neutral gas torus is assumed to have larger opening angles than that of the dusty torus. If we see the objects from intermediate viewing angles, we can observe them as X-ray absorbed optically-unobscured type-I AGNs (Davies et al., 2015; Liu et al., 2018).

Another possibility is presence of 'shielding gas' in the inner dusty torus, which is related to disk outflows. A fraction of AGNs show outflow signature, which are observed as broad absorption line (BAL) quasars. These objects are considered to have high Eddington ratios (close to or higher than unity). To check the consistency of our stacked samples with such high accretion state, we estimate the Eddington ratios of the X-undet samples. Although there is no direct information about the Eddington ratio for each individual X-undet object, we can estimate the Eddington ratio using AGN bolometric luminosity ($L_{\rm bol}$), stellar mass ($M_\star$), bulge-to-total stellar mass ratio (B/T), and black hole mass-to-bulge stellar mass ratio ($M_{\rm BH}/M_{\rm bulge}$), as follows:

$$\lambda_{\rm Edd} = \frac{L_{\rm bol}}{L_{\rm Edd}} = \frac{L_{\rm bol}}{1.26 \times 10^{38} M_{\rm BH}}$$
$$= \frac{L_{\rm bol}}{1.26 \times 10^{38} (M_{\rm BH}/M_{\rm Bulge})(B/T)(M_\star/M_\odot)}$$
$$= 0.011 \left(\frac{L_{\rm bol}}{10^{43}\ {\rm erg\ s^{-1}}}\right)\left(\frac{M_\star}{10^{10}\ M_\odot}\right)^{-1}\left(\frac{B/T}{0.5}\right)^{-1}\left(\frac{M_{\rm BH}/M_{\rm bulge}}{0.0014}\right)^{-1}. \quad (5.2.1)$$

Here we only consider the low mass ($M_\star < 10^{10}\ M_\odot$) samples in low-z ($z \leq 0.7$) and high-z ($0.7 < z \leq 2.0$), which are possibly affected by strong X-ray absorption (Figure 3.7). We use the median values of the stellar mass of the samples, $\log(M_\star/M_\odot) = 9.10$ and 9.14 for low-z and high-z bin, respectively. We assume that the bulge-to-total stellar mass ratio (B/T) is 0.5 and the black hole mass-to-bulge stellar mass ratio ($M_{\rm BH}/M_{\rm bulge}$) is 0.14% (Häring & Rix, 2004). The AGN bolometric luminosities listed in Table 3.2 are used for the calculation. The calculated Eddington ratios are 0.036 and 0.46 for low-z and high-z bin, respectively. In low-z bin, the Eddington ratio is slightly lower than that expected for BAL quasars. On the other hand, in high-z bin, the Eddington ratio is high, thus it is possible to launch powerful gas outflows. Additionally, in such a high accretion state, the inner region of the accretion disk can be significantly puffed up due to enhanced radiation pressure in the disk (Abramowicz et al., 1988), which is predicted as a narrow line seyfert 1 (NLS1). This thick disk can also absorb the X-ray emission, resulting in a hard X-ray spectrum (Luo et al., 2015).

The origin of the X-undet objects in our variability-selected AGNs is still unclear. To put more stringent constraints on the nature of these objects, such as the Eddington ratio, future deep optical spectroscopic follow-up observations are needed.

6 Summary

In this thesis, we have investigated the properties of AGN multi-band optical variability especially for the low luminosity sample selected by the Subaru HSC SSP survey data set in the COSMOS field, which is one of the most deepest/widest time-domain survey with a ground based telescope so far. Our variability analysis has been conducted for the $\sim$ 3 years data taken from March, 2014 to April, 2017 with the 4 optical filters (g, r, i, z-band), where the single-epoch limiting magnitude is $\sim$ 25 mag.

Combining multiple variability selection criteria using probability-based variability significances, cross-correlations between multi-band light curves, and visual inspection, we have found 491 variability-selected AGN candidates, out of which 441 ($\sim$ 90%) objects are detected in the Chandra X-ray imaging. These variability-selected AGNs have wide a range of bolometric luminosity of $L_{\rm bol} = 10^{43.0-46.5}$ erg s^{-1} and their redshifts reach to 4.26. We have also conducted X-ray stacking analysis for the X-undet samples in our variable AGNs and have detected the X-ray signals, which are lower than the detection limit of the Chandra deep X-ray imaging data. The X-undet samples have harder stacked X-ray spectra compared to the X-det variable AGNs, possibly due to absorption in the soft-band X-ray flux. We have suggested that the X-ray emissions of the X-undet sample are absorbed in the neutral torus, outflowing gas, or the puffed-up accretion disk.

We have shown that the dust covering factor of our variability sample has a similar luminosity dependence to the X-ray absorbed fraction, but slightly lower than the optical spectroscopically or photometrically identified AGNs, that is possibly due to the detection of broad line AGNs with the line width of FWHM $<$ 2000 km s^{-1} in our variability-selected AGN sample.

We have also shown that a certain fraction of the X-undet sample are not selected as AGNs in the MIR color-color diagnostics due to the large flux contamination from the host galaxy light.

Based on the structure function analysis, we have found that the variability

amplitude (at $\Delta t = 100$ days) of the X-det sample is anti-correlated with the wavelength and AGN bolometric luminosity. The variability amplitude is correlated with the time-interval Δt with the power-law slope of 0.487, which is consistent with the expectation from the DRW model, indicating that the AGN variability is caused by the stochastic processes in the accretion disk.

In low luminosity AGNs ($L_{\rm bol} < 10^{45}$ erg s^{-1}), we have found that the observed variability amplitude (at $\Delta t = 100$ days) decreases as the AGN luminosity decrease. This can naturally be interpreted such that the host galaxy flux contamination is more significant for the less luminosity AGNs, which results in the decrease of the variability amplitude. Since this decrement is related to the ratio of host galaxy light to AGN light, we have tried to calculate host galaxy to AGN flux ratio from the observed variability amplitude, and found that the host galaxy to AGN flux ratio increases as the AGN luminosity decreases. This trend is consistent with the previous SDSS quasar studies, suggesting that the decrement of the variability amplitude is a good estimator of the typical host galaxy to AGN flux ratio at a given AGN luminosity. The host galaxy to AGN flux ratio depends not only on the AGN luminosity but also on the wavelength, i.e., depends on the stellar population of the host galaxy. Compared with the host galaxy to AGN flux ratio calculated from the AGN+host galaxy composite spectra, we have shown that dominance of young stellar population is needed to explain the luminosity- and wavelength-dependence of the host galaxy to AGN flux ratio. These results suggest that less luminous AGNs ($L_{\rm bol} \sim 10^{44-45}$ erg s^{-1}) at $0.8 \lesssim z \lesssim 2.2$ are preferentially hosted in star-forming galaxies and the activity of the central black hole is related to the star-formation activity.

Appendix

A Direct SQL Script

```
SELECT forced.ra, forced.dec
FROM   s16a_udeep.forced AS forced
WHERE  coneSearch(coord, 150, 2, 2*3600)
   AND forced.detect_is_primary
   AND NOT forced.gflags_pixel_edge
   AND NOT forced.rflags_pixel_edge
   AND NOT forced.iflags_pixel_edge
   AND NOT forced.zflags_pixel_edge
   AND NOT forced.gflags_pixel_interpolated_center
   AND NOT forced.rflags_pixel_interpolated_center
   AND NOT forced.iflags_pixel_interpolated_center
   AND NOT forced.zflags_pixel_interpolated_center
   AND NOT forced.gflags_pixel_saturated_center
   AND NOT forced.rflags_pixel_saturated_center
   AND NOT forced.iflags_pixel_saturated_center
   AND NOT forced.zflags_pixel_saturated_center
   AND NOT forced.gflags_pixel_cr_center
   AND NOT forced.rflags_pixel_cr_center
   AND NOT forced.iflags_pixel_cr_center
   AND NOT forced.zflags_pixel_cr_center
   AND NOT forced.gflags_pixel_bad
   AND NOT forced.rflags_pixel_bad
   AND NOT forced.iflags_pixel_bad
   AND NOT forced.zflags_pixel_bad
   AND NOT forced.gflags_pixel_bright_object_any
   AND NOT forced.rflags_pixel_bright_object_any
   AND NOT forced.iflags_pixel_bright_object_any
   AND NOT forced.zflags_pixel_bright_object_any;
```

B PSF Map

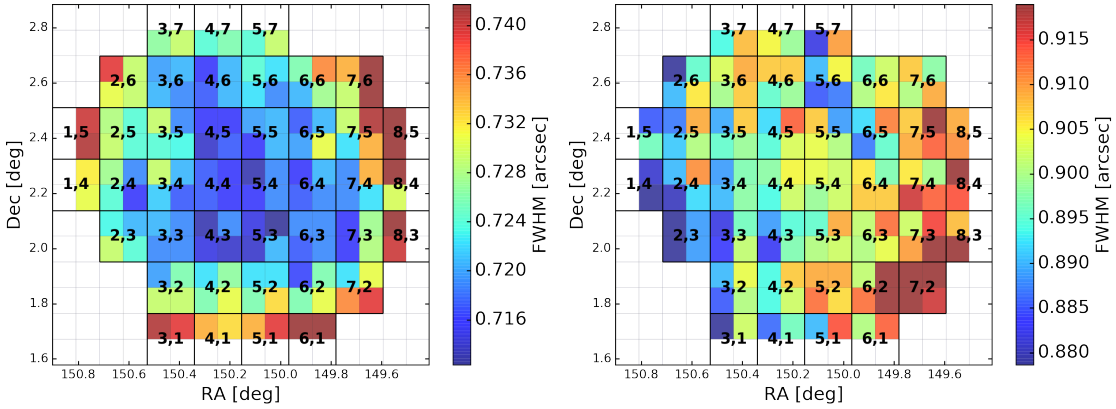

(a) 2014-11-18

(b) 2015-05-17

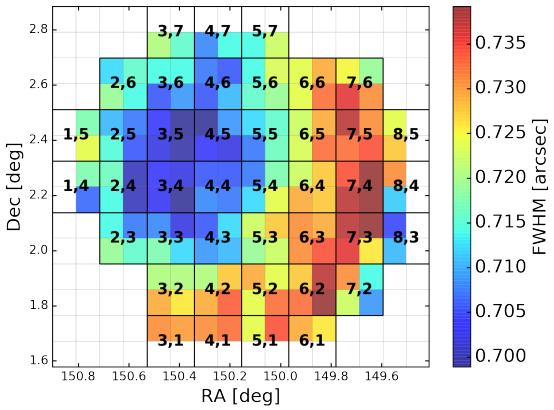

(c) 2016-03-07

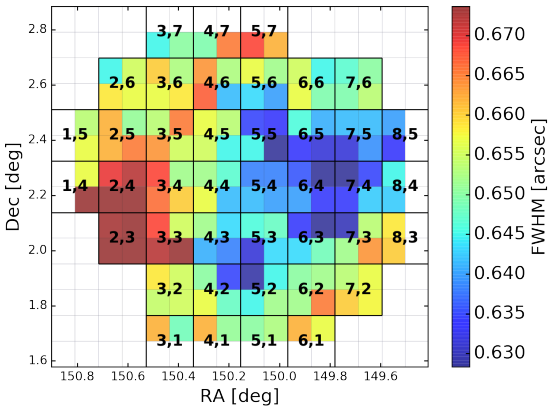

(d) 2017-01-02

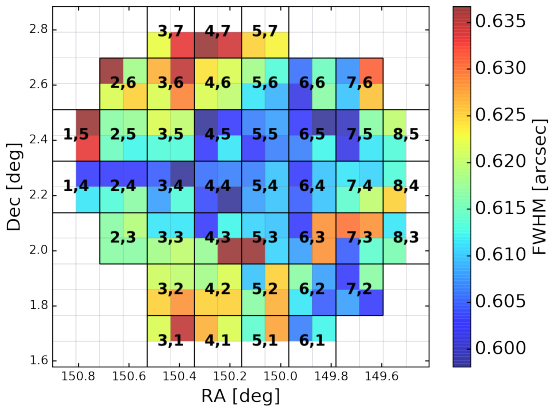

(e) 2017-02-01

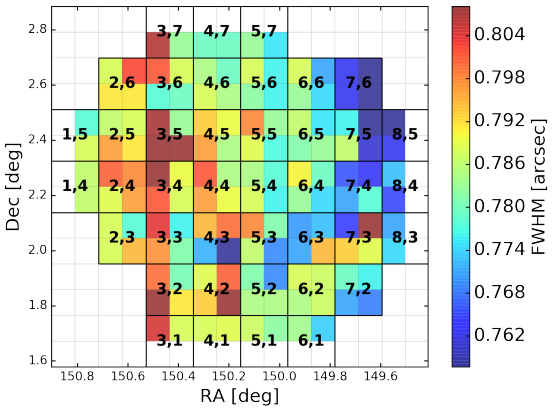

(f) 2017-03-22

Fig B.1: *g*-band

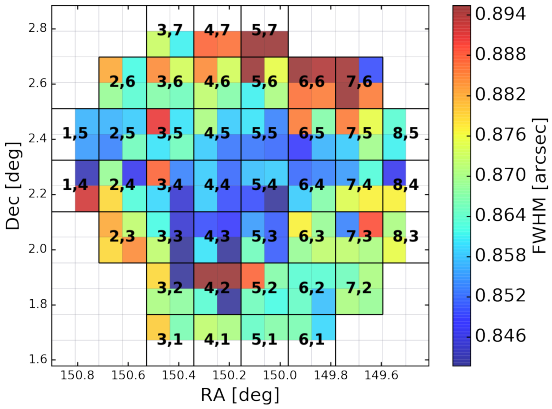

(g) 2017-03-29

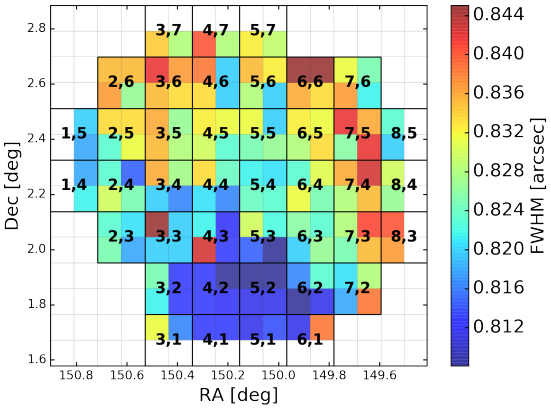

(h) 2017-04-26

Fig B.1: g-band (continued)

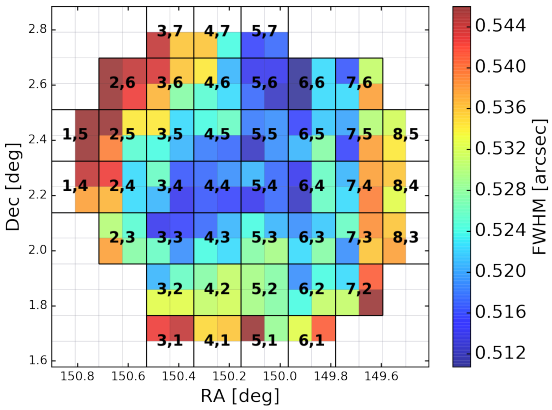

(a) 2014-03-28

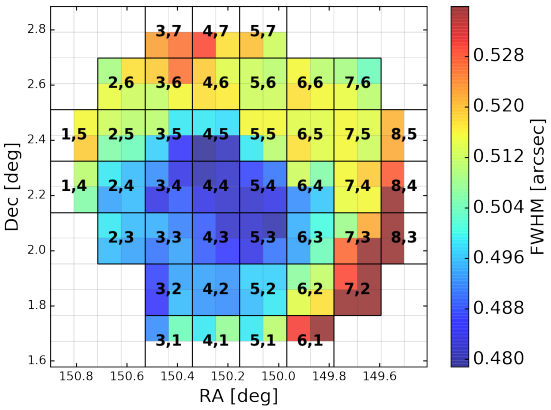

(b) 2015-03-18

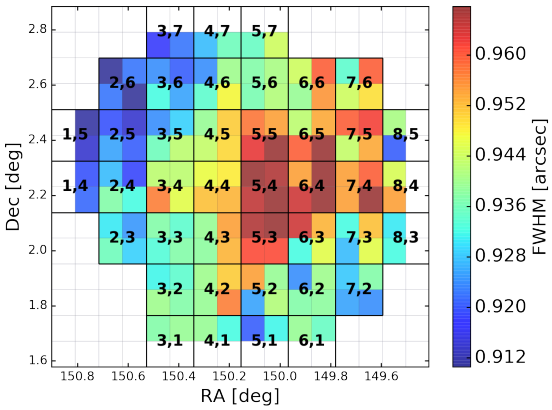

(c) 2016-03-09

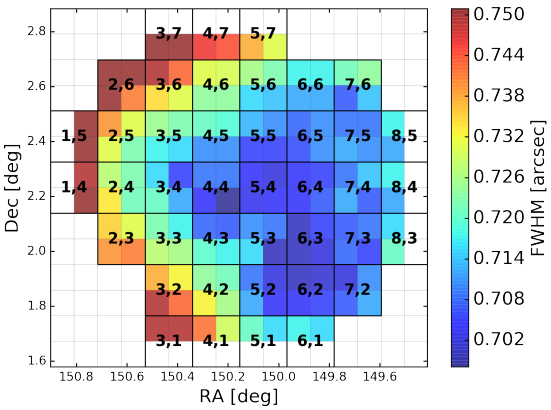

(d) 2016-11-28

Fig B.2: r-band

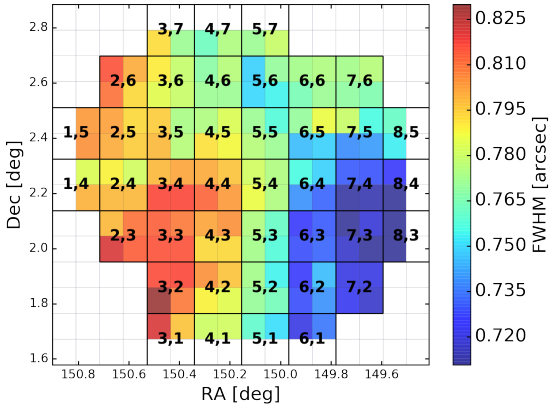

(e) 2017-01-23

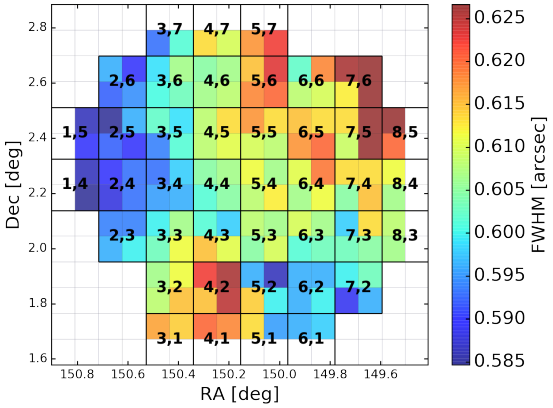

(f) 2017-02-02

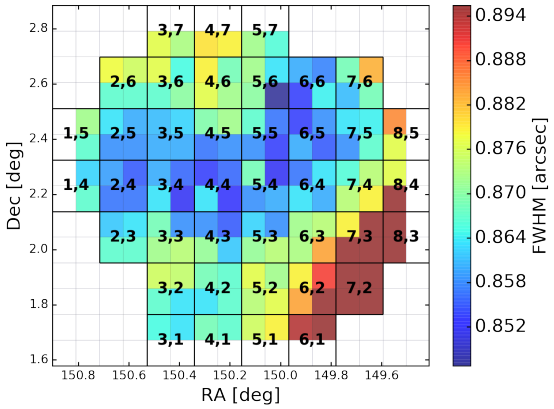

(g) 2017-02-23

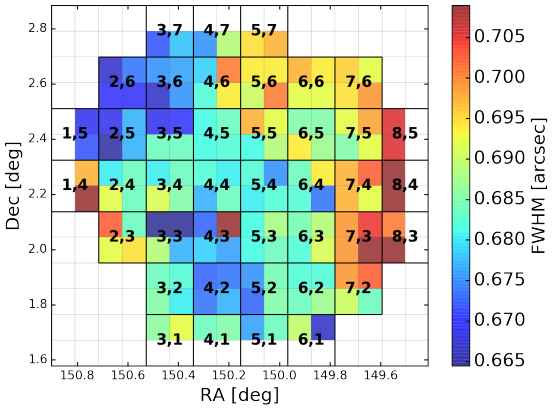

(g) 2017-03-06

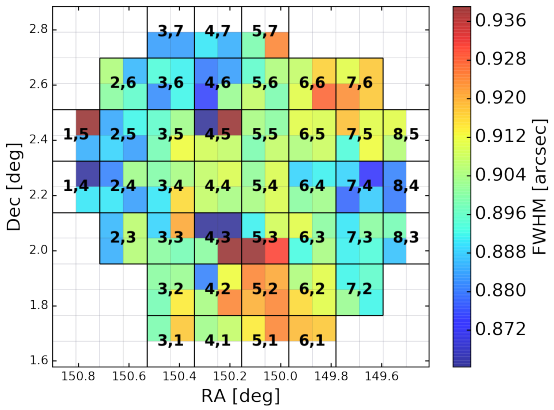

(h) 2017-03-25

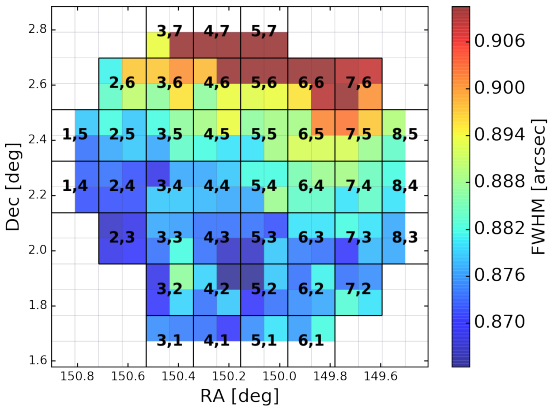

(h) 2017-04-23

Fig B.2: r-band (continued)

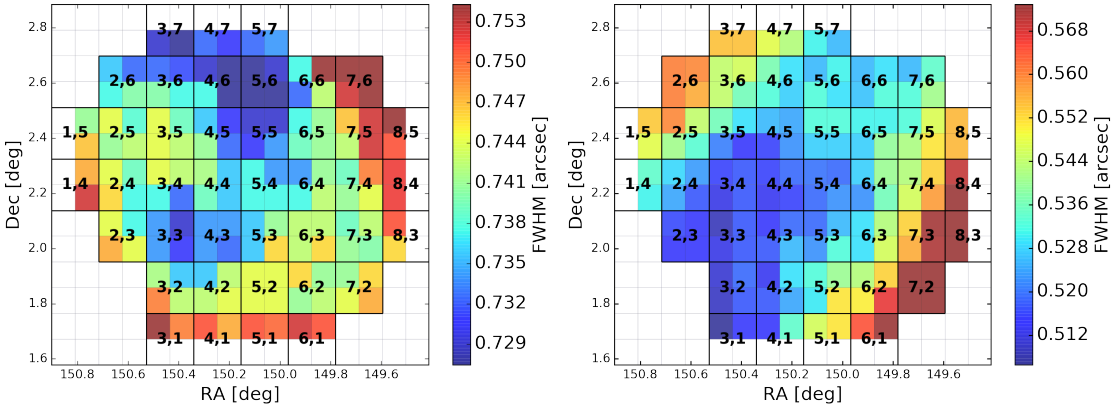

(a) 2014-03-28

(b) 2015-01-21

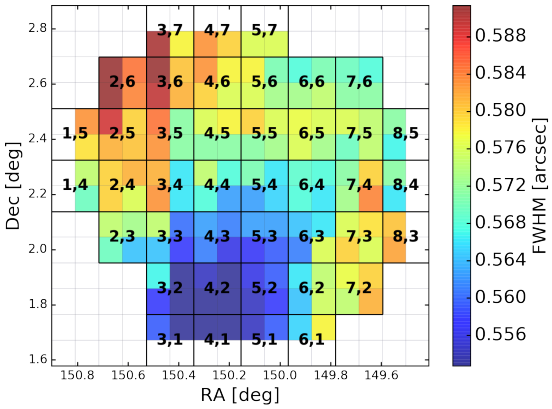

(c) 2015-05-21

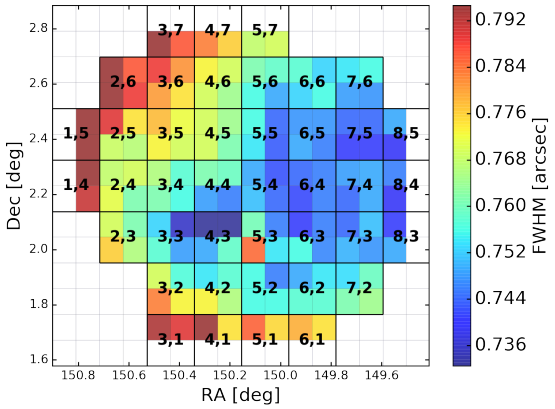

(d) 2016-11-25

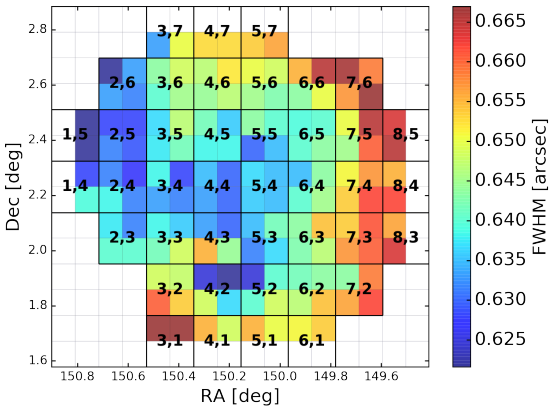

(e) 2017-01-02

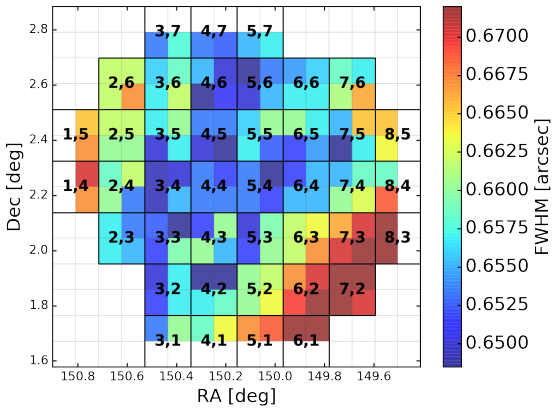

(f) 2017-01-23

Fig B.3: *i*-band

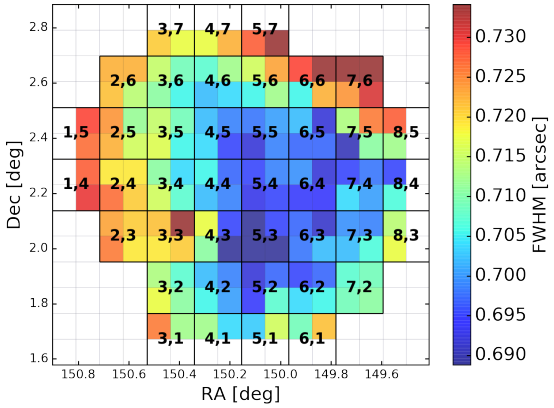

(g) 2017-01-30

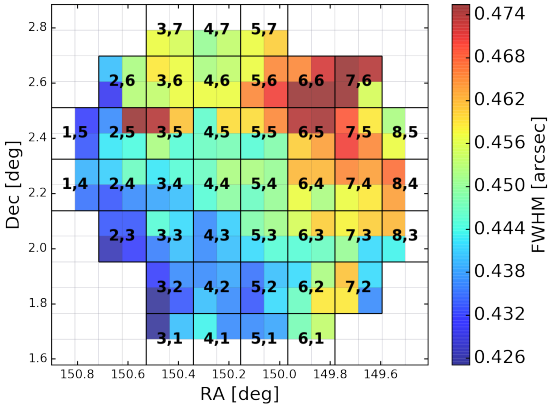

(h) 2017-02-02

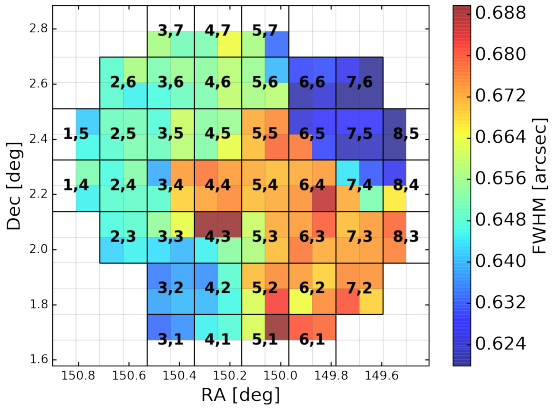

(i) 2017-02-25

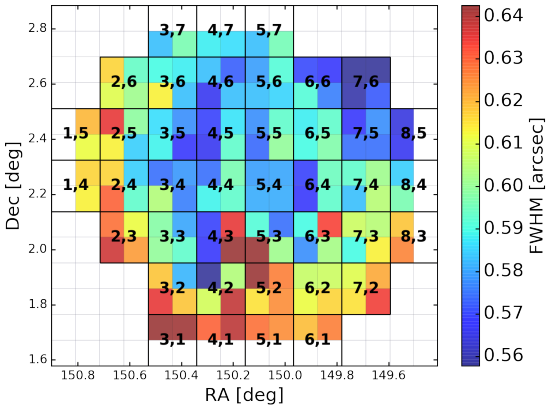

(j) 2017-03-04

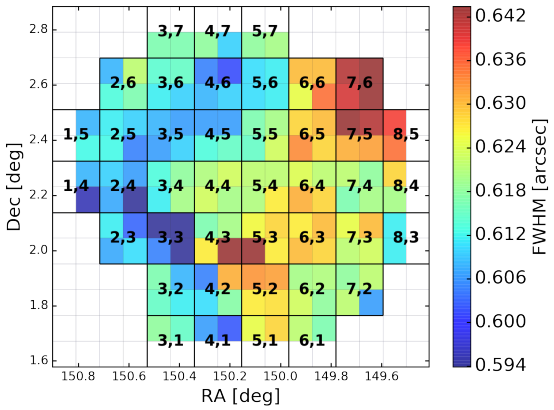

(k) 2017-03-23

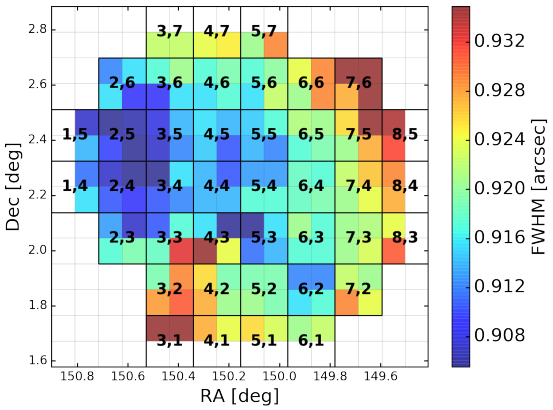

(l) 2017-03-30

Fig B.3: *i*-band (continued)

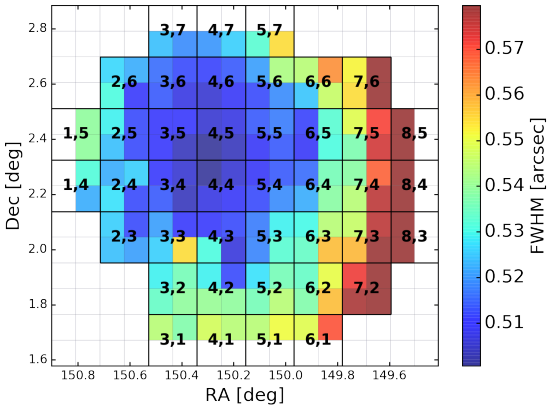

(m) 2017-04-27

Fig B.3: *i*-band (continued)

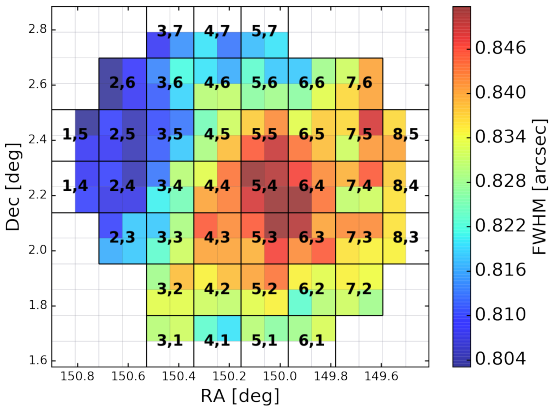

(a) 2014-03-28

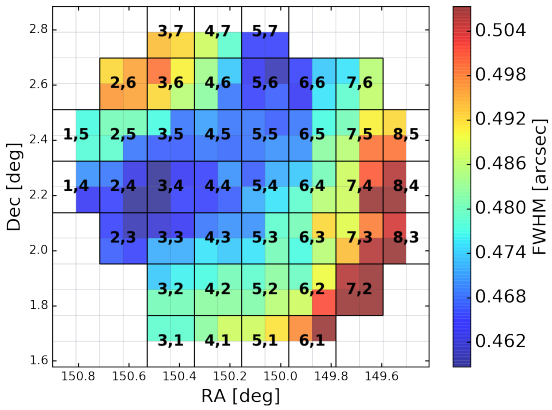

(b) 2015-01-16

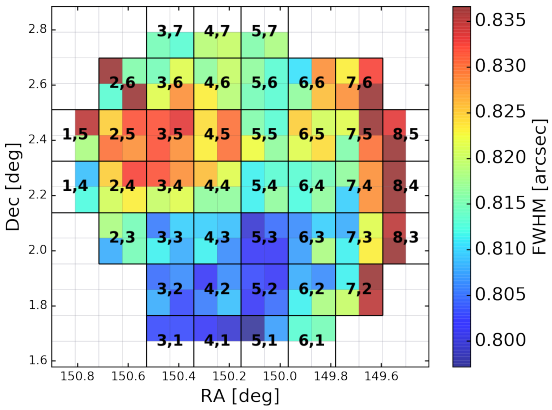

(c) 2016-01-15

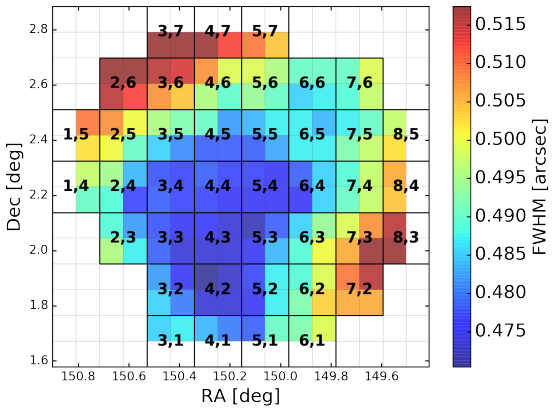

(d) 2016-03-12

Fig B.4: *z*-band

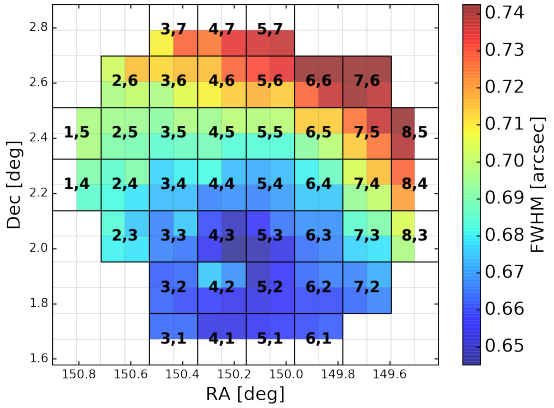

(e) 2016-11-23

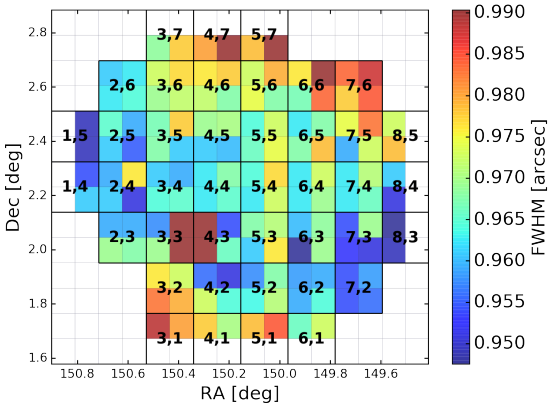

(f) 2016-11-29

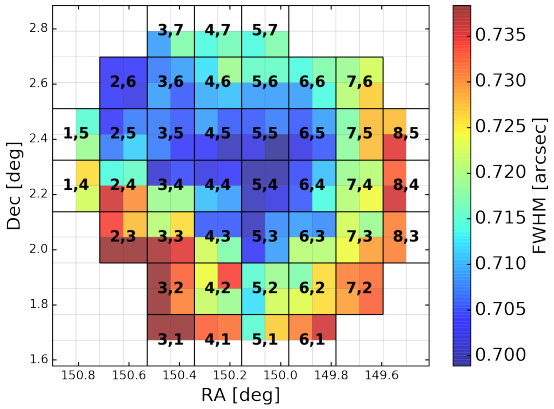

(g) 2017-01-02

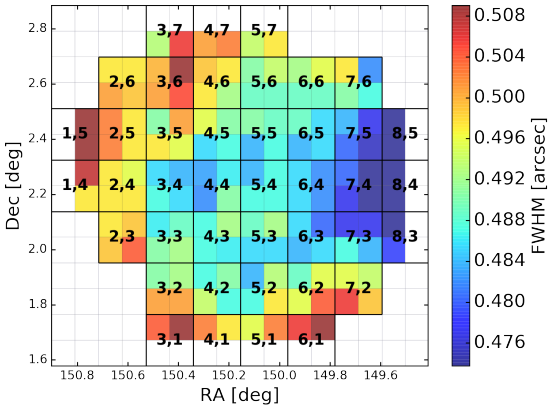

(h) 2017-01-21

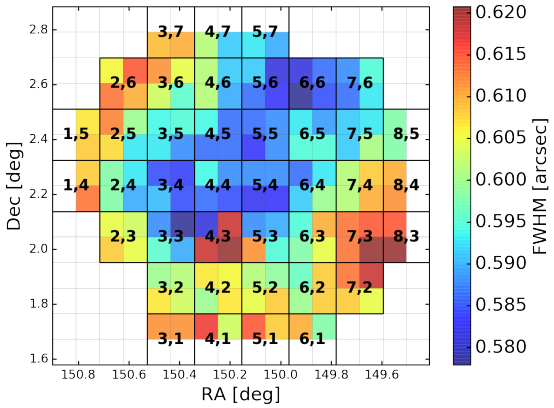

(i) 2017-01-30

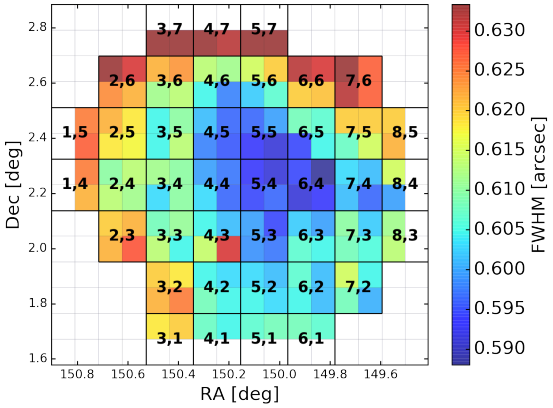

(j) 2017-02-21

Fig B.4: z-band (continued)

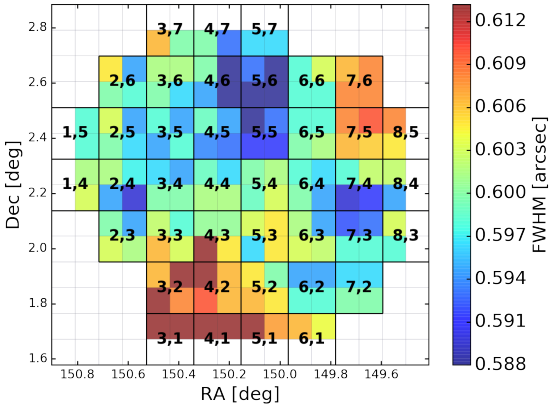

(k) 2017-03-04

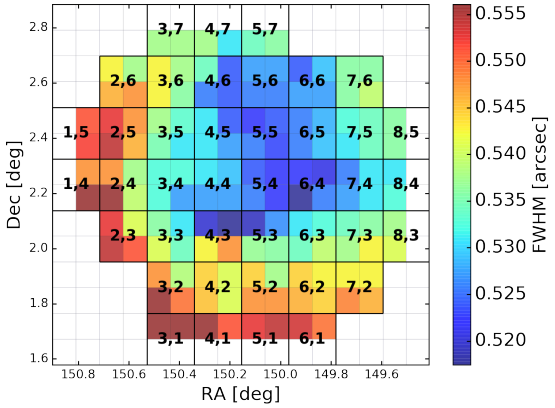

(l) 2017-03-22

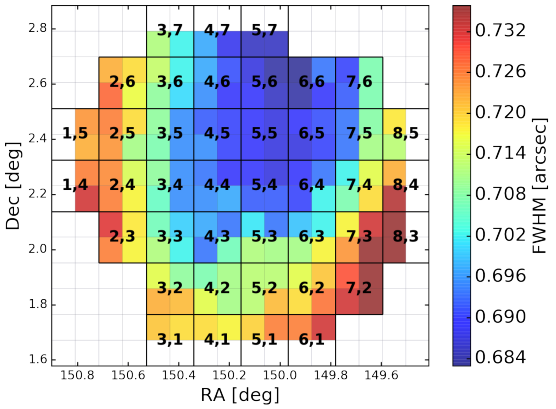

(m) 2017-03-29

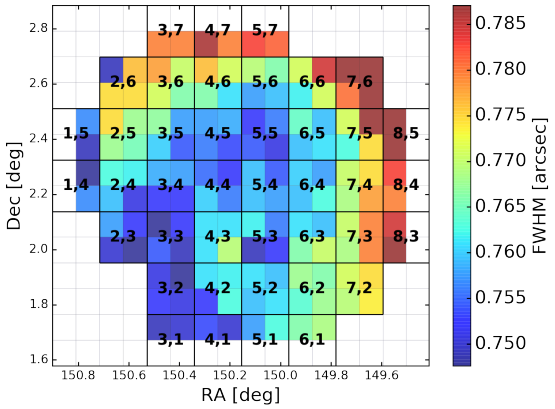

(n) 2017-04-23

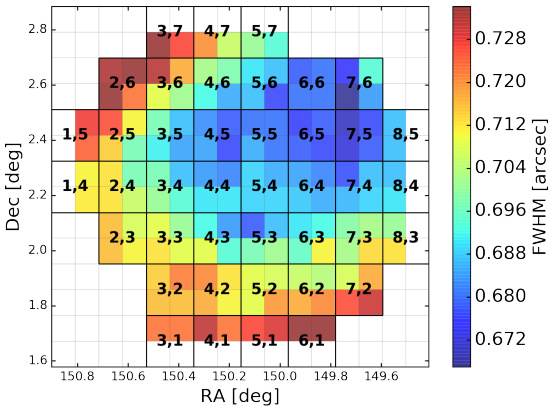

(o) 2017-04-29

Fig B.4: z-band (continued)

C Limiting Magnitude Map

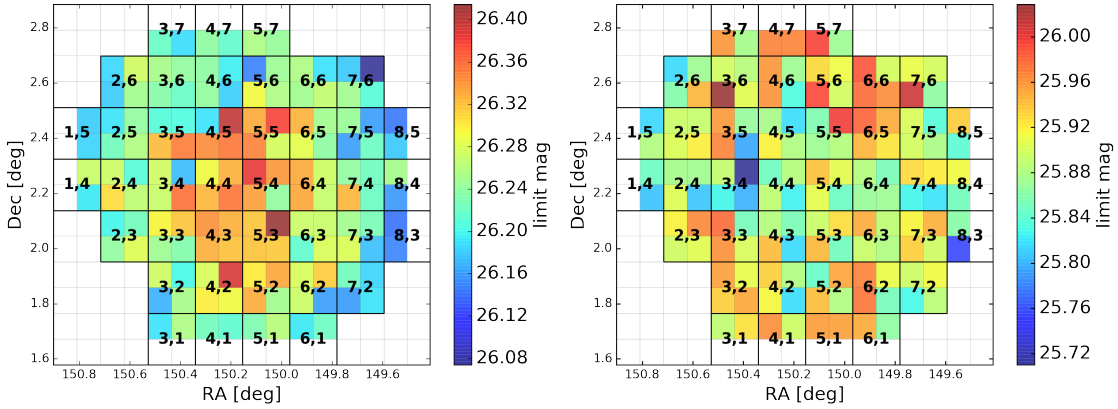

(a) 2014-11-18

(b) 2015-05-17

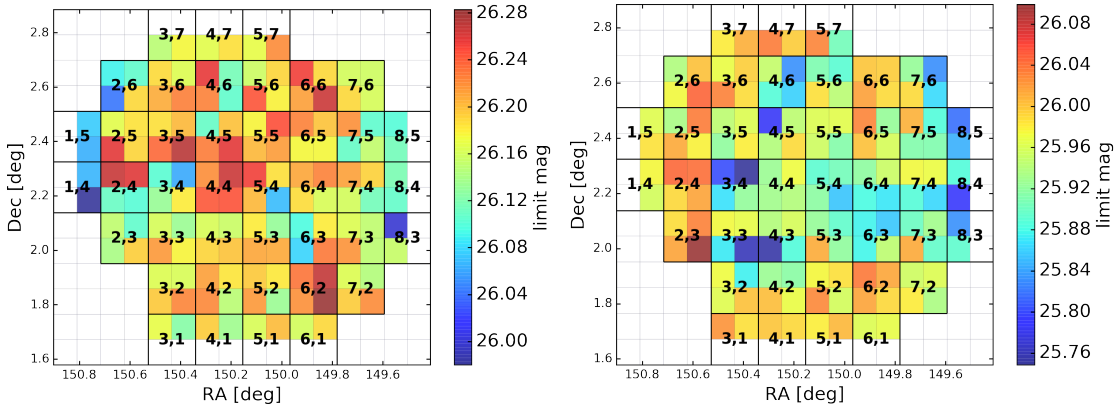

(c) 2016-03-07

(d) 2017-01-02

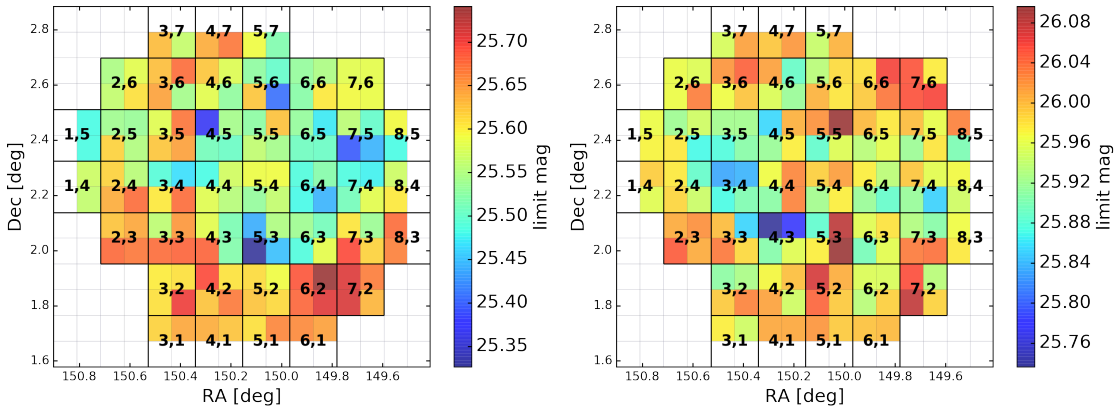

(e) 2017-02-01

(f) 2017-03-22

Fig C.5: g-band

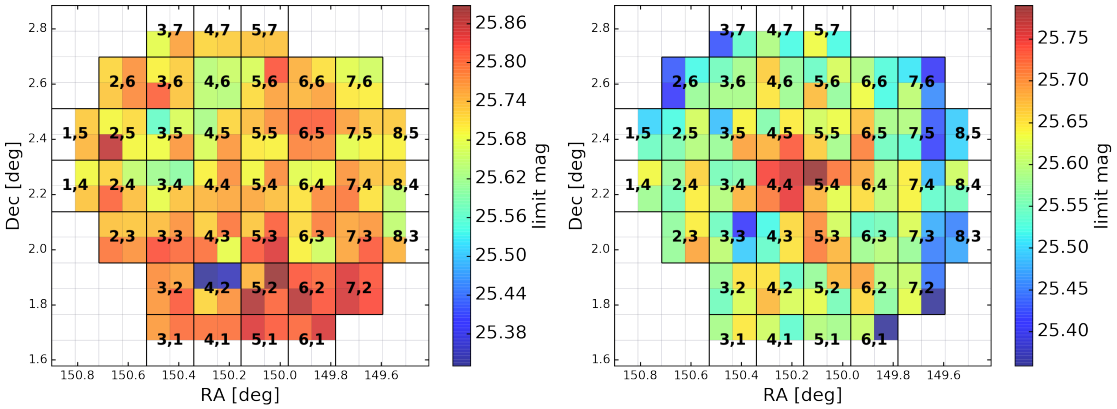

(g) 2017-03-29 (h) 2017-04-26

Fig C.5: g-band (continued)

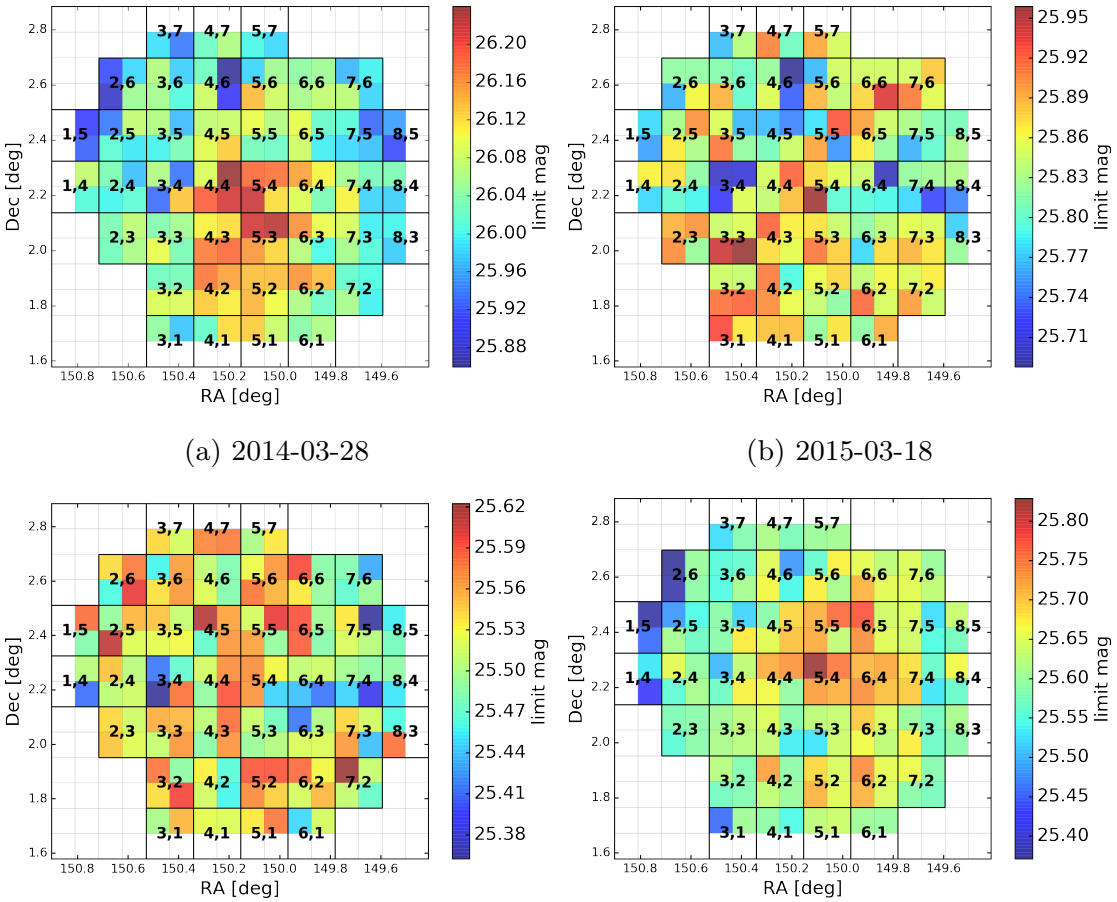

(a) 2014-03-28 (b) 2015-03-18

(c) 2016-03-09 (d) 2016-11-28

Fig C.6: r-band

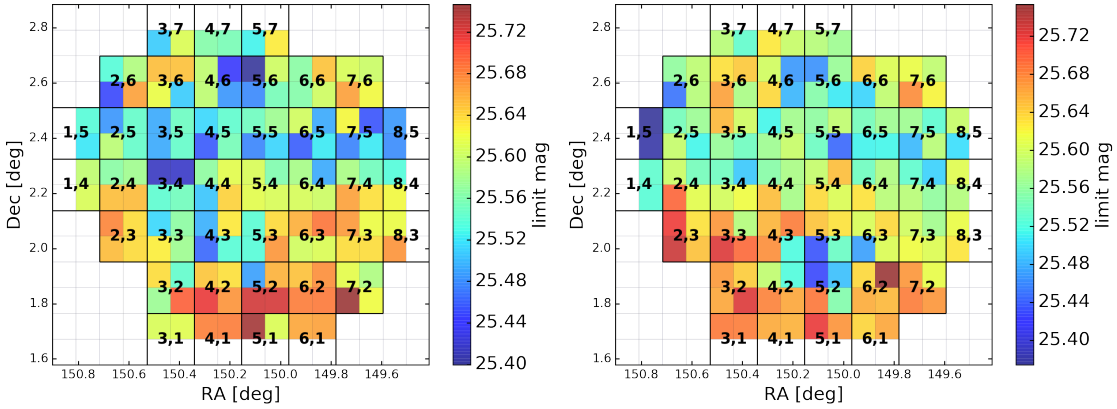

(e) 2017-01-23 (f) 2017-02-02

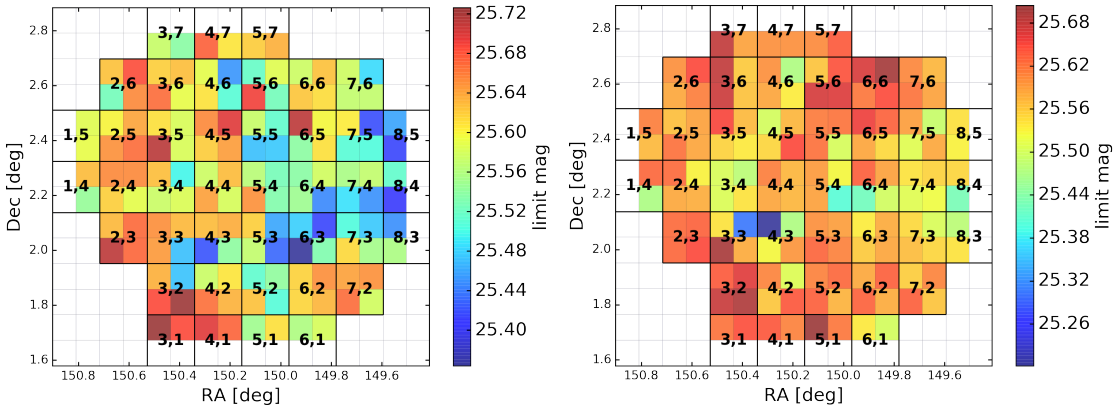

(g) 2017-02-23 (g) 2017-03-06

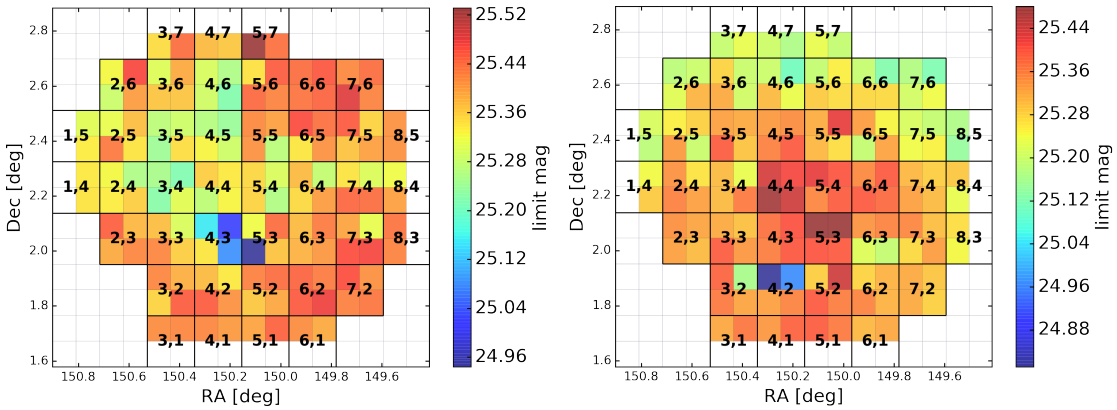

(h) 2017-03-25 (h) 2017-04-23

Fig C.6: r-band (continued)

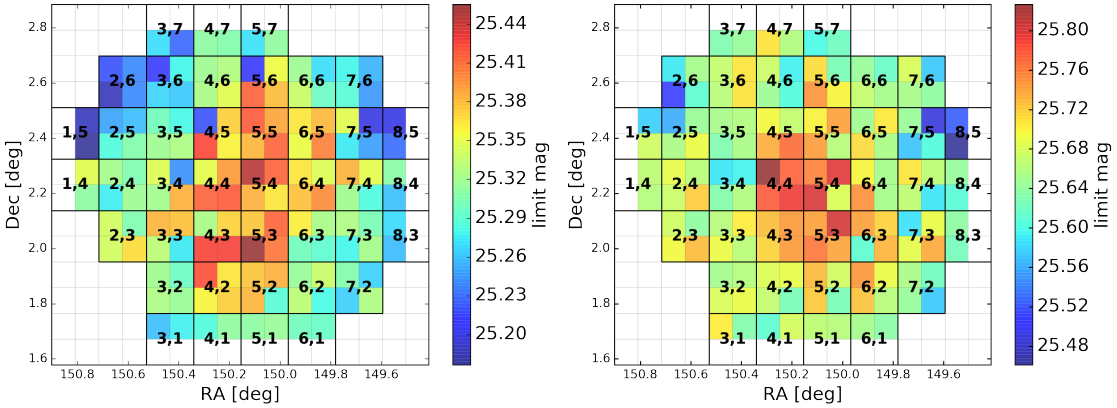

(a) 2014-03-28

(b) 2015-01-21

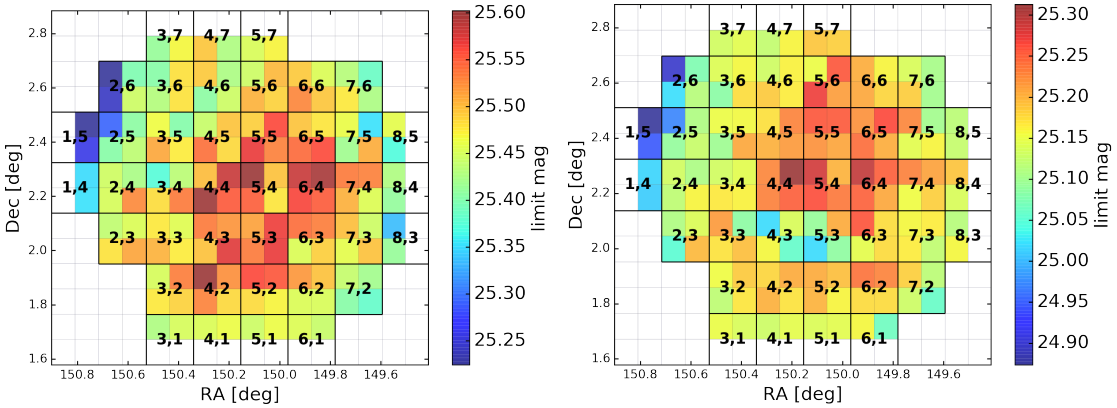

(c) 2015-05-21

(d) 2016-11-25

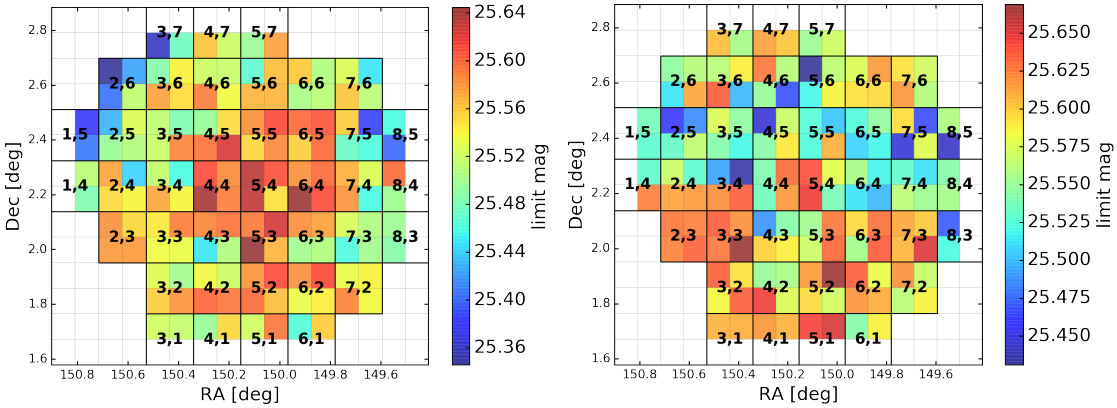

(e) 2017-01-02

(f) 2017-01-23

Fig C.7: *i*-band

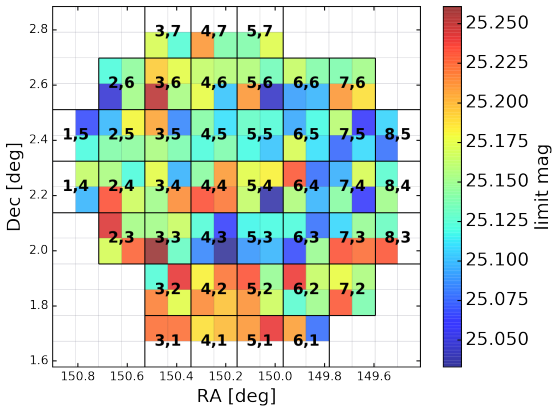

(g) 2017-01-30

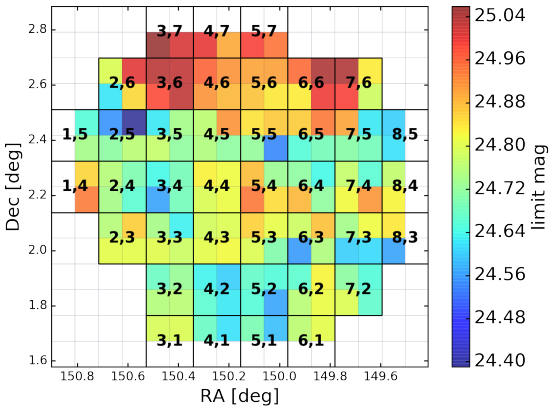

(h) 2017-02-02

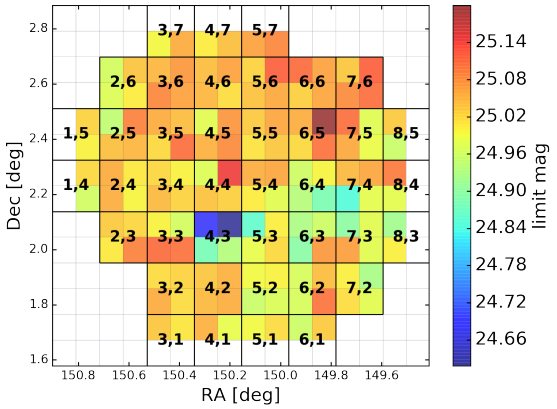

(i) 2017-02-25

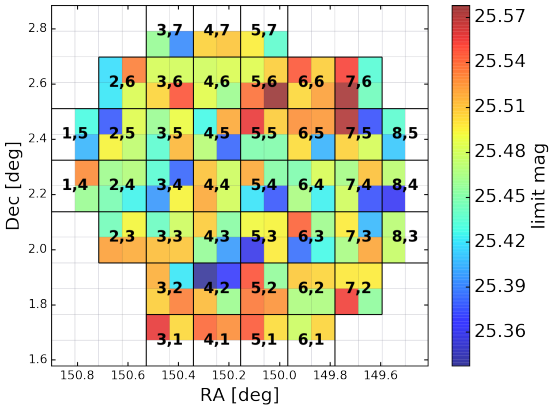

(j) 2017-03-04

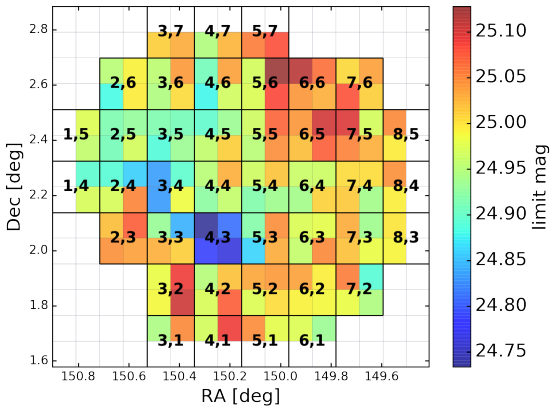

(k) 2017-03-23

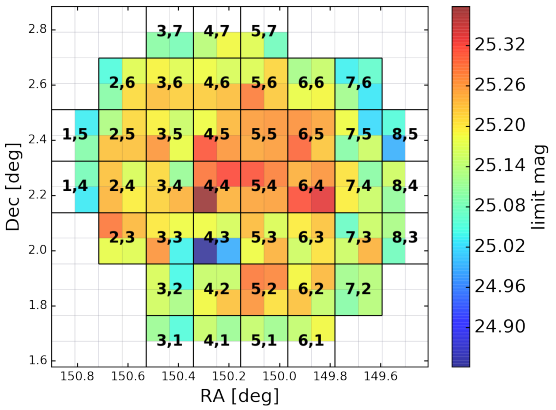

(l) 2017-03-30

Fig C.7: *i*-band (continued)

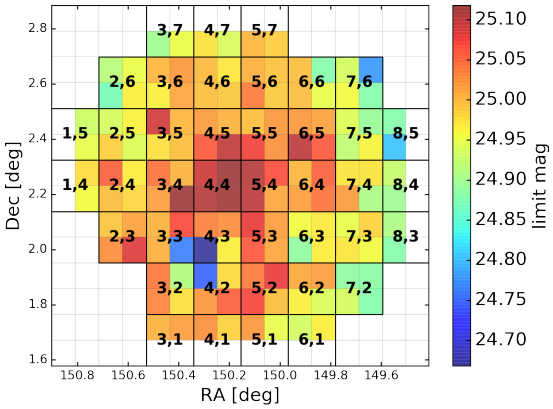

(m) 2017-04-27

Fig C.7: *i*-band (continued)

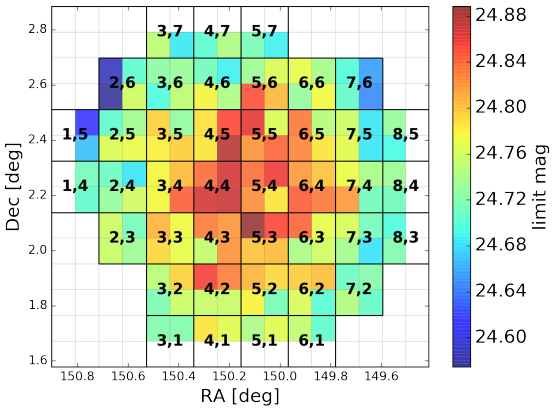

(a) 2014-03-28

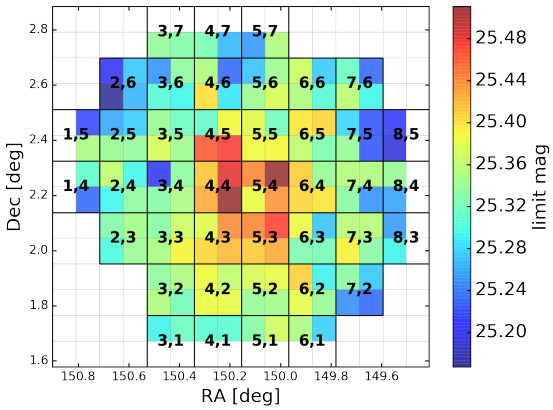

(b) 2015-01-16

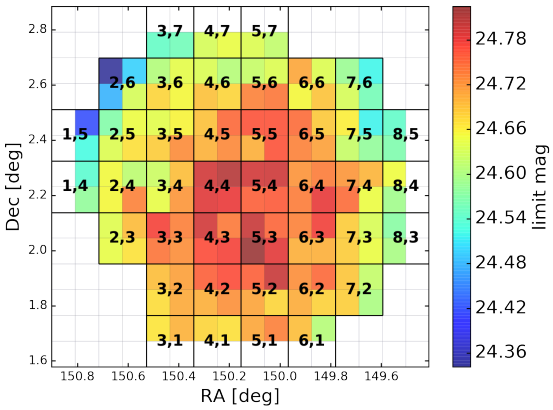

(c) 2016-01-15

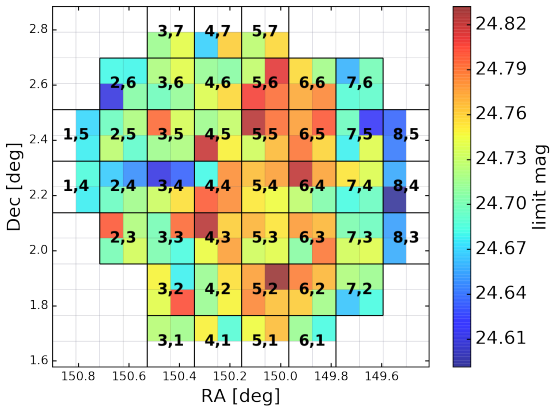

(d) 2016-03-12

Fig C.8: *z*-band

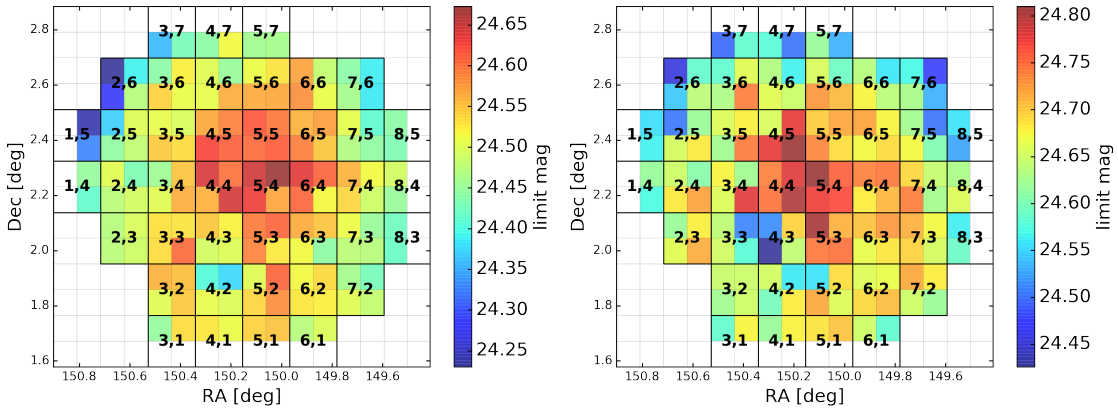

(e) 2016-11-23 (f) 2016-11-29

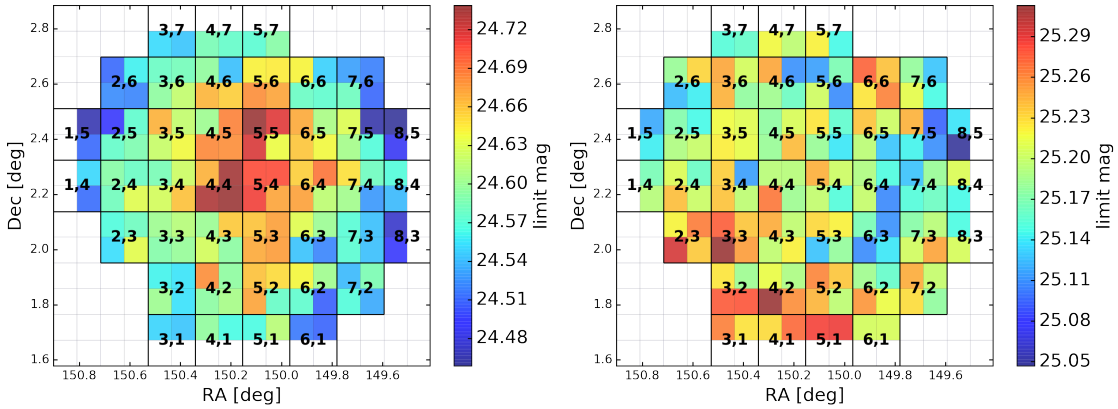

(g) 2017-01-02 (h) 2017-01-21

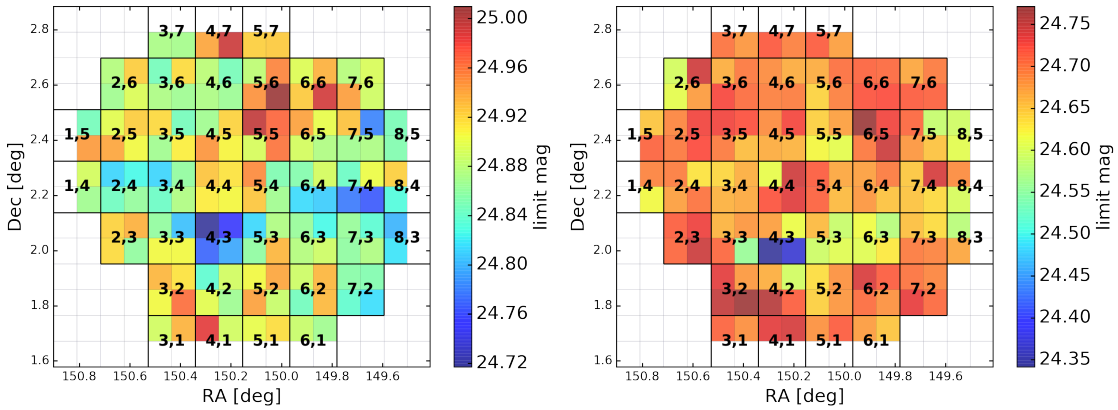

(i) 2017-01-30 (j) 2017-02-21

Fig C.8: z-band (continued)

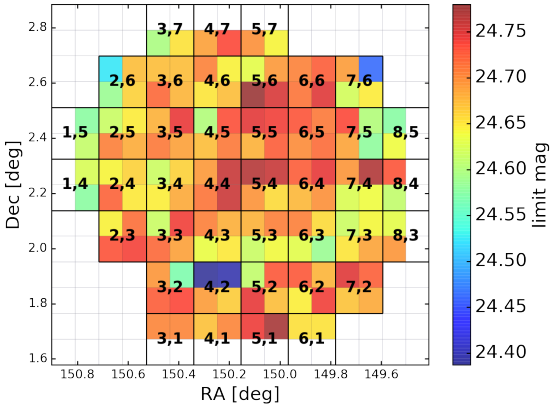

(k) 2017-03-04

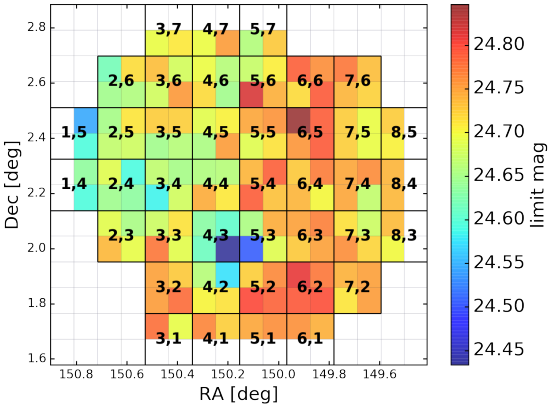

(l) 2017-03-22

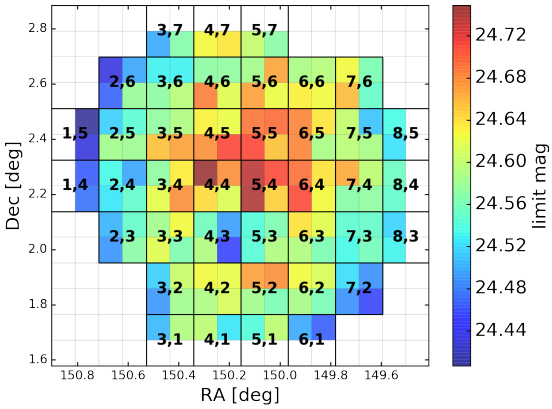

(m) 2017-03-29

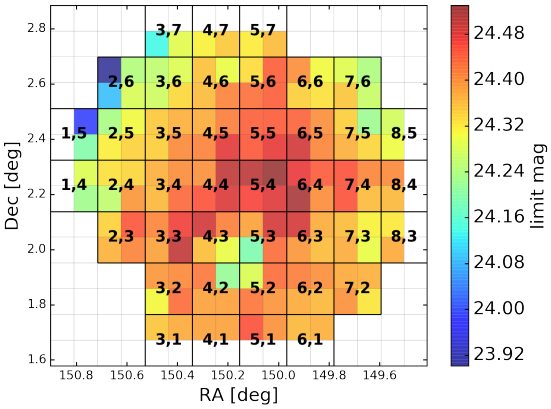

(n) 2017-04-23

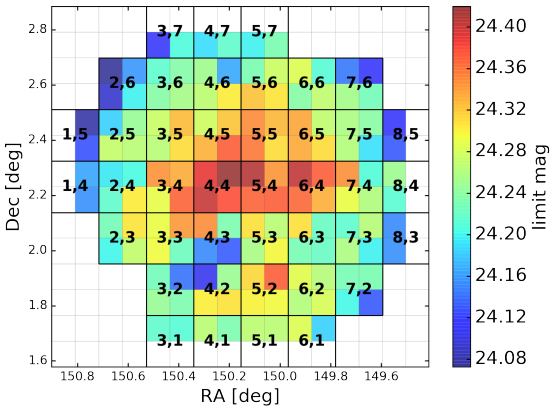

(o) 2017-04-29

Fig C.8: z-band (continued)

D Variability Selected AGN Catalog

Table D.1: Our variable AGN catalog. (1) identification of our variable sample. (2) source coordinates (unit of degree) from the HSC catalog. (3) i-band cmodel magnitude from the HSC catalog. (4) X-ray detection flag from the Chandra catalog (0: X-ray undetected, 1: X-ray detected). (5) variability flag for each band (0: non-variable, 1: variable). (6) the number that satisfies the condition of the correlation coefficient. (7) redshift. (8) reference of redshift (1: spec-z from the HSC catalog, 2: spec-z from the DEIMOS catalog, 3: phot-z from `z_best` in the Chandra catalog, 4: phot-z from `ZPDF` in the COSMOS2015. (9) identification listed in the COSMOS2015.

ID	RA	Dec	i-mag	X-ray	g r i z	$n_{\rm corr}$	redshift	ref.	ID-2015
(1)	(2)		(3)	(4)	(5)	(6)	(7)	(8)	(9)
1	150.7438650	2.2024543	22.71	1	1 1 1 1	6	1.561	3	594392
2	150.7355657	2.1995665	20.36	1	1 1 1 1	6	3.499	1	592797
3	150.7335342	2.1564649	20.88	1	1 1 1 1	6	0.977	1	565402
4	150.7970153	2.1388829	21.01	1	1 1 1 1	6	0.573	1	552225
5	150.7825888	2.1930553	20.63	1	1 1 1 1	6	0.585	1	589540
6	150.7201892	2.2480289	21.13	1	1 1 1 1	6	0.664	1	625595
7	150.7883838	2.3439906	19.82	1	1 1 1 1	6	1.964	1	689768
8	150.7151118	2.4848301	19.20	1	1 1 1 1	6	1.999	1	782508
9	150.7139071	1.9721387	22.87	1	1 1 1 1	5	1.474	3	445280
10	150.6314611	2.0026446	23.26	1	1 1 1 1	6	1.826	2	463657
11	150.6609417	1.9753602	21.47	1	1 1 1 1	6	1.565	1	448411
12	150.6529425	1.9968522	19.52	1	1 1 1 1	6	1.518	1	460965
13	150.6827404	2.0840320	20.72	1	1 1 1 1	5	1.234	3	516177
14	150.5844969	2.0216840	23.28	1	1 1 1 1	6	1.910	3	475665
15	150.6122381	1.9944174	21.40	1	1 1 1 1	6	1.610	1	458826
16	150.5748877	1.9767709	20.98	1	1 1 1 1	6	1.540	1	448517
17	150.5590279	2.1057606	22.61	1	1 1 1 1	6	2.322	1	529336
18	150.5357297	2.0577961	21.75	1	1 1 1 1	6	1.199	1	499247
19	150.7041588	2.2974603	21.59	1	1 1 1 1	6	2.739	1	657703
20	150.7080055	2.2923337	21.09	1	1 1 1 1	6	1.098	1	654576
21	150.5763382	2.1813892	19.16	1	1 1 1 1	5	0.569	1	581391
22	150.5811228	2.2210690	21.92	1	1 1 1 1	6	2.026	1	606414
23	150.5318738	2.1889197	21.58	1	1 1 1 1	6	0.827	1	585366
24	150.6096953	2.3231058	20.44	1	1 1 1 1	6	1.295	1	675269
25	150.6384436	2.3913354	22.56	1	1 1 1 1	6	3.649	3	720289
26	150.6302042	2.4545412	20.20	1	1 1 1 1	6	0.816	1	763207
27	150.5555638	2.3691660	23.29	1	1 1 1 1	6	1.634	2	706553
28	150.5997071	2.3982310	20.77	1	1 1 1 1	6	2.836	1	725685
29	150.5672708	2.5035924	21.03	1	1 1 1 1	6	1.146	3	794377
30	150.6172777	2.4827500	22.59	1	1 1 1 1	6	2.735	3	779775
31	150.5439776	2.4230658	21.92	1	1 1 1 1	6	0.983	1	741600
32	150.7136343	2.5729749	22.59	1	1 1 1 1	6	0.308	1	839943
33	150.6831529	2.5746382	19.16	1	1 1 1 1	6	0.375	1	837822
34	150.6338810	2.5937124	19.13	1	1 1 1 1	6	0.657	1	854964
35	150.6329542	2.5853962	22.07	1	1 1 1 1	6	0.881	1	847966
36	150.7055428	2.6295976	19.97	1	1 1 1 1	6	2.122	1	878244
37	150.6353920	2.6499065	21.04	1	1 1 1 1	6	1.222	1	890325
38	150.6284647	2.6774490	23.05	1	1 1 1 1	6	2.225	3	907047

(continued)

ID	RA	Dec	i-mag	X-ray	g r i z	n_{corr}	redshift	ref.	ID-2015
39	150.5393181	2.5420643	21.94	1	1 1 1 1	6	1.715	1	819172
40	150.5558791	2.5643832	21.89	1	1 1 1 1	6	0.492	1	834538
41	150.5952281	2.5498304	21.81	1	1 1 1 1	6	1.257	1	824613
42	150.6006228	2.5188047	21.54	1	1 1 1 1	6	0.667	1	803830
43	150.5548875	2.6410457	21.58	1	1 1 1 1	6	1.143	1	885687
44	150.5973539	2.6179297	21.27	1	1 1 1 1	6	1.446	1	869891
45	150.4484936	1.6856465	22.05	1	1 1 1 1	6	1.405	3	265264
46	150.4474932	1.6956899	22.04	1	1 1 1 1	6	2.107	3	271177
47	150.3765416	1.7178956	20.06	1	1 1 1 1	6	1.571	1	285627
48	150.3967422	1.7357101	22.29	1	1 1 1 1	6	2.766	3	295934
49	150.4851916	1.8030934	21.96	1	1 1 1 1	6	0.957	3	339381
50	150.4916766	1.7726232	20.86	1	1 1 1 1	6	0.832	1	320331
51	150.4912697	1.9102913	21.95	1	1 1 1 1	6	2.237	1	407347
52	150.4856163	1.8719280	22.23	1	1 1 1 1	6	2.405	1	382203
53	150.4976658	1.8611331	21.86	1	1 1 1 1	6	0.832	1	376362
54	150.3659087	1.8293322	21.63	1	1 1 1 1	6	0.959	1	355652
55	150.3831736	1.7988407	22.34	1	1 1 1 1	5	1.084	1	337029
56	150.4293120	1.8255774	21.74	1	1 1 1 1	6	2.084	1	353591
57	150.3922307	1.8756781	24.42	1	1 1 1 1	6	1.649	3	383885
58	150.3594229	1.9364357	22.48	1	1 1 1 1	6	2.390	1	423522
59	150.3526177	1.9320070	22.77	1	1 1 1 1	6	0.416	1	420196
60	150.4310184	1.9352699	21.47	1	1 1 1 1	6	1.162	1	422734
61	150.4009596	1.9119771	21.06	1	1 1 1 1	6	2.280	1	408043
62	150.4076705	1.8676959	22.53	1	1 1 1 1	6	0.068	1	379110
63	150.4460180	2.0435057	20.82	1	1 1 1 1	6	1.173	1	491067
64	150.4436839	2.0491045	20.11	1	1 1 1 1	6	0.669	1	494577
65	150.3530729	1.9607925	21.30	1	1 1 1 1	6	1.166	1	438137
66	150.4225631	2.0141513	21.79	1	1 1 1 1	6	2.268	1	471626
67	150.4157700	1.9678026	22.70	1	1 1 1 1	6	1.121	1	443133
68	150.4183445	2.0851464	20.08	1	1 1 1 1	6	0.424	1	518166
69	150.4353986	2.1427704	21.53	1	1 1 1 1	6	0.979	1	555407
70	150.4518442	2.1448065	20.64	1	1 1 1 1	6	1.305	1	556169
71	150.4843727	2.1620202	21.84	1	1 1 1 1	6	1.638	1	566857
72	150.5261906	2.2449644	21.02	1	1 1 1 1	6	1.271	1	623618
73	150.4495984	2.2464288	20.67	1	1 1 1 1	6	0.885	1	624526
74	150.4795291	2.2531207	21.69	1	1 1 1 1	6	0.875	1	629377
75	150.5190745	2.3209807	22.24	1	1 1 1 1	6	1.836	3	673948
76	150.3424360	2.2262376	21.71	1	1 1 1 1	6	0.894	1	610703
77	150.3647243	2.1437960	23.24	1	1 1 1 1	6	3.328	3	554731
78	150.3782447	2.1963597	22.49	1	1 1 1 1	6	1.521	1	590258
79	150.3459228	2.1475243	20.74	1	1 1 1 1	6	1.259	1	558958
80	150.4158474	2.1752090	23.63	1	1 1 1 1	6	1.387	2	576066
81	150.4222298	2.1753521	20.94	1	1 1 1 1	6	0.979	3	576870
82	150.3667096	2.3053488	21.58	1	1 1 1 1	6	1.177	1	662467
83	150.3746260	2.3101990	23.05	1	1 1 1 1	6	2.151	3	665457
84	150.3499308	2.2460937	20.82	1	1 1 1 1	6	0.891	1	623908
85	150.4381671	2.4158067	20.49	1	1 1 1 1	6	2.026	1	738308
86	150.4444225	2.3697683	21.49	1	1 1 1 1	6	0.891	1	707186
87	150.4956487	2.4125569	21.62	1	1 1 1 1	6	1.369	1	734723
88	150.4503749	2.3880907	23.01	1	1 1 1 1	3	1.075	3	719419
89	150.5115698	2.4096120	20.99	1	1 1 1 1	6	0.985	1	733581
90	150.5267205	2.3846754	22.37	1	1 1 1 1	6	0.421	1	717885
91	150.4991092	2.4449136	19.03	1	1 1 1 1	4	2.027	1	757535
92	150.3536254	2.3421607	20.36	1	1 1 1 1	6	1.710	1	688136
93	150.4066919	2.3654553	21.80	1	1 1 1 1	6	2.031	1	703733
94	150.3814234	2.5060209	23.99	1	1 1 1 1	6	1.810	3	794241
95	150.4535961	2.5278961	21.03	1	1 1 1 1	6	1.933	1	810108
96	150.4566609	2.6481145	20.36	1	1 1 1 1	6	2.054	1	889205
97	150.4976233	2.6598876	19.94	1	1 1 1 1	6	0.850	1	897743
98	150.5054964	2.6748747	22.05	1	1 1 1 1	6	1.289	2	906149
99	150.3828312	2.5597695	22.94	1	1 1 1 1	6	2.067	1	830661

(continued)

ID	RA	Dec	i-mag	X-ray	g r i z	$n_{\rm corr}$	redshift	ref.	ID-2015
100	150.4159645	2.5257429	22.27	1	1 1 1 1	6	1.444	3	808139
101	150.3514263	2.6782199	21.15	1	1 1 1 1	4	2.753	1	908022
102	150.4907701	2.7754425	20.24	1	1 1 1 1	6	1.437	1	970232
103	150.5045620	2.7250260	22.73	1	1 1 1 1	6	0.491	1	938102
104	150.3820007	2.7583794	21.20	1	1 1 1 1	6	1.228	3	958682
105	150.3828537	2.7236286	22.35	1	1 1 1 1	6	2.055	1	937194
106	150.4015450	2.7907977	21.38	1	1 1 1 1	6	0.923	1	979571
107	150.4056225	2.7232644	23.02	1	1 1 1 1	6	1.266	3	937001
108	150.3618692	2.7791071	22.54	1	1 1 1 1	6	2.535	1	971246
109	150.3199280	1.6815832	19.78	1	1 1 1 1	6	2.055	1	263032
110	150.2799729	1.7438703	22.05	1	1 1 1 1	6	0.762	1	301078
111	150.2592560	1.7572942	21.50	1	1 1 1 1	4	0.965	1	310302
112	150.2624340	1.7514588	23.25	1	1 1 1 1	3	1.675	1	305868
113	150.3062187	1.8751819	23.31	1	1 1 1 1	6	1.755	3	383817
114	150.3386649	1.9281398	22.89	1	1 1 1 1	6	1.197	1	418204
115	150.3088904	1.9123098	21.57	1	1 1 1 1	6	1.483	3	407780
116	150.2277910	1.7868581	22.54	1	1 1 1 1	6	1.681	3	328963
117	150.2425193	1.7664285	20.63	1	1 1 1 1	6	0.622	1	316931
118	150.2102732	1.8538563	22.06	1	1 1 1 1	6	0.934	3	370490
119	150.2451924	1.9001077	20.01	1	1 1 1 1	6	1.560	1	400930
120	150.2082336	1.8753758	20.52	1	1 1 1 1	6	1.148	1	386177
121	150.2430921	1.8691222	20.58	1	1 1 1 1	6	2.021	1	381137
122	150.1617909	1.8779561	21.98	1	1 1 1 1	6	1.443	1	388379
123	150.3119312	2.0357484	20.77	1	1 1 1 1	5	0.970	1	486067
124	150.2534243	1.9966064	21.93	1	1 1 1 1	6	1.170	1	460918
125	150.3118608	1.9779487	21.72	1	1 1 1 1	6	2.349	1	448282
126	150.2856552	2.0145936	21.20	1	1 1 1 1	6	2.669	1	471767
127	150.3242540	2.0890836	22.62	1	1 1 1 1	6	1.073	1	519096
128	150.3343853	2.0614714	20.17	1	1 1 1 1	6	0.903	1	502241
129	150.3069100	2.0538417	23.60	1	1 1 1 1	4	2.009	3	495819
130	150.2163712	1.9887377	21.34	1	1 1 1 1	6	2.242	1	455603
131	150.1807426	2.0759824	22.87	1	1 1 1 1	6	3.010	3	510871
132	150.2721682	2.2300881	21.02	1	1 1 1 1	6	2.611	1	613543
133	150.3026132	2.1610784	20.23	1	1 1 1 1	6	1.826	1	567121
134	150.3165216	2.2467809	21.62	1	1 1 1 1	6	2.491	1	624239
135	150.2623359	2.2563769	23.36	1	1 1 1 1	5	1.776	3	629991
136	150.1584319	2.1395692	20.14	1	1 1 1 1	6	1.829	1	553928
137	150.1800417	2.2312783	23.63	1	1 1 1 1	6	1.400	1	613328
138	150.2146937	2.2042679	20.70	1	1 1 1 1	6	1.840	1	595487
139	150.1997941	2.1908518	20.92	1	1 1 1 1	6	1.502	1	586685
140	150.2362801	2.2891341	21.36	1	1 1 1 1	6	2.077	1	652010
141	150.2542698	2.3306104	22.72	1	1 1 1 1	6	2.458	1	679413
142	150.2527050	2.4863775	21.15	1	1 1 1 1	6	2.040	1	782462
143	150.3080882	2.4300312	20.25	1	1 1 1 1	6	0.375	1	747724
144	150.2997586	2.5068710	21.03	1	1 1 1 1	6	1.505	1	795729
145	150.1740056	2.4029517	22.54	1	1 1 1 1	5	0.972	1	728847
146	150.2107802	2.3914554	22.67	1	1 1 1 1	3	3.095	3	720608
147	150.2318207	2.3639906	20.68	1	1 1 1 1	5	1.933	1	703122
148	150.2355390	2.3617478	22.79	1	1 1 1 1	6	2.501	3	701418
149	150.2446284	2.4322661	20.63	1	1 1 1 1	6	0.693	1	747883
150	150.2090198	2.4384602	21.00	1	1 1 1 1	5	3.727	1	751736
151	150.2088749	2.4818906	19.71	1	1 1 1 1	5	3.348	1	780589
152	150.2925165	2.5450657	21.48	1	1 1 1 1	6	2.656	1	821742
153	150.3238331	2.5525789	22.83	1	1 1 1 1	6	1.633	1	825866
154	150.3179136	2.6020679	20.86	1	1 1 1 1	6	0.957	1	860452
155	150.3344637	2.5614552	19.86	1	1 1 1 1	6	1.835	1	833026
156	150.2762890	2.5263177	22.46	1	1 1 1 1	6	1.436	1	808811
157	150.2992376	2.6334266	23.62	1	1 1 1 1	5	2.987	3	879130
158	150.2977988	2.6734745	21.83	1	1 1 1 1	6	1.593	1	904792
159	150.1713742	2.5640191	20.99	1	1 1 1 1	6	0.510	1	836473
160	150.1638369	2.5976489	21.91	1	1 1 1 1	6	1.588	1	856252

(continued)

ID	RA	Dec	i-mag	X-ray	g r i z	n_{corr}	redshift	ref.	ID-2015
161	150.1862449	2.5564162	21.99	1	1 1 1 1	6	0.653	1	828975
162	150.2308311	2.5781483	19.58	1	1 1 1 1	6	1.401	1	844866
163	150.2326622	2.5442669	24.57	1	1 1 1 1	4	1.404	3	819753
164	150.2241647	2.6511277	22.64	1	1 1 1 1	6	1.749	3	890192
165	150.2977072	2.7387880	23.22	1	1 1 1 1	6	1.633	3	946272
166	150.3385389	2.7767045	22.94	1	1 1 1 1	6	2.130	3	970077
167	150.2555731	2.7703524	20.94	1	1 1 1 1	6	0.781	1	966659
168	150.2513546	2.7371352	20.76	1	1 1 1 1	6	2.164	1	946085
169	150.1670569	2.7689128	21.92	1	1 1 1 1	6	2.387	3	965224
170	150.0518502	1.6827873	20.17	1	1 1 1 1	6	2.274	1	264418
171	149.9916063	1.7243150	20.21	1	1 1 1 1	6	1.628	1	289891
172	150.1317522	1.7994364	20.84	1	1 1 1 1	6	1.674	1	336989
173	150.1245601	1.8098309	22.71	1	1 1 1 1	6	1.441	3	342325
174	150.1016561	1.8483703	19.81	1	1 1 1 1	6	1.667	1	368360
175	150.1169854	1.9298983	22.23	1	1 1 1 1	6	1.519	1	419128
176	150.0814538	1.9060052	23.08	1	1 1 1 1	6	0.971	3	403419
177	150.0254764	1.8776816	22.51	1	1 1 1 1	6	1.796	3	385456
178	150.0426951	1.8721528	23.63	1	1 1 1 1	5	3.325	1	382018
179	149.9887406	1.9324379	22.58	1	1 1 1 1	6	2.395	1	420086
180	150.0730682	2.0035037	20.61	1	1 1 1 1	6	0.352	1	465158
181	150.1456247	2.0430812	20.66	1	1 1 1 1	6	1.178	1	490038
182	150.1055764	2.1263181	21.71	1	1 1 1 1	6	0.961	1	543535
183	149.9952741	2.0066541	21.97	1	1 1 1 1	6	1.037	1	466580
184	150.0044002	2.0389067	21.55	1	1 1 1 1	6	3.508	1	486220
185	150.0589368	2.0151619	19.63	1	1 1 1 1	6	2.499	1	473114
186	149.9917581	2.1319546	22.85	1	1 1 1 1	4	2.135	1	546685
187	150.1009477	2.1677810	22.99	1	1 1 1 1	6	2.055	3	571036
188	150.0958728	2.1451088	22.27	1	1 1 1 1	6	1.323	3	556119
189	150.1129620	2.1648595	22.53	1	1 1 1 1	6	1.927	3	568506
190	150.1380282	2.2916550	17.56	1	1 1 1 1	6	0.184	1	649852
191	149.9698032	2.1834505	22.49	1	1 1 1 1	6	2.900	1	580884
192	150.0285595	2.2099147	21.04	1	1 1 1 1	6	1.258	3	599948
193	150.0182082	2.2594522	22.66	1	1 1 1 1	5	0.045	1	632339
194	149.9936280	2.2585462	20.23	1	1 1 1 1	6	0.660	1	633565
195	149.9939133	2.3014304	19.89	1	1 1 1 1	6	1.792	1	661442
196	150.0044692	2.2371067	21.61	1	1 1 1 1	6	1.406	1	617775
197	150.0645567	2.3290229	21.85	1	1 1 1 1	6	2.445	1	678793
198	150.0915629	2.3990470	21.75	1	1 1 1 1	6	2.475	1	725867
199	150.1236909	2.3582546	20.03	1	1 1 1 1	6	0.726	1	700757
200	150.0621765	2.4550323	20.66	1	1 1 1 1	6	0.732	1	763293
201	150.0042338	2.3891457	23.28	1	1 1 1 1	5	0.090	1	719096
202	150.0201134	2.3536169	21.84	1	1 1 1 1	6	2.663	3	695834
203	150.0587280	2.4773881	20.62	1	1 1 1 1	6	1.260	1	778366
204	149.9769400	2.4866696	22.75	1	1 1 1 1	6	2.089	3	782146
205	150.0210776	2.4203681	22.57	1	1 1 1 1	4	2.186	1	739711
206	150.1036124	2.5507712	20.97	1	1 1 1 1	6	0.497	1	826212
207	150.1044737	2.6912283	21.21	1	1 1 1 1	6	1.881	1	916518
208	150.0805705	2.6345298	21.72	1	1 1 1 1	6	1.065	1	880811
209	150.1268927	2.6265428	21.68	1	1 1 1 1	6	1.834	1	876053
210	149.9925259	2.6825567	23.52	1	1 1 1 1	6	1.233	3	910029
211	150.0452642	2.6884924	21.78	1	1 1 1 1	6	1.436	3	914572
212	150.0425078	2.6291588	20.44	1	1 1 1 1	5	1.572	1	878415
213	150.0343116	2.6411192	21.06	1	1 1 1 1	6	0.517	1	884940
214	150.0606517	2.6479559	20.87	1	1 1 1 1	6	0.425	1	890018
215	150.0306633	2.6787320	21.46	1	1 1 1 1	6	1.950	1	908790
216	150.1257766	2.6988764	23.87	1	1 1 1 1	4	1.465	3	921233
217	150.0585846	2.7303379	21.69	1	1 1 1 1	6	1.141	3	942113
218	150.0084499	2.7045509	20.85	1	1 1 1 1	6	0.598	1	926105
219	149.9766312	2.7348699	23.31	1	1 1 1 1	6	1.870	3	943928
220	149.8079581	1.7092621	21.73	1	1 1 1 1	6	0.954	1	280576
221	149.8347011	1.8176575	21.92	1	1 1 1 1	6	0.734	1	348345

(continued)

ID	RA	Dec	i-mag	X-ray	g r i z	$n_{\rm corr}$	redshift	ref.	ID-2015
222	149.8168773	1.8467323	20.76	1	1 1 1 1	6	1.034	1	367307
223	149.8205311	1.8117547	20.36	1	1 1 1 1	6	0.748	1	346035
224	149.8219316	1.8386570	20.93	1	1 1 1 1	6	1.350	1	361705
225	149.8620414	1.8948471	18.92	1	1 1 1 1	6	0.443	1	397900
226	149.8707829	1.9461937	23.82	1	1 1 1 1	3	2.684	3	429896
227	149.7917861	1.8728732	22.21	1	1 1 1 1	6	1.566	1	383384
228	149.9225593	1.9792226	22.24	1	1 1 1 1	6	2.506	1	449364
229	149.9230545	2.0268955	22.71	1	1 1 1 1	6	2.918	3	478776
230	149.9577283	2.0030976	20.82	1	1 1 1 1	6	1.806	1	464309
231	149.9095462	2.0805815	20.35	1	1 1 1 1	6	2.796	1	514705
232	149.8979315	2.0939202	21.49	1	1 1 1 1	6	1.909	1	521908
233	149.8871528	2.1171771	22.99	1	1 1 1 1	5	0.559	1	536192
234	149.9105324	2.0679846	22.69	1	1 1 1 1	6	1.091	1	505102
235	149.8950985	2.0472104	21.78	1	1 1 1 1	6	2.192	1	491819
236	149.8142051	2.0163283	22.48	1	1 1 1 1	6	1.367	1	472392
237	149.7944280	2.0730813	23.04	1	1 1 1 1	6	0.134	1	508514
238	149.8226911	2.0896484	21.87	1	1 1 1 1	6	2.060	1	519456
239	149.9124423	2.2003171	20.30	1	1 1 1 1	6	0.687	1	593404
240	149.8948307	2.1744324	21.55	1	1 1 1 1	6	1.322	1	575534
241	149.8954014	2.2394686	20.70	1	1 1 1 1	6	1.735	1	619550
242	149.7818986	2.1390598	18.54	1	1 1 1 1	6	0.356	1	554361
243	149.8236193	2.2282704	22.82	1	1 1 1 1	6	2.966	1	611654
244	149.7897664	2.3212048	20.07	1	1 1 1 1	6	0.378	1	674574
245	149.8219423	2.2546483	20.88	1	1 1 1 1	6	0.932	1	631014
246	149.8590545	2.2582423	22.98	1	1 1 1 1	6	0.441	1	631720
247	149.8040653	2.2881276	23.96	1	1 1 1 1	6	2.123	3	650697
248	149.8515598	2.2763980	23.30	1	1 1 1 1	5	3.372	3	643124
249	149.9197738	2.3274220	20.27	1	1 1 1 1	6	1.453	1	678533
250	149.9455302	2.3692592	20.92	1	1 1 1 1	6	0.908	1	706615
251	149.9169375	2.3851802	19.78	1	1 1 1 1	6	1.131	1	717817
252	149.8833368	2.3467321	21.46	1	1 1 1 1	6	1.024	1	691252
253	149.8810212	2.4508288	21.51	1	1 1 1 1	6	1.314	1	761265
254	149.9384252	2.5059589	20.87	1	1 1 1 1	6	0.850	1	795779
255	149.9358846	2.4405848	21.63	1	1 1 1 1	6	0.992	1	753049
256	149.9556338	2.5020432	22.38	1	1 1 1 1	6	1.457	1	792290
257	149.7916244	2.3381998	21.28	1	1 1 1 1	6	1.003	1	686187
258	149.8129322	2.3454633	21.54	1	1 1 1 1	6	1.812	1	691398
259	149.8328454	2.3846787	21.84	1	1 1 1 1	6	2.272	1	716342
260	149.8707097	2.4172707	21.93	1	1 1 1 1	6	1.542	1	737222
261	149.8680264	2.3518532	18.73	1	1 1 1 1	6	0.349	1	696906
262	149.8680553	2.3306856	20.55	1	1 1 1 1	6	1.485	1	681549
263	149.8718421	2.3428646	21.55	1	1 1 1 1	6	1.740	1	688531
264	149.8481509	2.3742377	20.52	1	1 1 1 1	6	2.737	1	709713
265	149.9106719	2.5546518	19.96	1	1 1 1 1	6	0.744	1	829342
266	149.8759098	2.6902649	21.39	1	1 1 1 1	6	2.185	1	915989
267	149.8837718	2.6664291	22.07	1	1 1 1 1	6	0.334	1	900425
268	149.9366592	2.6802288	20.66	1	1 1 1 1	6	1.407	1	909256
269	149.9253967	2.6842313	20.28	1	1 1 1 1	6	1.778	1	912649
270	149.7856421	2.5547902	22.32	1	1 1 1 1	6	0.845	1	828000
271	149.7961929	2.5641118	20.56	1	1 1 1 1	6	0.703	1	834892
272	149.8114375	2.5579780	23.03	1	1 1 1 1	6	2.152	3	830312
273	149.8603163	2.5447541	22.77	1	1 1 1 1	6	0.991	1	821027
274	149.8079977	2.6456778	21.19	1	1 1 1 1	6	2.098	1	887753
275	149.8432443	2.6590588	23.29	1	1 1 1 1	6	3.845	3	895446
276	149.8371001	2.6507544	23.80	1	1 1 1 1	6	1.782	3	889659
277	149.8569318	2.6380323	22.91	1	1 1 1 1	6	0.516	1	882407
278	149.6151454	1.7895673	22.85	1	1 1 1 1	6	1.039	3	330333
279	149.6874744	1.8126605	22.58	1	1 1 1 1	6	1.214	1	344843
280	149.6499580	1.8658733	19.48	1	1 1 1 1	5	2.927	1	379813
281	149.6741826	1.8883735	19.97	1	1 1 1 1	6	1.784	3	393866
282	149.7156099	2.0165160	23.08	1	1 1 1 1	6	2.684	1	472279

(continued)

ID	RA	Dec	i-mag	X-ray	g r i z	$n_{\rm corr}$	redshift	ref.	ID-2015
283	149.7445112	2.0275213	19.39	1	1 1 1 1	6	2.448	1	479975
284	149.7535945	2.1256284	22.36	1	1 1 1 1	6	1.948	1	544338
285	149.7064919	2.1316371	23.98	1	1 1 1 1	5	1.972	3	545954
286	149.6636053	2.0852181	20.18	1	1 1 1 1	6	1.220	1	517100
287	149.6680221	2.1353502	18.57	1	1 1 1 1	6	0.339	1	551328
288	149.7389568	2.2206933	20.37	1	1 1 1 1	6	1.024	1	609017
289	149.7112531	2.1451502	20.31	1	1 1 1 1	6	1.547	1	556928
290	149.7063282	2.2779500	20.61	1	1 1 1 1	6	0.727	1	645944
291	149.6175946	2.2155803	20.51	1	1 1 1 1	6	0.675	1	603725
292	149.6217193	2.2619043	20.74	1	1 1 1 1	6	0.944	1	635497
293	149.6667959	2.2864329	21.02	1	1 1 1 1	6	1.028	1	650453
294	149.7207453	2.3489777	22.05	1	1 1 1 1	6	0.884	1	693350
295	149.7634769	2.3341372	20.99	1	1 1 1 1	6	1.134	1	683219
296	149.7783094	2.4592750	24.04	1	1 1 1 1	6	1.320	2	764321
297	149.6987714	2.4412389	21.23	1	1 1 1 1	6	1.515	1	754140
298	149.7058282	2.4197983	20.39	1	1 1 1 1	6	1.118	1	741487
299	149.7385163	2.4338677	21.52	1	1 1 1 1	6	2.102	1	748454
300	149.7769211	2.4442804	22.41	1	1 1 1 1	5	0.276	1	754803
301	149.6786348	2.3488904	23.36	1	1 1 1 1	6	2.017	3	692317
302	149.6039188	2.3260659	23.63	1	1 1 1 1	6	2.005	2	675793
303	149.6280392	2.4595021	22.16	1	1 1 1 1	6	1.167	1	765668
304	149.6111645	2.4717109	20.59	1	1 1 1 1	6	0.692	1	773838
305	149.7036093	2.5780974	20.48	1	1 1 1 1	6	1.541	1	844144
306	149.6958214	2.5490504	22.44	1	1 1 1 1	6	1.776	1	824019
307	149.7213406	2.5400068	21.57	1	1 1 1 1	6	1.743	1	818249
308	149.6556847	2.6008108	20.66	1	1 1 1 1	5	0.734	1	859825
309	149.6723981	2.6245303	23.21	1	1 1 1 1	6	2.084	3	872373
310	149.6095825	2.6895791	24.13	1	1 1 1 1	6	2.059	3	915011
311	149.5812770	1.9923536	22.25	1	1 1 1 1	6	1.332	1	457171
312	149.5866363	2.0371203	20.48	1	1 1 1 1	6	1.849	1	485406
313	149.5735118	2.0236667	21.52	1	1 1 1 1	6	2.798	1	477130
314	149.5329055	1.9588666	22.03	1	1 1 1 1	5	0.565	2	436688
315	149.5646949	1.9779049	20.97	1	1 1 1 1	6	1.684	1	449276
316	149.5549933	1.9885243	23.20	1	1 1 1 1	6	1.482	3	454808
317	149.5649390	2.0924118	23.18	1	1 1 1 1	5	1.406	3	520729
318	149.5067517	2.0747188	22.34	1	1 1 1 1	6	1.225	1	510152
319	149.5555831	2.0933915	20.31	1	1 1 1 1	6	0.702	1	523113
320	149.5910405	2.1427859	22.64	1	1 1 1 1	6	0.841	1	554257
321	149.5731023	2.3273864	21.06	1	1 1 1 1	6	0.732	1	677692
322	150.6559759	2.2245022	23.25	1	1 1 1 0	2	2.149	3	608549
323	150.6339230	2.4904502	20.67	1	1 1 1 0	3	0.796	1	785922
324	150.6296865	2.4763941	24.13	1	1 1 1 0	2	2.278	3	775611
325	150.4271672	2.0830621	21.73	1	1 1 1 0	3	0.843	3	516335
326	150.4212390	2.2166297	21.34	1	1 1 1 0	3	0.614	1	604416
327	150.4219596	2.3855089	23.34	1	1 1 1 0	3	1.514	3	716954
328	150.4012047	2.7290033	22.75	1	1 1 1 0	3	1.106	1	941454
329	150.3412202	1.7612474	23.72	1	1 1 1 0	1	2.930	3	311121
330	150.2252780	2.3512048	23.80	1	1 1 1 0	3	2.466	2	693397
331	150.3000620	2.7093471	22.62	1	1 1 1 0	3	2.234	1	928556
332	150.1752295	2.7417178	23.54	1	1 1 1 0	3	2.313	3	947925
333	150.1126113	2.0091364	22.88	1	1 1 1 0	2	1.143	1	469052
334	150.1275303	2.5709757	23.28	1	1 1 1 0	3	1.590	3	838473
335	150.0949611	2.6337958	22.74	1	1 1 1 0	3	1.182	2	880531
336	149.9261427	1.7247900	23.64	1	1 1 1 0	2	3.297	3	288867
337	149.9317040	1.8301596	24.38	1	1 1 1 0	2	2.676	3	355258
338	149.7888205	1.8753098	22.94	1	1 1 1 0	3	1.253	3	384414
339	149.8514475	2.1360505	23.91	1	1 1 1 0	3	1.614	3	549460
340	149.9634727	2.2414360	23.68	1	1 1 1 0	2	2.147	3	619689
341	149.7836298	2.3905309	23.47	1	1 1 1 0	3	2.692	3	719700
342	149.8457684	2.4816133	23.50	1	1 1 1 0	2	3.363	2	780592
343	149.9202536	2.5142302	21.65	1	1 1 1 0	3	0.697	1	800486

(continued)

ID	RA	Dec	i-mag	X-ray	$g\ r\ i\ z$	$n_{\rm corr}$	redshift	ref.	ID-2015
344	149.7962910	2.5594379	22.41	1	1 1 1 0	2	1.541	3	830656
345	149.7695336	1.8495802	22.96	1	1 1 1 0	3	2.242	3	367586
346	149.7376577	2.0652001	19.95	1	1 1 1 0	3	0.680	1	505243
347	149.7152731	2.2993889	23.01	1	1 1 1 0	2	1.191	3	658690
348	149.6107050	2.4108459	22.89	1	1 1 1 0	3	1.174	3	732617
349	149.7364897	2.6107449	21.97	1	1 1 1 0	3	1.323	1	864124
350	149.5454607	2.3177198	21.17	1	1 1 1 0	3	0.857	1	672490
351	150.3272261	1.9285999	20.07	1	1 1 0 1	3	0.525	1	419317
352	150.1778465	1.8899488	21.74	1	1 1 0 1	3	0.831	1	394239
353	150.2651927	2.0075847	22.48	1	1 1 0 1	3	0.275	1	466941
354	150.2617360	2.1166394	21.15	1	1 1 0 1	2	1.996	1	536630
355	150.3179943	2.2340701	20.60	1	1 1 0 1	3	0.376	1	616625
356	149.9928612	1.8578848	21.50	1	1 1 0 1	1	0.835	1	373875
357	149.9973997	2.4161827	20.10	1	1 1 0 1	3	0.574	1	737604
358	149.8935069	2.1076580	21.54	1	1 1 0 1	3	1.509	1	532321
359	149.5260242	2.0204883	21.35	1	1 1 0 1	3	0.623	1	475972
360	150.7822268	2.2850813	21.65	1	1 0 1 1	2	3.641	3	649286
361	149.7791033	1.9284862	23.59	1	1 0 1 1	1	2.421	3	417652
362	150.8074918	2.1980715	23.51	1	0 1 1 1	3	1.818	3	590721
363	150.5378800	2.3105114	21.38	1	0 1 1 1	3	1.443	1	666872
364	150.6610740	2.3486627	21.93	1	0 1 1 1	3	0.665	1	692655
365	150.7037871	2.3699890	21.87	1	0 1 1 1	3	3.754	1	706363
366	150.6836969	2.6727396	21.16	1	0 1 1 1	1	0.669	1	905927
367	150.6200211	2.6255374	22.14	1	0 1 1 1	3	1.325	1	873407
368	150.4903471	2.1818978	23.74	1	0 1 1 1	3	2.431	3	579765
369	150.3477175	2.3909897	22.41	1	0 1 1 1	3	1.842	1	720578
370	150.5181524	2.5217164	22.94	1	0 1 1 1	3	2.779	3	806263
371	150.1765658	1.7594948	21.63	1	0 1 1 1	3	1.161	3	311451
372	150.2276099	2.1145313	23.74	1	0 1 1 1	2	1.054	3	534811
373	150.2556066	2.3535302	22.59	1	0 1 1 1	3	2.975	3	694934
374	150.2053532	2.5028955	22.59	1	0 1 1 1	3	3.072	3	792762
375	150.3006567	2.5982335	22.56	1	0 1 1 1	3	0.041	1	856446
376	150.2335441	2.6826057	23.74	1	0 1 1 1	3	1.355	3	910004
377	150.1078915	1.8615419	22.75	1	0 1 1 1	1	1.358	3	377133
378	150.0673636	2.0843260	23.50	1	0 1 1 1	3	2.990	3	516134
379	150.0105240	2.2559048	22.58	1	0 1 1 1	3	1.658	1	629988
380	150.0490705	2.5866403	23.46	1	0 1 1 1	3	1.245	3	849718
381	149.8170745	2.2360368	23.80	1	0 1 1 1	3	1.719	3	616153
382	149.9195251	2.3453712	21.68	1	0 1 1 1	3	3.015	3	690971
383	149.8863121	2.4462107	24.37	1	0 1 1 1	2	1.233	2	756126
384	149.8397688	2.5376176	23.82	1	0 1 1 1	2	1.395	2	816320
385	149.7807506	2.1240589	23.95	1	0 1 1 1	3	1.115	3	540943
386	149.7362083	2.1799379	23.78	1	0 1 1 1	3	4.255	3	578726
387	149.7509207	2.4699059	20.59	1	0 1 1 1	3	0.660	1	772429
388	149.6965746	2.6054906	23.46	1	0 1 1 1	3	1.041	3	860713
389	149.6352929	2.5988571	22.17	1	0 1 1 1	3	2.536	3	856626
390	150.6553202	1.9955974	21.80	1	1 1 0 0	1	0.979	2	459617
391	150.5403956	2.5756549	20.87	1	1 1 0 0	1	0.612	1	842507
392	150.3693677	2.0413106	23.82	1	1 1 0 0	1	1.915	3	487345
393	150.3802213	2.2097604	23.97	1	1 1 0 0	1	2.661	2	598079
394	150.4601487	2.3586019	24.43	1	1 1 0 0	1	2.420	3	698404
395	150.4910042	2.7003038	22.34	1	1 1 0 0	1	1.030	1	923300
396	150.4583146	2.7184014	22.80	1	1 1 0 0	1	1.052	1	934419
397	150.1997411	1.8266199	21.18	1	1 1 0 0	1	0.947	1	355442
398	150.2479304	2.1362342	22.51	1	1 1 0 0	1	0.895	3	550062
399	150.3148496	2.6286994	23.98	1	1 1 0 0	1	2.329	3	876898
400	150.2240013	2.5507453	22.21	1	1 1 0 0	1	0.539	1	825668
401	150.1059853	2.2131395	22.21	1	1 1 0 0	1	0.926	1	601669
402	150.0959059	2.2308922	23.45	1	1 1 0 0	1	1.326	1	612897
403	150.1432487	2.6062092	21.94	1	1 1 0 0	1	0.731	1	861552
404	150.0268235	2.5620319	20.96	1	1 1 0 0	1	0.746	1	833950

(continued)

ID	RA	Dec	i-mag	X-ray	g r i z	$n_{\rm corr}$	redshift	ref.	ID-2015
405	150.1470931	2.7174678	22.64	1	1 1 0 0	1	1.177	1	934234
406	149.9449662	2.0781427	22.51	1	1 1 0 0	1	0.888	1	511953
407	149.9592073	2.3563537	22.09	1	1 1 0 0	1	0.890	1	698425
408	149.7371989	2.0897961	23.14	1	1 1 0 0	1	1.881	1	519494
409	149.5985181	2.2003157	22.15	1	1 1 0 0	1	1.170	3	593532
410	150.4549362	1.9674034	23.85	1	0 1 1 0	1	3.471	3	441487
411	150.2851731	1.7273279	23.64	1	0 1 1 0	1	1.340	3	290561
412	150.2278493	1.8268984	23.39	1	0 1 1 0	1	1.157	1	353402
413	150.3410743	2.3671434	23.96	1	0 1 1 0	1	1.590	3	704286
414	150.0692207	2.2313091	23.50	1	0 1 1 0	1	1.187	1	613159
415	149.8789904	2.1145154	24.68	1	0 1 1 0	1	1.953	2	534240
416	149.9625136	2.3204319	23.63	1	0 1 1 0	1	0.933	2	672268
417	149.5059843	2.1853546	22.02	1	0 1 1 0	1	3.225	3	582749
418	150.7179753	2.4684967	23.55	1	0 0 1 1	1	3.204	2	770406
419	150.5603936	2.0369077	25.02	1	0 0 1 1	1	1.440	3	484756
420	150.5796703	2.2523635	22.94	1	0 0 1 1	1	0.616	1	627823
421	150.6868656	2.5465832	23.00	1	0 0 1 1	1	0.437	1	822926
422	150.4831879	1.9151682	24.16	1	0 0 1 1	1	2.314	3	409604
423	149.9777777	2.3976884	23.58	1	0 0 1 1	1	1.456	2	725012
424	150.0565751	2.3737320	22.89	1	0 0 1 1	1	1.078	1	709134
425	149.9022149	2.3271081	23.71	1	0 0 1 1	1	1.948	3	676717
426	149.7359175	2.0275743	22.63	1	0 0 1 1	1	2.454	3	479881
427	149.6747115	2.2755385	23.86	1	0 0 1 1	1	1.372	2	642649
428	149.5551360	2.4026366	24.49	1	0 0 1 1	1	4.044	2	727144
429	150.5785811	2.1759709	24.27	1	1 0 1 0	1	2.045	3	575697
430	150.5214471	2.3438407	24.56	1	1 0 1 0	1	2.599	3	688302
431	150.1926506	2.2198418	23.68	1	1 0 1 0	1	3.090	3	605445
432	150.0843873	2.2904805	22.60	1	0 1 0 1	1	1.043	1	653385
433	150.0226202	2.1401093	22.91	1	0 1 0 1	1	0.837	3	552419
434	149.9575023	2.6875697	23.40	1	0 1 0 1	1	1.377	3	913409
435	149.8547325	2.6069391	23.19	1	0 1 0 1	1	2.111	3	862187
436	149.6242140	2.1806638	20.77	1	0 1 0 1	1	1.186	1	580915
437	150.7092250	2.1474423	19.74	1	1 0 0 1	1	0.326	1	558743
438	150.6036592	2.6865255	20.94	1	1 0 0 1	1	1.757	1	914962
439	150.0699353	2.1016111	23.60	1	1 0 0 1	1	2.250	3	526398
440	150.0351615	2.0464792	20.21	1	1 0 0 1	1	0.370	3	492525
441	150.1104329	2.7082647	18.43	1	1 0 0 1	1	0.350	1	923481
442	150.6966225	1.9857917	22.70	0	1 1 1 1	6	0.291	4	453072
443	150.6384229	2.5784541	22.22	0	1 1 1 1	6	1.026	1	843386
444	150.5918624	2.6193906	22.92	0	1 1 1 1	6	3.092	4	869382
445	150.4689844	2.3317369	21.43	0	1 1 1 1	6	0.337	1	681106
446	150.4961446	2.3275037	23.76	0	1 1 1 1	2	1.661	4	676889
447	150.4917050	2.4174771	23.37	0	1 1 1 1	6	0.420	1	737476
448	150.3915438	2.5911540	23.06	0	1 1 1 1	6	0.720	4	851352
449	150.2734667	2.3425422	24.04	0	1 1 1 1	6	1.634	4	687951
450	150.3392631	2.6281038	24.23	0	1 1 1 1	5	1.237	4	876267
451	150.0244514	2.2732114	23.34	0	1 1 1 1	5	3.677	4	640964
452	150.1303942	2.4659666	22.97	0	1 1 1 1	6	3.437	4	768961
453	150.0166193	2.4489519	22.67	0	1 1 1 1	6	0.842	4	757715
454	150.0073669	2.6711065	21.28	0	1 1 1 1	3	1.399	1	903304
455	150.1408242	2.7318872	21.19	0	1 1 1 1	6	0.400	4	942848
456	149.8436110	1.7331350	22.91	0	1 1 1 1	6	3.192	4	293947
457	149.8539520	1.7536827	22.51	0	1 1 1 1	6	3.140	4	306758
458	149.9506215	2.3545704	22.04	0	1 1 1 1	6	0.480	1	696561
459	149.6386507	2.2889990	20.25	0	1 1 1 1	6	0.230	4	652276
460	149.6826261	2.4382551	21.49	0	1 1 1 1	6	0.328	1	751481
461	149.5414682	2.2995836	21.81	0	1 1 1 1	3	0.431	1	659386
462	150.4919686	2.3866870	22.45	0	1 1 1 0	3	0.550	1	718762
463	149.9054929	2.3539841	23.02	0	1 1 1 0	3	3.249	4	695302
464	149.6829138	2.1438710	22.98	0	1 1 1 0	3	1.381	4	554866
465	150.7143188	2.0632060	24.01	0	1 1 0 1	3	2.658	4	501586

(continued)

ID	RA	Dec	i-mag	X-ray	g r i z	$n_{\rm corr}$	redshift	ref.	ID-2015
466	150.2802890	2.3516718	20.20	0	1 1 0 1	1	0.678	1	695724
467	150.7087993	2.6656529	22.64	0	1 0 1 1	1	0.165	4	899601
468	150.4559345	1.7164473	24.92	0	0 1 1 1	2	1.733	4	282989
469	150.3834294	1.8542605	22.49	0	0 1 1 1	3	0.716	1	370385
470	150.4045984	2.7805249	22.35	0	0 1 1 1	3	0.599	1	972308
471	150.3219541	2.2744919	21.90	0	0 1 1 1	3	0.974	1	642775
472	150.0685202	2.4094370	22.56	0	0 1 1 1	3	0.685	4	732491
473	150.1028405	2.6301579	21.89	0	0 1 1 1	3	0.538	1	878566
474	149.9707993	2.7495753	23.65	0	0 1 1 1	1	1.290	4	952645
475	149.6532993	2.1446535	23.30	0	0 1 1 1	2	0.272	1	557143
476	150.4677535	1.7152728	25.87	0	1 1 0 0	1	1.764	4	282218
477	150.4023429	2.1453140	20.88	0	1 1 0 0	1	0.478	1	557139
478	150.1922467	2.5445477	23.29	0	1 1 0 0	1	1.174	4	820651
479	150.0734560	1.9791330	24.27	0	1 1 0 0	1	2.591	4	448744
480	150.0673360	2.4851471	23.38	0	1 1 0 0	1	1.322	4	781247
481	150.0219982	2.7911092	21.22	0	1 1 0 0	1	0.822	2	979537
482	149.9103601	2.6955757	21.49	0	1 1 0 0	1	0.851	4	921254
483	150.5508292	2.6828762	23.63	0	0 1 1 0	1	3.493	4	910341
484	150.3224092	2.0412789	25.31	0	0 1 1 0	1	2.771	4	487018
485	150.0936120	2.2372101	22.31	0	0 1 1 0	1	1.175	1	617721
486	149.6940316	2.3343883	23.52	0	0 0 1 1	1	0.497	4	681801
487	149.5888191	2.4968062	23.09	0	1 0 1 0	1	1.217	4	789561
488	150.2897483	2.7532126	23.69	0	0 1 0 1	1	1.914	4	954735
489	150.2496535	1.9529434	22.48	0	1 0 0 1	1	1.107	1	432897
490	150.1697062	2.7813087	20.79	0	1 0 0 1	1	0.710	4	973742
491	150.0352355	2.7278081	21.04	0	1 0 0 1	1	0.509	1	940746

Acknowledgment

First of all, I would like to express the greatest appreciation to my supervisor, Professor Toru Yamada. He gave me various valuable suggestions and advices for my research. He also kindly made a time to discuss about my research no matter how busy he was with his work. His long-term supports enabled me to research with patience. The experiences that I got from him will help me greatly in my future.

I would like to acknowledge three referees for this thesis, Professor Masayuki Akiyama, Professor Tadayuki Kodama, and Associate Professor Takashi Murayama. They gave me various helpful comments and suggestions to improve contents of the thesis and the presentation of the thesis defense.

I would like to thank Dr. Mitsuru Kokubo, Professor Naoki Yasuda, Assistant Professor Tomoki Morokuma, Professor Tohru Nagao, and Associate Professor Yoshiki Matsuoka, for helpful comments and suggestions for my first journal paper, which is based on this thesis. Without their guidances and persistent helps, the paper would not have been possible.

I would also like to gratefully acknowledge all of the members in Astronomical Institute, Tohoku University. I have studied a lot of astrophysics, astronomical observations, and instrumentations through lectures and seminars, and from discussions with them.

Finally, I would like to express my gratitude to my parents, brothers, and grandparents for their endless and unconditional supports, and warm encouragements in my Ph.D. life.

Reference

Abramowicz, M. A., Czerny, B., Lasota, J. P., & Szuszkiewicz, E. 1988, ApJ, 332, 646, doi: 10.1086/166683

Aihara, H., Armstrong, R., Bickerton, S., et al. 2018a, PASJ, 70, S8, doi: 10.1093/pasj/psx081

Aihara, H., Arimoto, N., Armstrong, R., et al. 2018b, PASJ, 70, S4, doi: 10.1093/pasj/psx066

Alam, S., Albareti, F. D., Allende Prieto, C., et al. 2015, ApJS, 219, 12, doi: 10.1088/0067-0049/219/1/12

Antonucci, R. 1993, ARA&A, 31, 473, doi: 10.1146/annurev.aa.31.090193.002353

Bahcall, J. N., & Ostriker, J. P. 1975, Nature, 256, 23, doi: 10.1038/256023a0

Baldassare, V. F., Geha, M., & Greene, J. 2018, ApJ, 868, 152, doi: 10.3847/1538-4357/aae6cf

—. 2019, arXiv e-prints, arXiv:1910.06342. https://arxiv.org/abs/1910.06342

Baldwin, J. A., Phillips, M. M., & Terlevich, R. 1981, PASP, 93, 5, doi: 10.1086/130766

Begelman, M. C., & Rees, M. J. 1978, MNRAS, 185, 847, doi: 10.1093/mnras/185.4.847

Bentz, M. C., Peterson, B. M., Netzer, H., Pogge, R. W., & Vestergaard, M. 2009, ApJ, 697, 160, doi: 10.1088/0004-637X/697/1/160

Bentz, M. C., Peterson, B. M., Pogge, R. W., Vestergaard, M., & Onken, C. A. 2006, ApJ, 644, 133, doi: 10.1086/503537

Bentz, M. C., Denney, K. D., Grier, C. J., et al. 2013, ApJ, 767, 149, doi: 10.1088/0004-637X/767/2/149

Bianchi, S., La Franca, F., Matt, G., et al. 2008, MNRAS, 389, L52, doi: 10.1111/j.1745-3933.2008.00521.x

Bond, J. R., Arnett, W. D., & Carr, B. J. 1984, ApJ, 280, 825, doi: 10.1086/162057

Bosch, J., Armstrong, R., Bickerton, S., et al. 2018, PASJ, 70, S5, doi: 10.1093/pasj/psx080

Brinchmann, J., Charlot, S., White, S. D. M., et al. 2004, MNRAS, 351, 1151, doi: 10.1111/j.1365-2966.2004.07881.x

Caplar, N., Lilly, S. J., & Trakhtenbrot, B. 2017, ApJ, 834, 111, doi: 10.3847/1538-4357/834/2/111

Chambers, K. C., Magnier, E. A., Metcalfe, N., et al. 2016, arXiv e-prints, arXiv:1612.05560. https://arxiv.org/abs/1612.05560

Civano, F., Marchesi, S., Comastri, A., et al. 2016, ApJ, 819, 62, doi: 10.3847/0004-637X/819/1/62

Coil, A. L., Blanton, M. R., Burles, S. M., et al. 2011, ApJ, 741, 8, doi: 10.1088/0004-637X/741/1/8

Cool, R. J., Moustakas, J., Blanton, M. R., et al. 2013, ApJ, 767, 118, doi: 10.1088/0004-637X/767/2/118

Coupon, J., Czakon, N., Bosch, J., et al. 2018, PASJ, 70, S7, doi: 10.1093/pasj/psx047

Crummy, J., Fabian, A. C., Gallo, L., & Ross, R. R. 2006, MNRAS, 365, 1067, doi: 10.1111/j.1365-2966.2005.09844.x

Davies, R. I., Burtscher, L., Rosario, D., et al. 2015, The Astrophysical Journal, 806, 127, doi: 10.1088/0004-637x/806/1/127

De Cicco, D., Paolillo, M., Falocco, S., et al. 2019, arXiv e-prints, arXiv:1905.10374. https://arxiv.org/abs/1905.10374

Dexter, J., & Agol, E. 2011, ApJ, 727, L24, doi: 10.1088/2041-8205/727/1/L24

Elvis, M., Civano, F., Vignali, C., et al. 2009, The Astrophysical Journal Supplement Series, 184, 158, doi: 10.1088/0067-0049/184/1/158

Emmanoulopoulos, D., McHardy, I. M., & Uttley, P. 2010, Monthly Notices of the Royal Astronomical Society, 404, 931, doi: 10.1111/j.1365-2966.2010.16328.x

Fazio, G. G., Hora, J. L., Allen, L. E., et al. 2004, ApJS, 154, 10, doi: 10.1086/422843

Feng, H., & Soria, R. 2011, New Astronomy Reviews, 55, 166 , doi: https://doi.org/10.1016/j.newar.2011.08.002

Fukugita, M., Ichikawa, T., Gunn, J. E., et al. 1996, AJ, 111, 1748, doi: 10.1086/117915

Furusawa, H., Koike, M., Takata, T., et al. 2018, PASJ, 70, S3, doi: 10.1093/pasj/psx079

Gallastegui-Aizpun, U., & Sarajedini, V. L. 2014, MNRAS, 444, 3078, doi: 10.

1093/mnras/stu1648

George, I. M., & Fabian, A. C. 1991, MNRAS, 249, 352, doi: 10.1093/mnras/249.2.352

Gierliński, M., & Done, C. 2004, MNRAS, 349, L7, doi: 10.1111/j.1365-2966.2004.07687.x

Greene, J. E., Strader, J., & Ho, L. C. 2019, arXiv e-prints, arXiv:1911.09678. https://arxiv.org/abs/1911.09678

Haehnelt, M. G., & Rees, M. J. 1993, MNRAS, 263, 168, doi: 10.1093/mnras/263.1.168

Hainline, K. N., Reines, A. E., Greene, J. E., & Stern, D. 2016, ApJ, 832, 119, doi: 10.3847/0004-637X/832/2/119

Häring, N., & Rix, H.-W. 2004, ApJ, 604, L89, doi: 10.1086/383567

Hasinger, G., Cappelluti, N., Brunner, H., et al. 2007, ApJS, 172, 29, doi: 10.1086/516576

Hasinger, G., Capak, P., Salvato, M., et al. 2018, ApJ, 858, 77, doi: 10.3847/1538-4357/aabacf

Heinis, S., Gezari, S., Kumar, S., et al. 2016, ApJ, 826, 62, doi: 10.3847/0004-637X/826/1/62

Hickox, R. C., & Markevitch, M. 2006, ApJ, 645, 95, doi: 10.1086/504070

Hirata, C., & Seljak, U. 2003, MNRAS, 343, 459, doi: 10.1046/j.1365-8711.2003.06683.x

Huang, S., Leauthaud, A., Murata, R., et al. 2018, PASJ, 70, S6, doi: 10.1093/pasj/psx126

Ichikawa, K., Ricci, C., Ueda, Y., et al. 2019, ApJ, 870, 31, doi: 10.3847/1538-4357/aaef8f

Inayoshi, K., Visbal, E., & Haiman, Z. 2019, arXiv e-prints, arXiv:1911.05791. https://arxiv.org/abs/1911.05791

Jarrett, T. H., Cohen, M., Masci, F., et al. 2011, ApJ, 735, 112, doi: 10.1088/0004-637X/735/2/112

Kalberla, P. M. W., Burton, W. B., Hartmann, D., et al. 2005, A&A, 440, 775, doi: 10.1051/0004-6361:20041864

Kaspi, S., Smith, P. S., Netzer, H., et al. 2000, ApJ, 533, 631, doi: 10.1086/308704

Kauffmann, G., Heckman, T. M., Tremonti, C., et al. 2003, MNRAS, 346, 1055, doi: 10.1111/j.1365-2966.2003.07154.x

Kawanomoto, S., Uraguchi, F., Komiyama, Y., et al. 2018, PASJ, 70, 66, doi: 10.1093/pasj/psy056

Kelly, B. C., Bechtold, J., & Siemiginowska, A. 2009, ApJ, 698, 895, doi: 10.1088/0004-637X/698/1/895

Kewley, L. J., Dopita, M. A., Sutherland, R. S., Heisler, C. A., & Trevena, J. 2001, ApJ, 556, 121, doi: 10.1086/321545

Kewley, L. J., Nicholls, D. C., & Sutherland, R. S. 2019, ARA&A, 57, 511, doi: 10.1146/annurev-astro-081817-051832

Koekemoer, A. M., Aussel, H., Calzetti, D., et al. 2007, The Astrophysical Journal Supplement Series, 172, 196, doi: 10.1086/520086

Kokubo, M. 2015, MNRAS, 449, 94, doi: 10.1093/mnras/stv241

Komiyama, Y., Obuchi, Y., Nakaya, H., et al. 2018, PASJ, 70, S2, doi: 10.1093/pasj/psx069

Korista, K. T., Alloin, D., Barr, P., et al. 1995, ApJS, 97, 285, doi: 10.1086/192144

Koushiappas, S. M., Bullock, J. S., & Dekel, A. 2004, MNRAS, 354, 292, doi: 10.1111/j.1365-2966.2004.08190.x

Kozłowski, S. 2016, ApJ, 826, 118, doi: 10.3847/0004-637X/826/2/118

—. 2017, ApJS, 228, 9, doi: 10.3847/1538-4365/228/1/9

Krolik, J. H., Horne, K., Kallman, T. R., et al. 1991, ApJ, 371, 541, doi: 10.1086/169918

Lacy, M., Petric, A. O., Sajina, A., et al. 2007, AJ, 133, 186, doi: 10.1086/509617

Lacy, M., Storrie-Lombardi, L. J., Sajina, A., et al. 2004, ApJS, 154, 166, doi: 10.1086/422816

Laigle, C., McCracken, H. J., Ilbert, O., et al. 2016, ApJS, 224, 24, doi: 10.3847/0067-0049/224/2/24

Le Fèvre, O., Cassata, P., Cucciati, O., et al. 2013, A&A, 559, A14, doi: 10.1051/0004-6361/201322179

Lee, M. H. 1993, ApJ, 418, 147, doi: 10.1086/173378

Lehmer, B. D., Basu-Zych, A. R., Mineo, S., et al. 2016, ApJ, 825, 7, doi: 10.3847/0004-637X/825/1/7

Lilly, S. J., Le Brun, V., Maier, C., et al. 2009, ApJS, 184, 218, doi: 10.1088/0067-0049/184/2/218

Liu, T., Merloni, A., Wang, J.-X., et al. 2018, MNRAS, 479, 5022, doi: 10.1093/

mnras/sty1751

Loeb, A., & Rasio, F. A. 1994, ApJ, 432, 52, doi: 10.1086/174548

Luo, B., Brandt, W. N., Hall, P. B., et al. 2015, ApJ, 805, 122, doi: 10.1088/0004-637X/805/2/122

Lusso, E., Comastri, A., Simmons, B. D., et al. 2012, MNRAS, 425, 623, doi: 10.1111/j.1365-2966.2012.21513.x

Lutz, D., Poglitsch, A., Altieri, B., et al. 2011, A&A, 532, A90, doi: 10.1051/0004-6361/201117107

Maccacaro, T., Gioia, I. M., Wolter, A., Zamorani, G., & Stocke, J. T. 1988, ApJ, 326, 680, doi: 10.1086/166127

MacLeod, C. L., Ivezić, Ž., Kochanek, C. S., et al. 2010, ApJ, 721, 1014, doi: 10.1088/0004-637X/721/2/1014

MacLeod, C. L., Ivezić, Ž., Sesar, B., et al. 2012, ApJ, 753, 106, doi: 10.1088/0004-637X/753/2/106

Madau, P., & Rees, M. J. 2001, ApJ, 551, L27, doi: 10.1086/319848

Mandelbaum, R., Hirata, C. M., Seljak, U., et al. 2005, MNRAS, 361, 1287, doi: 10.1111/j.1365-2966.2005.09282.x

Marchesi, S., Civano, F., Elvis, M., et al. 2016, ApJ, 817, 34, doi: 10.3847/0004-637X/817/1/34

Matt, G., Perola, G. C., & Piro, L. 1991, A&A, 247, 25

Matthews, T. A., & Sandage, A. R. 1963, ApJ, 138, 30, doi: 10.1086/147615

McCracken, H. J., Capak, P., Salvato, M., et al. 2010, ApJ, 708, 202, doi: 10.1088/0004-637X/708/1/202

McCracken, H. J., Milvang-Jensen, B., Dunlop, J., et al. 2012, A&A, 544, A156, doi: 10.1051/0004-6361/201219507

Merloni, A., Bongiorno, A., Brusa, M., et al. 2014, MNRAS, 437, 3550, doi: 10.1093/mnras/stt2149

Mineo, S., Gilfanov, M., & Sunyaev, R. 2012, Monthly Notices of the Royal Astronomical Society, 426, 1870, doi: 10.1111/j.1365-2966.2012.21831.x

Miyaji, T., Griffiths, R. E., & C-COSMOS Team. 2008, in AAS/High Energy Astrophysics Division, Vol. 10, AAS/High Energy Astrophysics Division #10, 4.01

Miyazaki, S., Komiyama, Y., Kawanomoto, S., et al. 2018, PASJ, 70, S1, doi: 10.1093/pasj/psx063

Momcheva, I. G., Brammer, G. B., van Dokkum, P. G., et al. 2016, ApJS, 225,

27, doi: 10.3847/0067-0049/225/2/27

Morokuma, T., Tominaga, N., Tanaka, M., et al. 2016, PASJ, 68, 40, doi: 10.1093/pasj/psw033

Noda, H., Minezaki, T., Watanabe, M., et al. 2016, ApJ, 828, 78, doi: 10.3847/0004-637X/828/2/78

Oke, J. B., & Gunn, J. E. 1983, ApJ, 266, 713, doi: 10.1086/160817

Oliver, S. J., Bock, J., Altieri, B., et al. 2012, MNRAS, 424, 1614, doi: 10.1111/j.1365-2966.2012.20912.x

Onken, C. A., Ferrarese, L., Merritt, D., et al. 2004, ApJ, 615, 645, doi: 10.1086/424655

Park, D., Kelly, B. C., Woo, J.-H., & Treu, T. 2012, ApJS, 203, 6, doi: 10.1088/0067-0049/203/1/6

Park, T., Kashyap, V. L., Siemiginowska, A., et al. 2006, ApJ, 652, 610, doi: 10.1086/507406

Perola, G. C., Puccetti, S., Fiore, F., et al. 2004, A&A, 421, 491, doi: 10.1051/0004-6361:20047118

Peterson, B. M., Balonek, T. J., Barker, E. S., et al. 1991, ApJ, 368, 119, doi: 10.1086/169675

Peterson, B. M., Alloin, D., Axon, D., et al. 1992, ApJ, 392, 470, doi: 10.1086/171447

Peterson, B. M., Berlind, P., Bertram, R., et al. 1994, ApJ, 425, 622, doi: 10.1086/174009

Peterson, B. M., Barth, A. J., Berlind, P., et al. 1999, ApJ, 510, 659, doi: 10.1086/306604

Peterson, B. M., Berlind, P., Bertram, R., et al. 2002, ApJ, 581, 197, doi: 10.1086/344197

Polletta, M., Tajer, M., Maraschi, L., et al. 2007, ApJ, 663, 81, doi: 10.1086/518113

Ponti, G., Cappi, M., Costantini, E., et al. 2013, A&A, 549, A72, doi: 10.1051/0004-6361/201219450

Pooley, D., Blackburne, J. A., Rappaport, S., & Schechter, P. L. 2007, ApJ, 661, 19, doi: 10.1086/512115

Quinlan, G. D., & Shapiro, S. L. 1990, ApJ, 356, 483, doi: 10.1086/168856

Reines, A. E., Greene, J. E., & Geha, M. 2013, The Astrophysical Journal, 775, 116, doi: 10.1088/0004-637x/775/2/116

Ricci, C., Trakhtenbrot, B., Koss, M. J., et al. 2017a, ApJS, 233, 17, doi: 10.3847/1538-4365/aa96ad

—. 2017b, Nature, 549, 488, doi: 10.1038/nature23906

Salvato, M., Ilbert, O., Hasinger, G., et al. 2011, ApJ, 742, 61, doi: 10.1088/0004-637X/742/2/61

Sanders, D. B., Salvato, M., Aussel, H., et al. 2007, ApJS, 172, 86, doi: 10.1086/517885

Schinnerer, E., Smolčić, V., Carilli, C. L., et al. 2007, ApJS, 172, 46, doi: 10.1086/516587

Schinnerer, E., Sargent, M. T., Bondi, M., et al. 2010, ApJS, 188, 384, doi: 10.1088/0067-0049/188/2/384

Schmidt, M. 1963, Nature, 197, 1040, doi: 10.1038/1971040a0

Shakura, N. I., & Sunyaev, R. A. 1973, A&A, 24, 337

Shen, Y., Richards, G. T., Strauss, M. A., et al. 2011, ApJS, 194, 45, doi: 10.1088/0067-0049/194/2/45

Shimizu, T. T., Davies, R. I., Koss, M., et al. 2018, ApJ, 856, 154, doi: 10.3847/1538-4357/aab09e

Silverman, J. D., Kashino, D., Sanders, D., et al. 2015, ApJS, 220, 12, doi: 10.1088/0067-0049/220/1/12

Simm, T., Saglia, R., Salvato, M., et al. 2015, A&A, 584, A106, doi: 10.1051/0004-6361/201526859

Smith, H. J., & Hoffleit, D. 1963, Nature, 198, 650, doi: 10.1038/198650a0

Smolčić, V., Novak, M., Bondi, M., et al. 2017, A&A, 602, A1, doi: 10.1051/0004-6361/201628704

Steinhardt, C. L., Speagle, J. S., Capak, P., et al. 2014, ApJ, 791, L25, doi: 10.1088/2041-8205/791/2/L25

Stern, D., Eisenhardt, P., Gorjian, V., et al. 2005, ApJ, 631, 163, doi: 10.1086/432523

Swartz, D. A., Ghosh, K. K., Tennant, A. F., & Wu, K. 2004, ApJS, 154, 519, doi: 10.1086/422842

Tajer, M., Polletta, M., Chiappetti, L., et al. 2007, A&A, 467, 73, doi: 10.1051/0004-6361:20066667

Tananbaum, H., Avni, Y., Branduardi, G., et al. 1979, ApJ, 234, L9, doi: 10.1086/183100

Taniguchi, Y., Scoville, N., Murayama, T., et al. 2007, ApJS, 172, 9, doi: 10.

1086/516596

Taniguchi, Y., Kajisawa, M., Kobayashi, M. A. R., et al. 2015, Publications of the Astronomical Society of Japan, 67, doi: 10.1093/pasj/psv106

Tozzi, P., Gilli, R., Mainieri, V., et al. 2006, A&A, 451, 457, doi: 10.1051/0004-6361:20042592

Ulrich, M.-H., Maraschi, L., & Urry, C. M. 1997, ARA&A, 35, 445, doi: 10.1146/annurev.astro.35.1.445

Vanden Berk, D. E., Richards, G. T., Bauer, A., et al. 2001, AJ, 122, 549, doi: 10.1086/321167

Vanden Berk, D. E., Wilhite, B. C., Kron, R. G., et al. 2004, ApJ, 601, 692, doi: 10.1086/380563

Vestergaard, M., & Osmer, P. S. 2009, ApJ, 699, 800, doi: 10.1088/0004-637X/699/1/800

Vestergaard, M., & Peterson, B. M. 2006, ApJ, 641, 689, doi: 10.1086/500572

Walton, D. J., Roberts, T. P., Mateos, S., & Heard, V. 2011, MNRAS, 416, 1844, doi: 10.1111/j.1365-2966.2011.19154.x

Woo, J.-H., Treu, T., Barth, A. J., et al. 2010, ApJ, 716, 269, doi: 10.1088/0004-637X/716/1/269

Yaqoob, T. 2012, MNRAS, 423, 3360, doi: 10.1111/j.1365-2966.2012.21129.x

Yasuda, N., Tanaka, M., Tominaga, N., et al. 2019, PASJ, 71, 74, doi: 10.1093/pasj/psz050

Zamojski, M. A., Schiminovich, D., Rich, R. M., et al. 2007, ApJS, 172, 468, doi: 10.1086/516593

Zheng, W., Kriss, G. A., Telfer, R. C., Grimes, J. P., & Davidsen, A. F. 1997, ApJ, 475, 469, doi: 10.1086/303560